8-2024

Comparative Morphology and Development of the Trigeminally Innervated Infrared-Imaging System in Boas and Pythons

Helen Bond Plylar
Utah State University

Recommended Citation

COMPARATIVE MORPHOLOGY AND DEVELOPMENT OF THE TRIGEMINALLY

INNERVATED INFRARED-IMAGING SYSTEM

IN BOAS AND PYTHONS

by

Helen Bond Plylar

A dissertation submitted in partial fulfillment
of the requirements for the degree

of

DOCTOR OF PHILOSOPHY

in

Biology and Ecology

Approved:

_____   _____
Alan H. Savitzky, Ph.D.   Sara Freeman, Ph.D.
Major Professor   Committee Member

_____   _____
Susannah French, Ph.D.   Molly Womack, Ph.D.
Committee Member   Committee Member

_____   _____
Kerry Jordan, Ph.D.   D. Richard Cutler, Ph.D.
Committee Member   Vice Provost for Graduate Studies

UTAH STATE UNIVERSITY
Logan, Utah

2024

ABSTRACT

Comparative Morphology and Development of the Trigeminally Innervated Infrared-

Imaging System in Boas and Pythons

by

Helen Bond Plylar, Doctor of Philosophy

Utah State University, 2024

Major Professor: Dr. Alan H. Savitzky
Department of Biology

Three snake lineages (Boidae, Pythonidae, and Crotalinae) independently evolved the capacity for infrared-imaging and possess pit organs that are used to detect radiant heat. The pit organs are the primary sense organs of the IR-imaging system, and information from the pits is transmitted to the brain via trigeminal nerve rami and ultimately processed in the tectum, the same region that receives visual information. Thus, these snakes effectively "see" heat. While crotaline snakes possess a single pair of pits, boid and pythonid pits occur in paired arrays located within the supra- and infralabial scales. Few studies have examined this system in boas or python. The goal of this dissertation was to compare the morphology of structures critical to the IR-imaging system of boas and pythons (with an emphasis on pit innervation and microvasculature), as well as its development in pythons.

In Chapter 2, I employed traditional histology and micro-computed tomography (microCT) of python embryos to assess variation in the timing of development of the pit organs, trigeminal nerve, and optic tectum. Results of that study demonstrated a

decoupling of pit development between the upper and lower jaws and differences in timing of the innervation of these structures.

In Chapter 3 I used diffusible iodine contrast-enhanced microCT to compare innervation of the pits and labial scales among four species of pythons and two of boas. I found substantial inter- and intrafamilial variation in the trigeminal nerve rami and the pits they serve. Further, some pits were innervated by multiple sub-branches of a given trigeminal ramus, suggesting a more complex spatiotopic arrangement of thermal information in the snake brain than previously reported.

A dense microvascular network underlying the pits contributes to maintenance of an optimal thermal state, presumably reducing formation of thermal after-images. In Chapter 4, I used vascular casting and microCT to examine cephalic vascular patterns and pit microvasculature in three pythons and two boas. Although interspecific differences in microvascular density and morphology exist, vessels underlying the pit organs consistently form a web-like capillary network that projects perpendicularly to contact the IR-sensitive regions of the pit epithelium.

(173 pages)

PUBLIC ABSTRACT

Comparative Morphology and Development of the Trigeminally Innervated Infrared-

Imaging System in Boas and Pythons

Helen Bond Plylar

Boas and pythons use specialized sense organs called pit organs to detect radiant heat. Pit organs in these lineages occur in paired arrays along the upper and lower jaws and are served by the trigeminal nerve (the fifth cranial nerve and one of the largest). Information from the pit organs travels via branches of the trigeminal to the brain and ultimately is processed in the optic tectum, along with information from the visual system. That means these snakes effectively "see" heat. While studies of the pitviper infrared-imaging system are numerous, very few studies of this system in pythons or boas exist, and those only include a few species in each family. The goal of this dissertation was to compare the anatomy of structures critical to the IR-imaging system in boas and pythons (with an emphasis on the nerves and blood vessels) and examine its development in pythons. In Chapter 2, I used histology and micro-computed tomography (microCT) of python embryos to examine variation in the timing of development of structures associated with IR-imaging, including the pit organs, trigeminal nerve, and optic tectum. I found that the pits of the upper and lower jaw do not follow the same developmental timing. In Chapter 3 I used microCT scans of different species (four pythons and two boas) to examine the shape and size of their pit organs and their relationship to the nerves that supply them. I found substantial differences in sub-branching of the trigeminal and

the pits they serve between all species examined. Some of the pit organs were served by multiple sub-branches of the trigeminal, suggesting a more complex mapping of thermal information in the brain than previously reported. In Chapter 4, I used microCT to examine the fine structure of blood vessels serving the pit organs. The microvasculature underlying the pits is consistently complex, but its density and extent varies among the species. Blood vessels underlying the pits presumably help to maintain a constant temperature of the IR-sensitive tissues, thereby improving their ability to detect heat.

For F.H. Mattson

ACKNOWLEDGMENTS

There are many folks here at USU who have been essential to my success in this degree. Chief amongst them are my committee members, Susannah French, Sara Freeman, Molly Womack, and Kerry Jordan. I have been incredibly lucky to have such a stellar group of Women in STEM serving on my committee, providing mentorship and encouragement at every turn. As I continued along a path often plagued by pitfalls and alternatives, my committee remained supportive and enthusiastic, and lent me the independence to choose my own way forward. I would be remiss if I did not also acknowledge the kindness and generosity of the Biology Department staff, particularly Joe Shope, Mike Long, Kim Garrity, and Anthony Sterenchak. Each of them has gone out of their way time and time again to help me and my peers, and I am so extremely appreciative of all that they do.

My labmates, Megen Kepas and Lauren Houstoun, have remained dependable sources of support and camaraderie, for which I am very grateful. They have always been there for me, and in turn I will always be there for them. I am also fortunate to have made many other true friends in my time at USU, some of whom I am doubly fortunate to call my colleagues. To Emily Virgin, Ben Pepper, Erin Lewis, Layne Sermersheim, Sarah McKay Strobel, Jack Phillips, Elsa Jos, Matteo Petit Bon, and Daniel Emmanuel: thanks for your friendship over these many years. Whitney Walkowski, Kenzie Bozeman, Anat Belasen, Brandi Milligan, and Carley Jay were not here with me at USU, but instead cheered me on from afar, and I am so thankful to have them in my corner.

I would also like to thank my family, specifically my parents, grandparents, and

brothers. My parents, in particular, deserve my unending gratitude. They raised a strong-willed child to become a headstrong woman, and have never sought to force me to be anyone other than who I am. My younger brother, Andrew Plylar, and I could not be more different people, yet he never misses an opportunity to tell me how proud he is of me—and there have been many, many times over the past six years when I really needed to hear it. I am also so, so incredibly thankful for my partner and best friend, Cody Godwin, for his enduring love, unwavering commitment, and constant enthusiasm.

Last, but certainly not least, I am eternally grateful to Dr. Alan H. Savitzky. Al has been my mentor for the past six years and will forever remain one of my dearest colleagues and friends. Thank you for seeing potential in me that others before you overlooked, and for offering me the opportunity to join your lab. The circumstances that ultimately led us to this point were nothing short of serendipitous, and I thank my lucky stars every day for whatever forces conspired to ensure our paths would someday cross.

Helen Bond Plylar

CONTENTS

LIST OF TABLES

LIST OF FIGURES

CHAPTER 1
INTRODUCTION

Sensory systems allow animals to detect environmental or internal stimuli and inform their physiological and behavioral responses. Therefore, variation in the morphology of a given sensory system can be an important predictor of ecological niche and may influence predatory, defensive, and reproductive strategies, as well as the circumstances under which those behaviors occur. The capacity for infrared-imaging evolved independently in three clades of snakes: Boidae, Pythonidae, and Crotalinae. Snakes in these clades possess specialized cephalic sensory structures called pit organs, which are located within (Pythonidae, Crotalinae) or between (Boidae) the facial or labial scales and are used to detect the heat generated by the movement of infrared (IR) photons. Research has demonstrated that IR-imaging in snakes complements visual imaging, as information from both sensory modalities is ultimately processed and superimposed in the optic tectum (Terashima and Goris, 1975; Hartline et al., 1978; Newman and Hartline, 1981). Thus, while a few other animals (e.g., *Desmodus rotundus*, the common vampire bat—Kurten and Schmidt, 1982; *Melanophila accuminata*, forest fire-seeking beetles—Schmitz and Bleckmann, 1998) are capable of advanced heat detection, IR-imaging snakes are the only animals known to truly *see* heat.

Utility of the Infrared-imaging System

For those snakes capable of IR-imaging, this sensory system is used in prey detection and acquisition (Bullock and Diecke, 1956; Goris and Nomoto, 1967; Bullock and Barrett, 1968; Barrett et al., 1970; de Cock Buning et al., 1981;

Kardong and Mackessy, 1991; Kardong, 1993; Haverly and Kardong, 1996; Ebert

et al., 2006), predator avoidance (Greene, 1992), defensive targeting (Glaudas and

Gibbons, 2005; Van Dyke and Grace, 2010), thermoregulation via basking site

selection (Krochmal and Bakken, 2000; Krochmal and Bakken, 2003; Krochmal et

al., 2004), and hibernaculum site selection (Sexton et al., 1992). Both the

morphology and innervation of snake pit organs influence the sensitivity and

function of the IR-imaging system (de Cock Buning, 1985; Molenaar, 1992;

Bakken and Krochmal, 2007; Bakken et al., 2012). There is wide variation in pit

organ morphology both within and between families, which presumably places

constraints on these behaviors and may influence thermoreceptive efficiency in a

given environment. This appears to be reflected in the similarity of pit organs of

boas, pythons, and pitvipers that occupy similar habitats. For example, arboreal

species appear to possess larger pit organs or pit organ arrays relative to terrestrial

species, which hypothetically increases their field of view and may make arboreal

species more successful predators of birds and other tree-dwelling prey.

Signal Generation and Neural Processing

The pit organs of IR-imaging snakes are lined with transient receptor potential

(TRP) channels, specifically TRPA1, that respond to radiant heat (Gracheva et al., 2010).

Heat generated from the movement of infrared photons contacts the TRP-embedded

tissues of the pit organ, activating the TRP channels, and generating action potentials.

The morphology of the pit organs is taxon-specific, but all receive afferent innervation by

branches of the trigeminal nerve (cranial nerve [CN] V) (Lynn, 1931; Bullock and Fox,

1957; Kishida et al., 1980), which is the fifth and most extensive cranial nerve in the head of vertebrates. Action potentials generated at the level of the pit organ are conducted via branches of CN V to the lateral tract of the trigeminal descendens (LTTD), a region of the medulla unique to IR-imaging snakes (Molenaar, 1974; Schroeder and Loop, 1976; Terashima and Goris, 1977; Meszler et al., 1981). In boas and pythons, this information is subsequently relayed downstream directly to the contralateral tectum, the same region of the ophidian brain that receives information from the lateral eyes of the visual system (Barrett, 1969; Goris and Terashima, 1973; Terashima and Goris, 1975; Haseltine, 1978; Newman et al., 1980). In pitvipers, there is an additional ipsilateral relay nucleus between the LTTD and the tectum known as the reticularis caloris (RC) (Gruberg et al., 1979; Kishida et al, 1980; Newman et al., 1980; Stanford et al., 1981; Meszler, 1983), and this extra step in the transmission of IR-information from the LTTD to the tectum is thought to further improve the resolution of the crotaline IR-imaging system.

Histological tracing studies have demonstrated that single tectal neurons receive projections from both the visual and infrared pathways (Kobayashi et al., 1992), and electrophysiological studies have identified overlap in visual and IR receptive fields in the tectum (Bullock and Diecke, 1956). Thus, it is hypothesized that merging of information from these two sensory systems allows snakes to form detailed, spatial maps of their combined thermal and visual environments (Hartline et al., 1978). In the visual system, the ganglion cells of the retina project in a highly ordered fashion onto tectal neurons, generating a spatiotopic mapping of visual information in the optic tectum of the vertebrate brain. However, due to the wider receptive field of the pit organs, lack of a crystalline lens, and relative paucity of infrared receptors (compared to visual receptors,

which number in the millions), the image produced by the pit organs alone likely lacks

the degree of spatial resolution produced by the visual system (Terashima and Goris,

1975; Berson and Hartline, 1988; Sichert et al., 2006). Indirect projection of neurons

from the pit organ, via the LTTD or LTTD-RC relay, may also degrade the spatial

resolution of the infrared image.

Theoretical studies of crotaline pit organ function have used principles of

geometric optics and computational modeling to generate simulations of the images

produced by the IR-imaging system (Krochmal and Bakken, 2003; Krochmal et al., 2004;

Bakken and Krochmal, 2007; Bakken et al., 2012). Electrophysiological studies of the

overlap of visual and thermal information processing in the brain have also emphasized

that spatial resolution of IR-imaging in snakes is apparently much coarser than that of the

visual system (Bakken and Krochmal, 2007; Berson and Hartline, 1988). However, such

results appear to contradict findings of behavioral studies, which have consistently

demonstrated that IR-imaging snakes are capable of highly accurate targeting and striking

when presented with a thermal stimulus, independent of whether or not the lateral eyes

are occluded (e.g., *Python sebae*—Ros, 1935; *P. regius*— Ebert, et al., 2007; *Agkistrodon

contortrix*—Van Dyke and Grace, 2010; *Gloydius brevicaudus*—Chen et al., 2012). One

possible explanation for this apparent disparity is that the merging of these two sensory

modalities in the brain corrects for the theoretical limitations on resolution imposed by pit

organ geometry, thus enabling the highly accurate strikes observed in behavioral trials.

Pit Organ Morphology

There is substantial inter- and intrafamilial variation in pit organ morphology in

terms of the number, shape, size, and position of these sensory structures. Since the pit

organs are proposed to function as a pinhole optical system, however rudimentary, their geometry is critically important to their function (de Cock Buning, 1985; Molenaar, 1992; Bakken and Krochmal, 2007; Bakken et al., 2012). Thus, pit organ diversity likely underscores species-specific differences in thermally guided behaviors and ecological niche occupancy.

Pitvipers (family Viperidae, subfamily Crotalinae) possess a pair of deep, structurally complex pit organs, one on either side of the face in the loreal region, which occupies a bony fossa within the prefrontal and maxillary bones. The aperture of the crotaline pit is narrow, opening into a wider interior space that is subdivided into an inner and outer chamber by the IR-sensitive pit membrane (Lynn, 1931; Bullock and Diecke, 1956; Bullock and Fox, 1957). A pore located between the medial side of the eye and the lateral side of the pit connects to the inner chamber, supplying it with air. It is hypothesized that the structure of the crotaline pits and the suspension of the pit membrane between the air-filled inner and outer chambers lends itself to increased sensitivity relative to the pits of pythons and boas. However, while the pitvipers are limited to only a pair of pit organs, boas and pythons possess arrays of pit organs located either within (pythons) or between (boas) the supra- and/or infralabial scales. Unlike the pit organs of Crotalinae, those of the pythons and boas do not implicate the underlying bones and are limited to the soft tissues of the labial scale rows, including, in some pythons, the rostral scale (Ros, 1935).

There is wide inter- and intrafamilial variation in pit organ morphology among pythons and boas, though some general trends exist for each family, respectively. Pythons generally possess rostral supralabial (which include both the pits on the rostral scale and

those within the anterior supralabial scales) and caudal infralabial pit arrays, each with 3-5 pits per side (Ros, 1935; Noble and Schmidt, 1937; Warren and Proske, 1968). The shapes of the pits in the supralabial array vary: *Python molurus*, *P. sebae*, and *P. reticulatus* have 3-4 inverted tear-drop shaped pits that decrease in size caudally; the supralabial pits of *Morelia spilota* exhibit a similar rostral-to-caudal decrease in size, but are more triangular; in *P. regius*, the 5 pits are much larger (relatively speaking), and round, and the rostral-to-caudal size decrease is much less obvious. Other pythons, such as *Antaresia childreni*, often lack any evidence of rostral supralabial pits, but possess well-developed caudal infralabial pit arrays. When present in pythons, the infralabial pit array is much less variable in terms of external shape of the pits, the margins of which generally appear squared. The only genus of python that lacks pit organs entirely is *Aspidites*, the basal-most lineage of the Australian python clade. In all pythonid pit organs, the infrared-sensitive tissues are located at the base of the pit organ, or the pit fundus. The pit aperture is slightly narrower than the fundus, though still much wider relative to the sensory membrane than that of the pitvipers.

The pit organs of boas are distinctive in that, rather than a deep invagination within a scale, the pits are formed from a widening or depression between adjacent labial scales, lending a folded appearance to the arrays. Unlike the pitvipers and pythons, the infrared-sensitive tissues of boid pits do not lie at the base, or fundus, between these folds, but rather on the rostral and caudal sides, respectively, of the proximal and distal scales implicated (Ebert, 2007). Thus, a pit aperture is entirely absent. While not technically correct, I will be referring to these structures in boas as "pit organs" or "pit arrays", when present, throughout this work, as they are functionally analogous to the

true pits of the other two infrared-sensing taxa. Arboreal boas, such as *Corallus hortulanus*, *C. caninus*, and *Sanzinia madagascariensis* have very obvious arrays of pits, as evidenced by the extent and depth of the folds present between the supra- and infralabial scales. Other boas, such as the terrestrial *Boa constrictor,* do not exhibit an obvious capacity for IR-imaging at all, as they have been previously reported to lack any external, macroscopic evidence of pit organs. However, previous electrophysiological and histological studies have demonstrated that they still possess infrared-sensitive regions in the same relative locations as the more obviously pitted boid taxa (von During, 1974; von During and Miller, 1979; Amemiya et al., 1996).

The structure and directional positioning of the pits of pitvipers and pythons result in a receptive area that is never fully stimulated by incoming IR, but movement of an IR source relative to the snake (or vice versa) causes incoming wavelengths to contact different regions of the pits as the IR source/snake changes position. While boid pit organs are morphologically quite dissimilar to those of pythons, movement relative to a given IR stimulus still produces a change in its field of view (Ebert, 2007). The striking morphological variation between the pit organs of boids, pythonids, and crotaline snakes reflects independent evolution of the IR sensory system, or at least its peripheral features, in each lineage.

Development of the Infrared-Imaging System

While the structure of pit organs has been examined in adults of a few pythonid and boid species, there are no published reports on their embryonic development in these families. However, the development of the pit organs has been described for several species of pitvipers (*Agkistrodon contortrix*, *A. piscivorus*, *Crotalus horridus*, *C. atrox* —

Savitzky, 1992; *Bothrops jararaca*, *C. durissus*, *Gloydius halys*, *Trimeresurus albolabris* — Hofstadler-Deiques, 2002). During development in pitvipers, the maxillary and ophthalmic branches of the trigeminal nerve (which ultimately both serve the crotaline pit organ) extend anteriorly as the pit organ invaginates. Pit invagination begins at a stage equivalent to Zehr Stage 27 and continues in concert with the formation of the maxillary and prefrontal bones, which eventually form a bony fossa around the pit organ (Savitzky, 1992). Ultimately, the pit organs and maxillary fangs of Crotalinae are both innervated by sub-branches of the maxillary nerve, and the shared pattern of hypertrophy between the pits and adjacent dentition suggests that there may be a common underlying developmental mechanism between these two structures (Savitzky, 1992). The pit organs of at least one species of python, *P. regius*, are first evident externally at a timepoint equivalent to Zehr Stage 30-33 (Savitzky, 1984), though their initial invagination may begin earlier. The rostral pits form first, followed by each successive pit in the supralabial array (Savitzky, 1984). The development of the pit organs in boas remains undescribed. Like the paired loreal pits of crotaline snakes, the supralabial pit organs of pythons and boas are also associated with two branches of the trigeminal nerve: the rostral pits are innervated by the ophthalmic (Lynn, 1931) or maxillary branch (Warren and Proske, 1968), the supralabials by the maxillary branch (Warren and Proske, 1968), and the infralabials by the mandibular branch (Warren and Proske, 1968). Whether this pattern of innervation reflects a process similar to that of pitvipers is unclear. However, most pythons exhibit both rostral pit organs and premaxillary dentition, whereas boas exhibit neither, which may further support the hypothesis of a shared developmental mechanism for these structures.

Dissertation Overview

The chapters that follow constitute an investigation of the development and morphology of the trigeminally innervated infrared-imaging system of pythons and boas. Chapter II combines traditional histology and micro-computed tomographic (microCT) scanning to provide a description of the embryonic development of the pit organs, their blood supply, and their innervation by the trigeminal nerve in three pythons (*Antaresia childreni*, *Python molurus*, and *P. regius*). Chapter III provides a description of the morphological variation in the trigeminal nerve in adults of four species of python (*Antaresia childreni*, *Morelia spilota*, *Python molurus*, and *P. regius*) and two species of boa (*Boa constrictor* and *Corallus hortulanus*) while Chapter IV describes the blood supply to the pit organs in these taxa.

References

Amemiya, F., R. C. Goris, Y. Atobe, N. Ishii, and T. Kusunoki. 1996. The ultrastructure of infrared receptors in a boid snake, Python regius: evidence for periodic regeneration of the terminals. Animal Eye Research (15): 13-25.

Bakken, G. S., and A. R. Krochmal. 2007. The imaging properties and sensitivity of the facial pits of pitvipers as determined by optical and heat-transfer analysis. Journal of Experimental Biology, 210(16): 2801-2810.

Bakken, G. S., S. E. Colayori, and T. Duong. 2012. Analytical methods for the geometric optics of thermal vision illustrated with four species of pitvipers. Journal of Experimental Biology, 215(15): 2621-2629.

Barrett, R., P. F. A. Maderson, and R. M. Meszler. 1970. The pit organs of snakes. In C. Gans and T.S. Parsons (Eds.), Biology of the Reptilia (Vol. 2, pp. 277-300). Academic Press, London and New York.

Berson, D.M., and P. H. Hartline. 1988. A tecto-rotundo-telencephalic pathway in the rattlesnake: evidence for a forebrain representation of the infrared sense. Journal of Neuroscience. 8: 1074-1088.

Bullock, T. H., and R. Barrett. 1968. Radiant heat reception in snakes. Communications in Behavioral Biology, 1: 19-29.

Bullock, T. H., and F. P. J. Diecke. 1956. Properties of an infra-red receptor. The Journal of Physiology, 134(1): 47-87.

Bullock, T.H., and W. Fox. 1957. The anatomy of the infra-red sense organ in the facial pit of pitvipers. Quarterly Journal of Microscopical Science 98(2): 19-234.

Chen, Q., H. Deng, S. E. Brauth, L. Ding, and Y. Tang. 2012. Reduced performance of prey targeting in pit vipers with contralaterally occluded infrared and visual senses. PLoS One, 7(5): e34989.

de Cock Buning, T. 1985. Qualitative and quantitative explanation of the forms of heat sensitive organs in snakes. In G.G. Zweers and P. Dullemeijer (Eds.), Architecture in Living Structure (pp. 87-99). Springer, Dordrecht.

de Cock Buning, T., R. C. Goris, and S. I. Terashima. 1981. The role of thermosensitivity in the feeding behavior of the pitviper, Agkistrodon blomhoffi brevicaudus. Japanese Journal of Herpetology, 9: 7-27.

Ebert, J., S. Müller, and G. Westhoff. 2007. Behavioural examination of the infrared sensitivity of ball pythons. Journal of Zoology, 272(3): 340-347.

Ebert, J. 2008. Infrared Sense in Snakes—Behavioural and Anatomical Examinations (Crotalus atrox, Python regius, Corallus hortulanus). Unpubl. Ph.D. diss., University of Bonn, Germany.

Glaudas, X., and J. W. Gibbons. 2005. Do thermal cues influence the defensive strike of cottonmouths (Agkistrodon piscivorus). Amphibia Reptilia, 26(2): 264-267.

Goris, R. C. (2011). Infrared organs of snakes: an integral part of vision. J of Herpetology, 45(1): 2-15.

Goris, R. C., and M. Nomoto. 1967. Infrared reception in oriental crotaline snakes. Comparative Biochemistry and Physiology, 23(3): 879-892.

Goris, R. C., and S. Terishima. 1973. Central response to infra-red stimulation of the pit receptors in a crotaline snake, Trimeresurus flavoviridis. Journal of Experimental Biology 58: 59-76.

Goris, R. C., T. Kadota, and R. Kishida. 1989. Innervation of snake pit organ membranes mapped by receptor terminal succinate dehydrogenase activity. Current Herpetology in East Asia: 8-16.

Gracheva, E. O., N. T. Ingolia, Y.M. Kelly, J.F. Cordero-Morales, G. Hollopeter, A. T. Chesler, and D. Julius. 2010. Molecular basis of infrared detection by snakes. Nature, 464(7291): 1006-1011.

Greene, H. W. (1992). The ecological and behavioral context for pitviper evolution. In J.A. Campbell and E.D. Brodie (Eds.), Biology of the Pitvipers (pp. 107-117). Selva Publishing, Tyler, TX.

Gruberg, E. R., E. Kicliter, E. A. Newman, L. Kass, and P. H. Hartline. 1979. Connections of the tectum of the rattlesnake Crotalus viridis: an HRP study. Journal of Comparative Neurology, 188(1): 31-41.

Hartline, P. H., L. Kass, and M. S. Loop. 1978. Merging of modalities in the optic tectum: infrared and visual integration in rattlesnakes. Science, 199: 1225-1229.

Haseltine, E. C. 1978. Infrared and Visual Organization of the Tectum of Boid Snakes. Unpubl. Ph.D. diss., Indiana University, Bloomington.

Haverly, J. E., and K. V. Kardong. 1996. Sensory deprivation effects on the predatory behavior of the rattlesnake, Crotalus viridis oreganus. Copeia: 419-428.

Hofstadler-Deiques, C. 2002. The development of the pit organ of Bothrops jararaca and Crotalus durissus terrificus (Serpentes, Viperidae): support for the monophyly of the subfamily Crotalinae. Acta Zoologica, 83(3): 175-182.

Kardong, K. V. 1993. The predatory behavior of the Northern Pacific rattlesnake (Crotalus viridis oreganus): laboratory versus wild mice as prey. Herpetologica: 457-463.

Kardong, K. V., and S. P. Mackessy. 1991. The strike behavior of a congenitally blind rattlesnake. Journal of Herpetology, 25(2): 208-211.

Kishida, R., F. Amemiya, T. Kusunoki, and S. I. Terashima. 1980. A new tectal afferent nucleus of the infrared sensory system in the medulla oblongata of Crotaline snakes. Brain Research, 195(2): 271-279.

Kobayashi, S., R. Kishida, R. C. Goris, M. Yoshimoto, and H. Ito. 1992. Visual and infrared input to the same dendrite in the tectum opticum of the python, Python regius: electron-microscopic evidence. Brain Research 597: 350–352.

Kohl, T., M. S. Bothe, H. Luksch, H. Straka, and G. Westhoff. 2014. Organotopic organization of the primary Infrared Sensitive Nucleus (LTTD) in the western diamondback rattlesnake (Crotalus atrox). Journal of Comparative Neurology, 522(18): 3943-3959.

Krochmal, A. R., and G. S. Bakken. 2000. Evidence for the use of facial pits for behavioral thermoregulation in the western diamondback rattlesnakes (Crotalus atrox). American Zoologist 40(6): 1092-1093.

Krochmal, A. R., and G. S. Bakken. 2003. Thermoregulation is the pits: use of thermal radiation for retreat site selection by rattlesnakes. Journal of Experimental Biology, 206(15): 2539- 2545.

Krochmal, A. R., G. S. Bakken, and T. J. LaDuc. 2004. Heat in evolution's kitchen: evolutionary perspectives on the functions and origin of the facial pit of pitvipers (Viperidae: Crotalinae). Journal of Experimental Biology, 207(24): 4231-4238.

Kürten, L., and U. Schmidt.1982. Thermoperception in the common vampire bat (Desmodus rotundus). Journal of Comparative Physiology, 146(2): 223-228.

Lynn, W.G. 1931. The structure and function of the facial pit of the pitvipers. American Journal of Anatomy 49: 97-139.

Meszler, R. M. 1983. Fine structure and organization of the infrared receptor relays: lateral descending nucleus of V in Boidae and nucleus reticularis caloris in the rattlesnake. Journal of Comparative Neurology, 220(3): 299-309.

Meszler, R.M., C. R. Auker, and D. O. Carpenter. 1981. Fine structure and organization of the infrared receptor relay, the lateral descending nucleus of the trigeminal nerve in pitvipers. Journal of Comparative Neurology, 196: 571-584.

Molenaar, G. J. 1974. An additional trigeminal system in certain snakes possessing infrared receptors. Brain Research, 78: 340-344.

Molenaar, G. J. 1992. Anatomy and physiology of infrared sensitivity of snakes. In C. Gans and T.S. Parsons (Eds.), Biology of the Reptilia (Vol. 17, pp. 367-453). Academic Press, London and New York.

Newman, E. A., E. R. Gruberg, and P. H. Hartline.1980. The infrared trigemino-tectal pathway in the rattlesnake and in the python. Journal of Comparative Neurology, 191(3): 465-477.

Newman, E. A., and P. H. Hartline. 1981. Integration of visual and infrared information in bimodal neurons in the rattlesnake optic tectum. Science, 213(4509): 789-791.

Noble, G. K., and A. Schmidt. 1937. The structure and function of the facial and labial pits of snakes. Proceedings of the American Philosophical Society: 263-288.

Ros, M. (1935). Die Lippengruben der Pythonen als Temperaturorgane. Jenaische Zeitschrift für Naturwissenschaft, 70: 1-32.

Savitzky, A. H. (1984). Development of the thermoreceptive pit organs in the boid snake Python regius. American Zooloogist 4(25): 107A

Savitzky, Alan H. 1992. Embryonic Development of the Maxillary and Prefrontal Bones of Crotaline Snakes. In J. A. Campbell and E. D. Brodie, Jr. (Eds.), The Biology of Pitvipers (pp. 119-142). Selva Publishing, Tyler, TX.

Schmitz, H., and H. Bleckmann. 1998. The photomechanic infrared receptor for the detection of forest fires in the beetle Melanophila acuminata (Coleoptera: Buprestidae). Journal of Comparative Physiology A, 182(5): 647-657.

Schroeder, D. M., and M. S. Loop. 1976. Trigeminal projections in snakes possessing infrared sensitivity. Journal of Comparative Neurology, 1691: 1-14.

Sexton, O. J., P. Jacobson, and J. E. Bramble. 1992. Geographic variation in some activities associated with hibernation in nearctic pitvipers. In J.A. Campbell and E.D. Brodie (Eds.), The Biology of the Pitvipers (pp. 337-345). Selva Publishing, Tyler, TX.

Sichert, A. B., P. Friedel, and J. L. van Hemmen. 2006. Snake's perspective on heat: reconstruction of input using an imperfect detection system. Physical Review Letters, 97(6): 68-105.

Stanford, L. R., D. M. Schroeder, and P. H. Hartline. 1981. The ascending projection of the nucleus of the lateral descending trigeminal tract: A nucleus in the infrared

system of the rattlesnake, Crotalus viridis. Journal of Comparative Neurology, 201(2): 161-173.

Terashima, S. I., and R. C. Goris. 1975. Tectal organization of pitviper infrared reception. Brain Research, 83: 490-494.

Terashima, S. I., and R. C. Goris. 1977. Infrared bulbar units in crotaline snakes. Proceedings of the Japan Academy, Series B, 53(7): 292-296.

Van Dyke, J. U., and M. S. Grace. 2010. The role of thermal contrast in infrared-based defensive targeting by the copperhead, Agkistrodon contortrix. Animal Behaviour, 79(5): 993-999.

Von Düring, M. 1974. The radiant heat receptor and other tissue receptors in the scales of the upper jaw of Boa constrictor. Zeitschrift für Anatomie und Entwicklungsgeschichte, 145: 299-319.

Von During, M., and M.R. Miller. 1979. Sensory nerve endings of the skin and deeper structures. Biology of the Reptilia, Neurology A., 9, 407-441.

Warren, J. W., and U. Proske. 1968. Infrared receptors in the facial pits of the Australian python Morelia spilotes. Science, 159(3813): 439-441.

CHAPTER 2

COMPARATIVE DEVELOPMENT OF THE INFRARED IMAGING SYSTEM IN
THREE SPECIES OF PYTHONS

INTRODUCTION

The Snake Infrared-Imaging System

Snakes are a highly diverse and prolific tetrapod lineage, with >4000 extant

species and major radiations spanning all continents except Antarctica. Perhaps the most

readily identifiable feature of snakes is their lack of limbs. Although some basal lineages

(e.g., Pythonidae and Boidae) have retained remnants of the pelvic girdle and vestigial

hindlimbs, these are essentially nonfunctional for locomotion, and the pectoral girdle is

entirely absent. Despite their evolutionary loss of limbs, their success as predators is

infamous. This success hinges almost entirely upon the evolution of highly specialized

cranial and other cephalic structures, which allow snakes to detect and apprehend a wide

variety of prey items. One such structural system involves the pit organs of boid,

pythonid, and crotaline snakes. These pits are the cephalic sense organs of the infrared-

imaging system, which function in the detection of radiant heat.

The pit organs of all three lineages are innervated by one or more branches of the

trigeminal nerve (CN V), which is the fifth cranial nerve and one of the two most

expansive. The morphology of the pit organs and the pattern of pit innervation varies

between taxa and is described in more detail below. However, in all cases, the pit organs

detect radiant heat via the action of transient receptor potential (TRP) channels (Gracheva

et al., 2010). When exposed to heat, the TRP channels generate nerve impulses that travel

via branches of the trigeminal to the lateral tract of the trigeminal descendens (LTTD), a hindbrain nucleus unique to pit-bearing snakes (Molenaar, 1974; Schroeder and Loop, 1976; Terashima and Goris, 1977; Meszler et al., 1981; Terashima and Liang, 1991). Information from the LTTD is subsequently routed to either a second hindbrain nucleus (the reticularis caloris [RC], which is unique Crotalinae; Gruberg et al., 1979; Kishida et al, 1980; Newman et al., 1980; Stanford et al., 1981; Meszler, 1983) or directly to the optic tectum (Boidae, Pythonidae), where it is processed deep to the neural layer receiving visual information (Terashima and Goris, 1975; Hartline et al., 1978; Newman and Hartline, 1981). Processing of visual and thermal information in the tectum means that not only are these snakes capable of advanced heat detection, but they effectively *see* heat. Thus, the pit organs, trigeminal rami and ganglia, RC and/or LTTD, and the optic tectum are collectively known as the "infrared-imaging system."

Current evidence suggests that the infrared-imaging system has evolved independently in each of the three taxa that possess it, and this independent evolution is reflected in the extreme interfamilial variation in pit organ morphology (Maderson, 1970). Crotaline snakes (Family Viperidae, Subfamily Crotalinae), the "pitvipers", have paired pit organs, with only a single pit bordered by the lacunal scales on either side of the face between the eye and nostril. The pit organs of crotaline snakes are anatomically complex, with a narrow aperture that opens into a wider, mushroom-shaped cavity (Lynn, 1931; Bullock and Diecke, 1956; Bullock and Fox, 1957). This cavity forms within a bony fossa between the maxillary and prefrontal bones (Dullemeijer, 1959), and is separated into an inner and outer chamber by the pit membrane (Bullock and Fox, 1957). The individual pit organs of boas and pythons are less complex morphologically than

those of pitvipers, but they are much more numerous. Rather than a single pit organ on either side of the face, the pits of boas and pythons occur as paired arrays located between (boas) or within (pythons) the supra- and infralabial scales (Ros, 1935). In boas, the heat-sensitive tissues are located between the scales, and in those that have obvious pits (e.g., *Corallus hortulanus*) the rostral and caudal margins of some labial scales are depressed into a v-shaped space between adjacent scales (Ebert, 2007). Most pythons have pits that form within the rostral scale and anterior supralabial scales and/or within the caudal infralabial scales (Ros, 1935). These pits vary in number, shape, size, and depth among pythonid species, though in all cases the heat-sensitive tissues are located in the base of the pit, known as the "pit fundus."

Embryonic Development of the Snake Infrared-Imaging System

Studies of snake development are technically challenging, owing to the difficulty of ensuring success in captive-breeding programs (some species readily breed in captivity, others do not), differences in reproductive strategies (oviparity vs. viviparity), which require different methods of embryo collection, and variation in clutch or litter sizes. As such, developmental studies of snakes in general have been limited in number, and the development of the infrared-imaging system in snakes has received even less attention. Current knowledge of the embryonic development of any aspect of the infrared-imaging system is limited to only a few species of pitvipers (*Agkistrodon contortrix, A. piscivorous, Crotalus atrox, C. horridus* – Savitzky, 1992; *Bothrops jararaca, Crotalus durissus, Gloydius halys, Trimeresurus albolabris*—Hofstadler-Deiques, 2002; *Bothrops atrox*—Silva et al., 2023).

During development in pitvipers, the opthalmic (V_1) and maxillary (V_2) branches of CN V extend rostrally as the pit organ invaginates, and invagination continues in concert with the formation of the maxillary and prefrontal bones (Savitzky, 1992). The ganglia and three primary branches of CN V are present in Zehr Stage 26, prior to the onset of craniogenesis, whereas the pit organ is first evident at Stage 27 in histological sections (Savitzky, 1992). By Stage 29 the maxillary mesenchyme surrounds the deep branch of the maxillary nerve (V_2d). Deep invagination of the pit organs begins at approximately Stages 30-32, co-occurring with a thinning of the mesenchyme lateral to the maxilla, potentially facilitating the positioning of the pit organ within the bony fossa that eventually forms between the maxillary and prefrontal bones. Ultimately, the loreal pit organs and adjacent maxillary fangs of Crotalinae are both innervated by V_2, and that shared pattern of hypertrophy suggests that there may be a common underlying developmental mechanism between these two trigeminally innervated structures (Savitzky et al., 1992).

The pit arrays of pythons are associated with separate branches of the trigeminal nerve: the rostral pits are innervated by V_1 or V_2 (de Cock Buning and Dullemeijer, 1977; Tan and Gopalakrishnakone, 1988) the supralabials by V_2 (de Cock Buning and Dullemeijer, 1977; Tan and Gopalakrishnakone, 1988) and the infralabials by the mandibular branch (V_3) (de Cock Buning and Dullemeijer, 1977; Tan and Gopalakrishnakone, 1988). The supralabial pit organs in *Python regius* are first evident externally at a stage equivalent to Zehr Stage 30-33, and develop in series from rostral to caudal (Savitzky, 1985). As in pitvipers, appearance of the pit organs in pythons occurs later in development than that of the other cephalic sensory organs (e.g., the eyes, tongue,

vomeronasal organ), but prior to the development of scales or pigmentation (Savitzky, 1985). No other published works have addressed any aspects of pit organ development in pythons nor the development of any other component of the python infrared-imaging system.

I used histological sections and microCT scans of embryos to assess post-ovipositional development of the infrared-imaging system in three species of python: *Antaresia childreni, P. molurus, and P. regius*. The morphology of the pit arrays in adults varies substantially among these taxa. Both *P. regius* and *P. molurus* possess large, robust supralabial pit organs, but only small, shallow depressions in the infralabial array. Conversely, *A. childreni* lacks supralabial pits entirely, but possesses well-defined pits in its infralabial array. Here, I describe the development of the supra- and infralabial pit organs, the trigeminal nerve ganglia and rami, and the optic tectum in these species. I hypothesized that the interspecific differences in morphology are associated with differences in the timing of development of these structures, and that the developmental sequence of the supra- and infralabial pits does not follow the same patterning process.

MATERIALS AND METHODS

Acquisition of Prepared Slides

Previously prepared slides of *Python regius* and *P. molurus* embryos were loaned from the collection of the Division of Amphibians and Reptiles at the United States National Museum of Natural History (USNM). The slides had been prepared in the laboratory of Alan H. Savitzky, at Old Dominion University (ODU) between 1988 and 1989, largely with support of NSF BSR-8415752, and had been donated to the USNM in

2011. The embryos used to generate these slides were harvested from eggs laid by wild-caught, gravid dams of *P. regius* that had been captured for the commercial trade and were housed at Old Dominion prior to oviposition or, for *P. regius*, from eggs laid at other institutions and donated to the Savitzky lab. Eggs were incubated at 31.5°C throughout post-ovipositional development. Embryos were removed from their eggs at different developmental time points (Table 2.1.), preserved in either 10% phosphate buffered formalin (PBF) or formalin-alcohol-acetic acid (FAA, for nerve staining), and prepared according to standard histological practices described in Savitzky (1992). Preparation involved decalcification in a 1:1 solution of 8% formic acid to 8% hydrochloric acid (several hours to several days), before embedding in a paraffin-polymer compound (Paraplast Plus) and sectioning at 5-10μm on either the frontal or transverse plane (Table 2.1.).. Sections were stained using either Crowder's Trichome stain (Crowder, 1983) or Bodian's protargol with gallocyanin counterstain (Humason, 1979), the latter stain being used for better visualization of developing nerves (Table 2.1.). When stained with Crowder's Trichome stain, collagen and bone appear blue, nerves appear purple, and blood vessels appear as dark orange-red. Stained slides were coverslipped with Permount mounting medium, and stored in slide boxes for future use.

Imaging of Histological Slides

Prior to imaging, slides were cleaned using xylenes to remove residual mounting medium and were wiped with 70% ethanol to remove fingerprints and dust. A Leica DM4000 B LED compound light microscope with camera attachment (Leica DFC290HD) and Leica Acquisition Suite software (LASv4.1) were used to acquire

images of each section. Whole sections were imaged at 4.825x total magnification (2.5x

objective, 1.93x camera adapter lens). A single image was generated for smaller sections,

whereas multiple images were generated for larger sections and combined into a single

image using the deprecated 2D stitching option in the Stitching module (Preibisch et al.,

2009) in ImageJ (version 1.54b). Higher magnification images were acquired for regions

of interest in a subset of sections at 19.3x total magnification (10x objective, 1.93x

camera adapter lens) or 77.2x total magnification (40x objective, 1.93x camera adapter

lens).

Whole Embryo Acquisition and Preparation

In addition to the histological slides of *P. molurus* and *P. regius*, intact embryos of

Antaresia children were also acquired for microCT scanning. Those embryos were

collected from a breeding colony maintained by the DeNardo Lab at Arizona State

University and were donated by Dr. Dale DeNardo (Table 2.2.). Eggs were incubated at

31.5°C throughout post-ovipositional development. Embryos were removed from their

eggs at different developmental time points (Table 2.2.) and preserved in 10% PBF

(Appendix A). Those collected at day of hatch (days 45-50 POP) were euthanized via

decapitation prior to fixation in 10% PBF.

Although well-calcified skeletal elements do not require any preparation prior to

microCT scanning, a contrast agent must be used for visualization of soft tissues. In order

to visualize developing nerves and pit organs in the embryos, I used established protocols

developed for staining of embryonic soft tissues (Metscher, 2011). A common contrast

agent used for visualizing embryonic tissues under microCT is 1% Phosphotungstic Acid

(PTA; Appendix B). Embryos were removed from 10% PBF, rinsed in deionized water

(ddH_2O), and dehydrated through a graded series of ethanol (15% EtOH → 35% EtOH

→ 70% EtOH; 15 minutes at each step). Following dehydration in 70% EtOH, embryos

were submerged in 1% PTA in EtOH for at least 48 hours prior to microCT scanning.

MicroCT Scanning and Reconstruction of 3D Volumes

Embryos were suspended in 70% EtOH inside individual polypropylene

microcentrifuge tubes to prevent desiccation during scanning. For each scan, a tube

containing a single embryo was secured in floral foam and placed on the stage inside the

chamber of a Nikon XT H 225 ST scanner, and scans were acquired at 2s exposure, 18dB

gain, and 4476 projections with a frame averaging of 1. Due to differences in relative size

and density of embryos of different species and developmental ages, scan parameters for

voltage, current, power, and pixel spacing varied, and were optimized for each individual

(Table 2.3), to ensure that the highest resolution was achieved and that there was

adequate contrast between embryo and background.

Once projections were acquired, CT 3D Pro (Version 6.8.7977.22560; Nikon

Metrology) was used to reconstruct volumes. An automatic search was performed to

identify the dual centers of rotation, and a beam hardening correction of level 2 was

applied for all scans. Volumes were cropped to fit the specimen and to reduce file size,

and scans were exported as both 16-bit VGL files and 16-bit TIFF stacks.

Analysis of 3D Volumes

Reconstructed volumes were imported into VG Studio Max (Version 3.5, Volume

Graphics GnbH), grayscale values were calibrated for material and background, and

those values were mapped to 10,000 and 50,000, respectively. Images from transverse

digital slices were used to examine the developing brain, trigeminal ganglion, CN V_1-V_3, cranial bones, supra- and infralabial scale rows, and pit arrays, and to assess interspecific patterns and timing of development of these structures.

Staging of Embryos

Antaresia childreni embryos were staged from three-dimensional renderings of microCT scan volumes, which allowed for enhanced clarity of the structures of interest required for analysis. In order to facilitate comparisons between the embryos of *A. childreni* and those of the other two species examined, which were available only as histological sections, I used the same staging criteria, that of Zehr (1962) (Table 2.2). For *P. molurus* and *P. regius*, most embryos were allocated to a single stage, with the exception of those indicated as being in a stage between stages 33-35 (Table 2.1). This is due to the fact that the Zehr (1962) staging criteria were intended for staging embryos of the natricine snake, *Thamnophis sirtalis*. Thus, they did not perfectly align with the developmental events taking place from stages 33-35 in pythonid embryos.

RESULTS

Python molurus

Stage 26

At Zehr Stage 26 in *Python molurus*, the trabeculae cranii are visible, but not distinct from the surrounding mesenchyme. The nasal capsule and vomeronasal cartilages have begun to differentiate. Slight thickening of the tissues along the maxillary prominences of the upper jaw mark the incipient formation of the maxillary dental

laminae, which form the maxillary tooth rows. The dental laminae that form the palatine teeth have not yet begun to develop. In the lower jaw, the Meckel's cartilages are just beginning to form. As in the upper jaw, epithelial thickenings dorsomedial to the Meckel's cartilages indicate the formation of the mandibular dental laminae.

The trigeminal ganglia are forming and have separated into their three primary divisions (Fig 2.1.). All three trigeminal rami have begun their rostral extension toward the regions they will ultimately innervate. Both V_1 and V_2 are visible in cross section as far forward as the vomeronasal organ (VNO). The mandibular rami (CN V_3) are visible in the lower jaw and appear in cross-section as small purple circles, in trichrome stain, dorsolateral to the developing Meckel's cartilages (Fig 2.2). No trigeminal nerve branches have yet reached the peripheral tissues, though V_3 is the closest to reaching the region it will ultimately serve. The rostral and two supralabial pits have begun to invaginate (Fig 2.3), but the infralabial pits have not (Fig 2.2.).

Stage 27

The trabeculae cranii and Meckel's cartilages are continuing to form, as are the epithelia of the olfactory organ and the VNO. In the upper jaw, the palatine dental laminae have begun to develop and appear as thickenings of tissues medial to the first dental laminae. Blood islands have begun to form in different regions of the head, including in the mesenchyme underlying the developing supralabial pit organs. The supralabial pits continue to invaginate (Fig. 2.3.), but there is still no evidence of pit formation in the lower jaw (Fig 2.2.). Some sub-branching of V_2 is evident at this stage, although V_2 has not yet reached either of the supralabial pit organs (Fig.2.3). In the lower jaw, V_3 has extended even closer to the regions where the infralabial pit arrays will form,

and it is joined in its journey to the periphery by a cluster of developing blood vessels

(Fig. 2.2). The three divisions of the trigeminal ganglia have become even more distinct

(Fig 2.1), and it appears that the lateral tracts of the trigeminal descendens (LTTD) have

begun to form.

Stage 29

The trabeculae cranii and communis are distinct, and the branches of the

parietotectal cartilages have begun to extend from the anterior of the former. Ossification

centers for the palatine and pterygoid bones are also present. First and second tooth

germs are visible in the maxillary dental laminae. There is evidence of increased

subdivision of the maxillary nerves, which are surrounded by small blood vessels

(Fig.2.3.). Both V_2 and these nearby vessels have begun to extend in earnest toward the

supralabial pits that they ultimately will supply.

In the lower jaw, first and second tooth germs in the mandibular dental laminae

are evident in cross-section, with the first tooth buds just beginning to appear. The pit

organs of the lower jaw have just begun to invaginate, with a thickening of the tissues

evident in the regions where they are forming (Fig 2.2.). The mandibular nerves have

already contacted the tissues in these regions and have begun to branch at this level, and

the blood vessels that underlie the infralabial arrays are also visible at the periphery

(Fig.2.2).

Stage 30

The trigeminal ganglia and nerve roots are further differentiated, and the LTTD is

distinct from the surrounding gray matter (Fig.2.1). In early Stage 30 (day 10) embryos,

the palatine bones have begun to ossify, but there is not yet any evidence of maxillary or premaxillary formation or ossification. By late stage 30 (day 12), ossification centers for the vomer and nasal bones are evident in some sections, though premaxillary and maxillary formation still has not begun. Tooth buds are forming in the maxillary dental laminae. Both the maxillary nerves and the blood supply underlying the supralabial pits have reached the periphery to contact the pits that they serve as early as day 10, and by day 12 the tissues lining the pit organs have begun to thicken and differentiate into more distinct layers (Fig 2.3.).

Pit organ formation in the lower jaw is underway, appearing as a medial folding of the peripheral tissues that can be traced across consecutive sections, and V_3 has begun to branch more extensively as it contacts the peripheral tissues (Fig.2.2). By day 10 the ossification centers for the compound bone appear medial to the Meckel's cartilages, and by day 12 they have progressed laterally, to partially encircle those cartilages. Ossification of the compound bones is first seen in day 12 embryos.

Stage 32

The optic tectum has begun to form in the roof of the mesencephalon in early stage 32 (day 15), and clear layering of this region of the brain is evident by this stage (Fig.2.4). The LTTDs have become much more distinct (Fig.2.4). Ossification of the cranial and facial bones is well underway, as is true for the bones that will surround the trigeminal ganglia.

In the upper jaw, ossification of the maxillary bones has begun by early stage 32 (day 15), and by late stage 32 (day 21) maxillary ossification has progressed even further, although does not yet completely encircle V_2 (Fig.2.3). More blood vessels have

developed in the regions underlying the supralabial pits (Fig.2.3), and the tissues that line those pits are beginning to separate into even more distinct layers.

In the lower jaw, the dentary bones have begun to form medial to the Meckel's cartilages. The compound bones now almost entirely encircle those cartilages and V_3, although they have not yet formed the mandibular foramen (through which V_3 passes to innervate the infralabials in adults) (Fig 2.2.). By late stage 32, both the compound and dentary bones are more completely ossified. The scales hosting the infralabial pit organs have begun to differentiate during this stage, and more blood vessels are evident in the tissues underlying the developing pits (Fig.2.2).

Stage 33-35

In earlier timepoints for this stage (day 28), the optic tectum is distinct and the brain has established a form more similar to that of the adults (Fig.2.4). The laterosphenoid bones surrounding the trigeminal ganglion are ossified by day 28, forming the foramina through which V_2 and V_3 exit the braincase. By day 35, clear layers are evident in the tectum (Fig.2.4).

By day 28, the maxillary bone is clearly ossified, though the foramina through which V_2 passes to innervate the pits do not form until at least day 35. The pit organs of the upper jaw exhibit a distinct layering of the tissues in the pit fundus by day 28 (Fig 2.3). In the lower jaw, the infralabial glands have begun to develop medial to the developing pit organs prior to day 28, with their ducts visible dorsomedial to the pits by day 35. A dense layer of blood vessels is evident between the pits and this gland (Fig 2.2), and V_3 passes under the developing glandular tissues before extending laterally to contact the pits. Clear layers in the pit fundi are evident by day 28 (Fig 2.2). Ossification of the

compound bone is ongoing by day 28, and seemingly is complete by day 35, at which

point the mandibular foramen of the compound bone has fully encircled V_3 as the nerve

exits the compound bone to contact the infralabial pits.

Python regius

Stage 28

Many of the anterior bones of the face and upper jaw that ultimately surround V_1

and V_2 (including the maxilla, premaxilla, and nasal bones) have not yet begun to form.

However, both the developing palatine and pterygoid bones appear ventromedial to the

orbit in their respective locations along the palatal shelf. The trabeculae cranii are

distinct, and the Meckel's cartilages of the lower jaw are present.

By Stage 28, the rostral pit organs have begun to invaginate, as have at least the

first three pairs of supralabial pit organs. Inception of supralabial pit organ invagination is

marked by a thickening of the peripheral ectodermal layer and the appearance of a

collagen matrix underlying the invaginating pit (Fig. 2.5.). V_2 has not yet reached the

periphery but appears adjacent to the developing supralabial pit organs in transverse

sections (Fig.2.5.).

Cranial nerve V_3 is visible in the lower jaw, and has already begun to send

branches toward the tissues where the infralabial pits will eventually form (Fig.2.6). At

this stage, there is no evidence of infralabial pit formation. At the level of the hindbrain,

the trigeminal ganglia have formed, and their divisions into the three main branches are

distinct (Fig 2.7.).

Stage 31

In Stage 31, the optic tectum has begun to differentiate in the roof of the mesencephalon (Fig. 2.8). The LTTDs also appear to be forming during this stage (Fig. 2.8). Mesenchymal condensations indicating the incipient formation of the premaxillae, prior to their fusion, are visible by early stage 31 (day 2). The premaxillae have begun to ossify in transverse sections taken anterior to the nasal capsule later in this stage (day 8). The trabecula cranii is distinct, and the parietotectal cartilages (also distinct in this stage) extend from its anterior region. Ossification centers for the vomer are visible in sections caudal to the VNO by day 2, and the palatine, pterygoid, and ectopterygoids are beginning to ossify by this time. By day 8, ossification centers of the maxillary bones have begun to form around V_2 and its sub-branches (which ultimately reach the supralabial pits via foramina in the maxillae).

While the rostral pit organs are not visible in any sections of this stage (given their position at the front of the rostrum, they are easily missed in transverse sections cut from the tip of the snout), their presence is implied by two distinct aggregations of nerve fibers and blood vessels in sections anterior to the developing nasal capsule as early as day 8 (Fig 2.5.). In these sections, the developing sub-branches of V_1 (which ultimately contact the membranes of the rostral pit fundi in adults) are distinct (Fig. 2.5.). Each is encircled by blood vessels as they extend anteriorly (Fig. 2.5). Invagination of the supralabial pits continues, and the thickened epithelial layer observed in Stage 28 appears as two distinct layers of cells by day 8 (Fig. 2.5.). The subbranches of V_2 that serve the supralabial pits are now visible and approaching the periphery (Fig. 2.5.). The supralabial

pits are visible as a thickening of the peripheral tissues, with a collagen matrix underlying the developing pits just beginning to form by day 8 (Fig. 2.5.).

In the lower jaw, ossification centers for both the compound and dentary bones are visible ventromedial to the Meckel's cartilages by day 2, and ossification had progressed much further by day 8 (although neither of those developing bones fully encircles the Meckel's cartilages by this point). By day 2, V_3 has begun to approach the region where the infralabial pits will form, although has not yet made contact with tissues at the periphery (Fig.2.6.). There is also no noticeable folding of the infralabial tissues at this point. By day 8, sub-branches of V_3 have contacted the periphery, traveling alongside developing blood vessels (Fig.2.6.). A slight depression of the infralabial tissues is evident by this stage, marking the onset of pit organ invagination (Fig.2.6.).

Stage 33-35

By this stage (day 18), the tectum is well developed, and distinct layers are visible in cross-section (Fig. 2.8.). Ossification of the maxillae is much more advanced than in stage 31, though the maxillae have not yet fully encircled V_2**.** The cells lining the rostral pit organ that form the pit membrane, or fundus, have become distinctly columnar. The rostral pit, which was difficult to differentiate in previous stages, is now visible in more sections, indicating an increase both in extent and in depth. All pits in the supralabial array are contacted by the nerve or the nerve sub-branches that innervate them, and the blood vessels underlying the pits are increasingly dense (Fig.2.5). The interiormost cells of the supralabial pit organs have also become much more strongly columnar at this stage (Fig.2.5.). Formation of the terminal nerve masses is underway, and the sub-branch of V_2 that supplies the pits is in contact with this cell layer (Fig.2.5.).

In the lower jaw, both the dentary and compound bones are much more highly ossified than in stage 31, though neither have fully encircled the Meckel's cartilages or V_3. The fold from which the infralabial pits differentiate is much deeper than in late stage 31, and the sub-branches of V_3 are in contact with the peripheral tissues (Fig.2.6.). There is also a dense vascular layer underlying the regions where the pits are forming (Fig.2.6.).

Stage 36

Only one timepoint is represented for stage 36, by embryo collected at day 35 post-oviposition, which is late in stage 36 for this species. Ossification of the cranial and facial bones of the upper jaw is nearly complete, though the top of the braincase still appears to be open. The maxillae now completely encircle V_2, with foramina forming in the rostral extent of this bone, allowing passage of the nerve to the pit organs. There are at least four distinct layers evident in the rostral and supralabial pit organs by this stage, and fiber bundles are evident in each maxillary sub-branch (Fig. 2.5.).

The infralabial pits have fully invaginated, and the scales that harbor them are beginning to differentiate (Fig. 2.6.). Ossification of the dentary and compound bones is complete, and the foramina through which V_3 exits the compound bone to supply the pits has formed around that ramus. As in the rostral and supralabial pits, distinct layers can be seen in the infralabial pits, and small nerve fibers and blood vessels infiltrate the deepest of these layers from below to contact the pit fundus (Fig. 2.6.).

Stage 37

In early stage 37 (day 36), the infralabial pits do not appear to be further developed than those of stage 36. By mid-stage 37 (day 46), the capillary loops

underlying the rostral and supralabial pits are well-developed and are in contact with columnar cells deep to the epithelium of the pit organ. Nerve fibers have invaded this columnar layer, which appears to be organized into the triangular terminal nerve masses (TNMs) described by Amemiya et al. (1996). There is a thick layer of collagen that appears to support the nerves and blood vessels just beneath the level where the blood vessels branch, and a thinner layer supports those branches where they project into the columnar layer as capillary loops. Infralabial pit development appears to be complete, with TNMs evident in cross section.

By late stage 37 (day 61), the dense layer of nerves and blood vessels underlying the rostral and supralabial pits are completely developed, and the thicker and deeper collagen network is still evident deep to the slightly thinner layer of collagen that supports the fine vascular and nervous branches. The terminal nerve masses are present just deep to the epithelium of the pit membrane as a series of triangular structures. Small, clear circles are visible just deep to the TNM layer, and these appear to be the capillary loops that have been reported to be in contact with the TNMs. In the lower jaw, the infralabial gland is fully formed. The pits of the lower jaw are less deeply invaginated than those of the upper jaw, although the layers evident in the rostral and supralabial pits are still visible.

Antaresia childreni

Stage 26

Embryos of *Antaresia childreni* are at a stage equivalent to Zehr Stage 26 on the day of oviposition (day 0). Cranial and cephalic vasculature is already quite prominent,

with developing vessels forming in the rostrum and lower jaw. The nasal capsule and vomeronasal organ have begun to differentiate, and the olfactory nerves have extended from the developing olfactory lobe of the brain to contact those structures. The trabeculae cranii are forming, but are only faintly evident. The maxillary dental laminae are forming at this stage. In the lower jaw, the Meckel's cartilages have begun to form, as have the mandibular dental laminae. V_3 appears dorsal to the developing Meckel's cartilages in cross-section, although it extends only as far forward as the caudalmost edge of the eye (Fig. 2.9.).

Later in this stage (day 1), the first tooth germs are evident in the maxillary dental laminae of the upper jaw, and the inner dental laminae are beginning to form. Ossification of the pterygoid bones has begun, and the faint beginnings of premaxillary bone formation are evident in transverse section. In the lower jaw, the first tooth germs are developing in the mandibular dental laminae, and the Meckel's cartilages have become much more distinct. V_3 extends as far forward as the middle of the eye, and it has begun to reach the peripheral tissues where the infralabial pits will eventually form (Fig. 2.9.).

Stage 27

Only one embryo was available for this stage, collected on at day 2 post-oviposition. In the upper jaw, premaxillary tooth germs are visible. In the lower jaw, shadows around the Meckel's cartilage mark the onset of formation of the compound and dentary bones. While the rostral extent of V_3 does not differ from that observed in Stage 26, it has lateral branches that contact the tissues underlying the region of eventual infralabial pit formation (Fig. 2.9). Developing blood vessels are also evident in the tissues underlying the region of incipient pit organ formation (Fig. 2.9).

Stage 28

Early stage 28 (day 3) is very similar to stage 27. By late stage 28 (day 5) the ossification centers for the palatine bones are evident. The first tooth buds are visible in the maxillary dental laminae of the upper jaw. In the lower jaw, tooth buds are forming on the mandibular dental laminae, and development of the compound bone has progressed. Sub-branching of V_3 has begun (Fig. 2.9).

Stage 29

This stage is represented by an embryo collected on day 7. Development of the pterygoid and palatine bones continues. Maxillary bone formation is also underway, forming around V_2, which now extends as far forward as the caudal margin of the nasal capsule. An egg tooth bud is visible at the ventral midpoint of the premaxillary bone. In the lower jaw, development of the compound bone continues, with ossification centers now encircling V_3, forming a foramen through which this ramus passes to reach the caudal infralabial tissues. No infralabial pits have yet formed, but the tissues in this region appear to be medially depressed, forming a very shallow fold. The optic tectum first begins to differentiate at this stage.

Stage 31

By stage 31, the bones that began forming earlier continue to ossify. The fold in the tissues of the lower jaw, first evident in late Stage 29, has become much deeper and more obvious (Fig.2.10). A layer of blood vessels is developing in the tissues deep to this fold, and sub-branches of V_3 are in contact with these tissues (Fig. 2.9.). It appears that

this folding of the labial tissues marks the inception of infralabial pit invagination. The optic tectum is further developed and is beginning to form distinct layers.

Stage 33

In stage 33 (day 15), ossification is advanced, though not yet complete. Foramina in the mandible have formed to allow passage of nerves and blood vessels to the supralabial scales. Foramina have also formed around V_3 and the mandibular artery as they exit the compound bones and (more rostrally) the dentary bone.

Stage 34

In the earliest embryos from stage 34 (day 17), the bones of both the upper and lower jaws are nearly entirely ossified, although the braincase remains open. The infralabial fold has deepened further, and also appears to be widening ventrally (Fig. 2.10.). Deep to this fold, a thinning of the mesenchyme is evident.

Midway through Stage 34 (day 18), pits have begun to differentiate within the infralabial fold (Fig. 2.10.). The fan-like arrangement of both the mandibular artery and the mandibular vein (which supply and drain the infralabial array, respectively) is visible (Fig. 2.9). On day 19, the margins of the infralabial scales are first evident, indicating that the scales have begun to form around the individual pits (Fig. 2.10.).

Stage 35-37

In early stage 35 (days 21 and 22) the facial bones are fully ossified, as are many of the other cranial bones, though the braincase still has not fully enclosed the brain. The braincase is also not complete dorsally by the end of this stage (day 28), although parietal development is much more advanced by then. The pit organs have continued to deepen,

together with deepening of the scale margins, taking on the more square shape seen in adults of this species (Fig. 2.10.). There appear to be layers of tissues forming in the infralabial pit fundus (as in the other two pythonid species examined) (Fig. 2.11.), although that could not be confirmed due to the limited resolution afforded by microCT scanning of PTA-stained tissues. By stage 36 (day 35) the braincase is fully ossified. Little change is evident in the infralabial pits from the onset of stage 36 through hatching, which occurs at stage 37.

DISCUSSION

Development of the trigeminal ganglia and the three primary trigeminal rami is well advanced by day of oviposition in all taxa examined (Stage 26 in *A. childreni*, Stage 26 in *P. molurus*, and Stage 28 in *P. regius*). Trigeminal development begins both before the development of the cranial and facial bones, and before differentiation of the optic tectum in the roof of the mesencephalon (which begins at Stage 35 in *A. childreni*, Stage 32 in P. *molurus*, and Stage 31 in *P. regius*). Timing of the onset of trigeminal development is consistent with observations in *Crotalus atrox* and *Agkistrodon contortrix* (Savitzky, 1992). It is not clear when development of these structures begins, although given the degree of division and branching evident at oviposition, it is likely to have begun several days prior to that event.

Pit organs in the upper jaw in both *Python regius* and *P. molurus* appear to invaginate before either nerves or blood vessels contact the peripheral tissues, and the pit organs develop in series from rostral to caudal, as previously described by Savitzky (1985). The supralabial pits are evident under microscopic examination as early as the day of oviposition (stage 28 in *P. molurus* and stage 26 in *P. regius*). Savitzky (1985)

noted that those pits are macroscopically visible between stages 30 through 33 in *P. regius*, which is the point at which they begin to become much deeper, with thickening of the tissues that ultimately form the pit fundus. The ophthalmic and maxillary nerves reach the rostral and supralabial pits, respectively, by Stage 30 in *P. molurus*. This is first evident in histological sections at Stage 31 in *P. regius*, for which neither Stage 29 nor Stage 30 was available. Thus, it is possible that V_1 and V_2 reach the pits they innervate sometime prior to Stage 31, but this could not be confirmed with the available histological material. This occurs prior to the formation of the maxillary bones. As maxillary development proceeds, so too does development of the pit organs. The supralabial pits become much deeper and begin to exhibit distinct layers of tissues within the pit fundus. Development of the pits on the upper jaw is ongoing throughout all stages of post-ovipositional development, continuing to deepen and increase in both innervation and blood supply through late stage 37.

Savitzky (1992) reported the earliest evidence of loreal pit formation in the crotaline vipers *C. atrox* and *A. contortix* in Stage 27. Silva et al. (2023) briefly compared loreal pit organ development in pitvipers to that of the supralabial and rostral pit arrays of pythons and concluded that pit development in *Bothrops atrox* begins at stage 28, but does not occur until stage 35 in pythons generally. This assertion was reportedly based on a single study of development in *P. sebae*, although the paper cited (Buchtova et al., 2007) does not address pit organ development at all, but rather describes development of the cranial and facial bones for that species. Thus, the findings in this study directly contradict the report by Silva et al. (2023). Rather than occurring much later than that of the pitvipers, pit organ development in the upper jaw of pythons begins

as early as that of pitvipers, if not earlier. Invaginating rostral and supralabial pits are evident on the day of oviposition, and thus invagination of the pits presumably begins while the eggs are *in utero*, prior to oviposition.

Development of the infralabial array appears to follow a different timeline than that of the rostral and supralabial pit organs. In the lower jaws of all taxa examined, the nerves reach the periphery well before the onset of pit organ formation, and prior to any evidence of compound bone development. Rather than forming in series, the infralabial pits are first evident as a longitudinal fold (evident in all taxa beginning at approximately Zehr Stages 30-31). Although it was difficult to visualize the differentiation of the pits within this fold in histological sections of *P. regius* and *P. molurus*, it was very clear in 3D renderings of the microCT scans of *A. childreni*. The fold represents the onset of pit invagination in the lower jaw and begins to form after V_3 contacts the peripheral tissues in this region (which occurs at Stage 29 in *P. molurus*, stage 31 in *P. regius*, and Stage 28 in *A. childreni*). In the 3D renderings of *A. childreni,* the fold is first evident at day 10 (Stage 31) and persists through day 15 (stage 33). Day 18 (early stage 34) marks the initial onset of pit differentiation and occurs prior to the formation of the infralabial scales within which these pits eventually come to lie. By day 19 (late Stage 34), the infralabial scale margins are weakly visible, and from that point onward pit formation occurs with further differentiation of the infralabial scales.

Although these observations do not strongly confirm the hypothesis that hypertrophy of the teeth and pit organs of the upper jaw are developmentally linked (as first proposed by Savtizky, 1992), they do lend further support to that hypothesis. Hypertrophy of the pit organs and the adjacent dentition in pythons appears limited to

those pits and teeth innervated by V_1 and V_2. The pit arrays of the upper jaw form earlier

in development, prior to the time at which the nerves that ultimately innervate them have

made contact. Each pit forms independently in a series from rostral to caudal, with the

deepest pits forming first. The teeth of the premaxillary and maxillary bones share

innervation with these pits and similarly decrease in size from rostral to caudal.

Conversely, the caudal dentition of the dentary bone medial to the infralabial pit array is

not enlarged, even when robust pits are present (as in *A. childreni*). The pits of the lower

jaw form later in development, after their constituent tissues have already received

substantial innervation from V_3. Additionally, the pits of the infralabial array form from a

single deep invagination of the caudal infralabial tissues, which later differentiates into

individual pits as the infralabial scales themselves form. The observed differences in the

timing of contact by the trigeminal rami and the onset of pit invagination in the upper and

lower jaws, coupled with the differences in the mode of pit formation between the two

arrays, is noteworthy. These observations suggest that there is a decoupling of

development between the pit arrays in the upper and lower jaws of pythons.

40

TABLES AND FIGURES

Table 2.1. Developmental stages, stains, and sectioning planes for histological slides of *Python molurus* and *P. regius* embryos.

Taxon	USNM Catalog #	AHS Lab #	Zehr Stage	Day Post-ovipositon	Plane of Sectioning
Python molurus	595195	187	26	0	transverse
	595196	188	27	2	transverse
	595197	189	29	7	transverse
	595198	190	30	10	transverse
	595199	191	30	12	transverse
	595200	192	32	15	transverse
	595201	193	32	21	transverse
	595202	194	33-35	28	transverse
	595203	195	33-35	35	transverse
Python regius	595212	204	28	0	frontal
	595218	210	31	2	transverse
	595219	211	31	8	transverse
	595221	213	33-35	18	transverse
	595222	214	36	35	transverse
	595223	215	37	36	transverse
	595226	218	37	46	transverse
	595229	221	37	61	transverse

Table 2.2 *Antaresia childreni* embryo collection data, including maternal (dam) identification number, day collected post-oviposition, and developmental stage.

Dam ID #	Specimen ID #	Day Collected Post-ovipositon	Developmental Stage
F47	f47d0	0	26
F56	f56d0	0	26
F52	f52d1	1	26
F18	f18d1	1	26
F24	f24d2	2	27
F29	f29d3	3	28
F8	f8d3	3	28
F52	f52d5	5	28
F16	f16d6	6	29
F10	f10d7	7	29
F52	f52d10	10	31
F10	f10d11	11	31
F16	f16d14	14	32
F52	f52d15	15	33
F16	f16d17	17	34
F52	f52d18	18	34
F10	f10d19	19	34
F8	f8d21	21	35
F52	f52d22	22	35
F52	f52d26	26	35
F8	f8d27	27	35
F16	f16d28	28	35
F10	f10d35	35	36
F16	f16d36	36	36
F8	f8d45	45	37-hatch
F10	f10d47	47	37-hatch
F16	f16d49	49	37-hatch
F52	f52d50	50	37-hatch

Table 2.3. MicroCT scan parameters for embryos of *Antaresia childreni.*

Specimen ID #	Beam Energy (kV)	Beam Current (μA)	Pixel Spacing (μm)	Exposure (ms)	Gain (dB)
f47d0	135	19	2.5	1000	18
f56d0	85	82	3	1415	24
f52d1	85	82	3	1415	24
f18d1	135	19	2.5	1000	18
f24d2	135	19	2.5	1000	18
f29d3	135	19	2.5	1000	18
f8d3	80	88	5	1415	24
f52d5	135	19	2.5	1000	18
f16d6	135	22	3	1000	18
f10d7	80	88	4.5	1000	18
f52d10	80	88	4.5	1000	18
f10d11	80	88	4.5	1000	18
f16d14	80	88	4.5	1000	18
f52d15	80	88	4.5	1000	18
f16d17	80	88	4.5	1000	18
f52d18	80	88	4.5	1000	18
f10d19	80	88	5	1000	18
f8d21	80	79	6	1000	18
f52d22	80	88	6.5	1000	18
f52d26	200	60	7.5	500	24
f8d27	110	68	7.5	1000	12
f16d28	200	65	6	500	24
f10d35	85	118	10	1000	24
f16d36	80	125	10	1000	24
f8d45	80	88	6	1415	24
f10d47	200	60	6	500	24
f16d49	80	88	7.5	1415	24
f52d50	80	88	6	1415	24
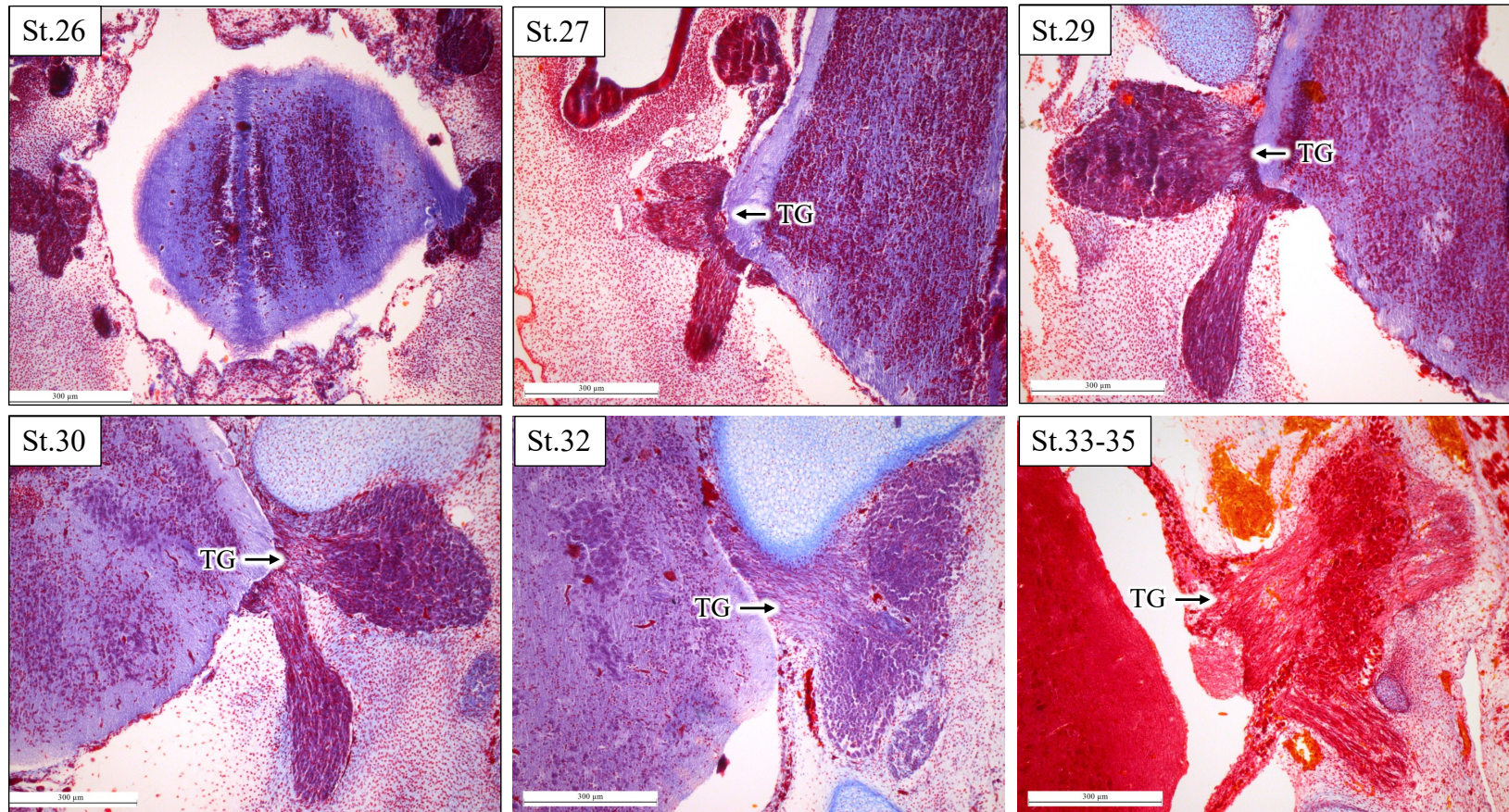
Fig.2.1. Development and differentiation of the trigeminal ganglion (TG, indicated with arrows) in *Python molurus* embryos at Zehr-equivalent stages 26, 27, 29, 30, 32, and 33-35. Scale bars indicate 300μm.
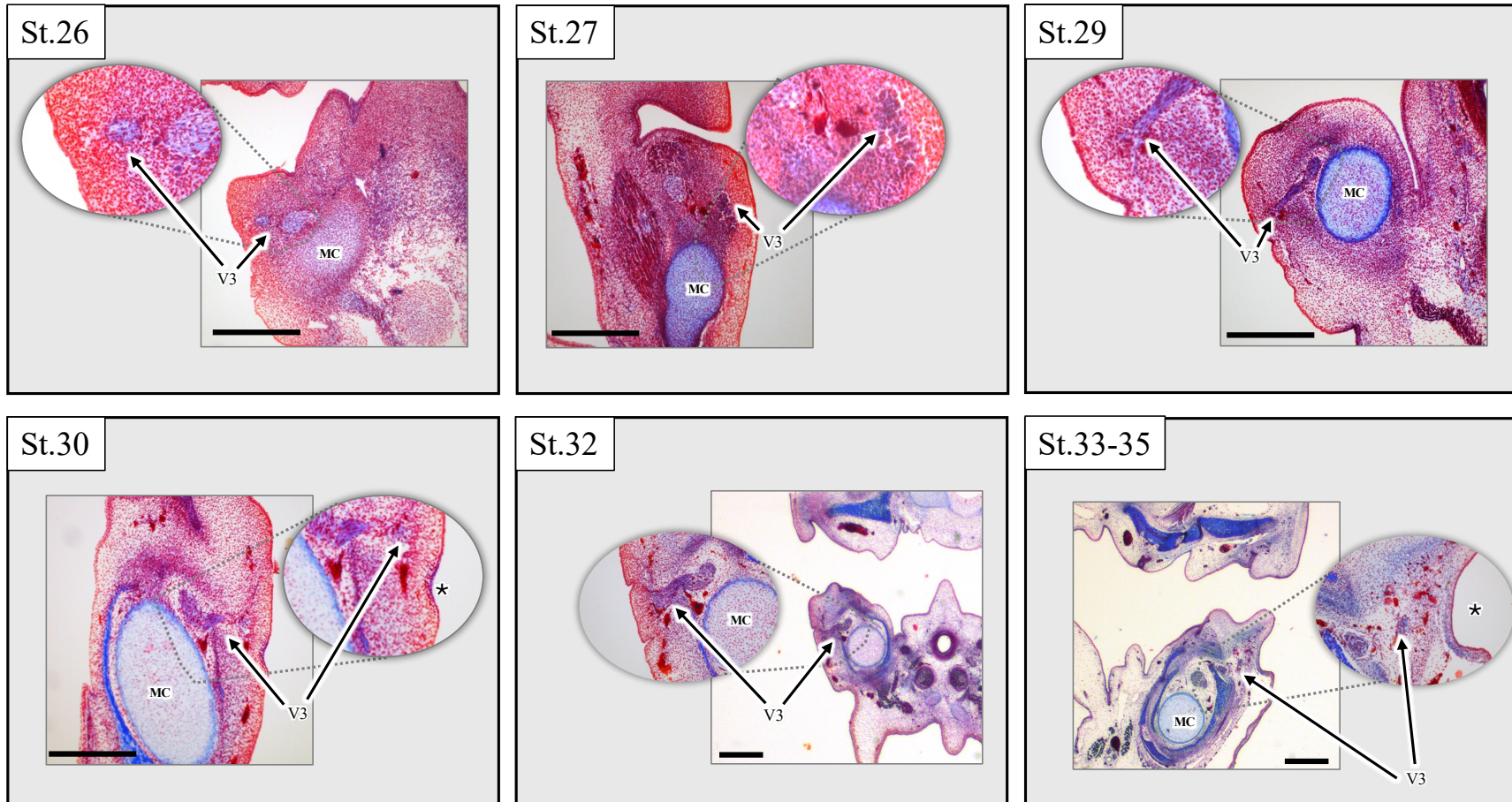
Fig. 2.2. Development of the infralabial pit organs and mandibular branch of the trigeminal nerve (which appears purple when stained with Crowder's Trichome) in *Python molurus*. The mandibular nerve is in contact with the periphery by stage 27, whereas pit organ invagination does not begin until stage 29. (asterisks indicate invaginating pit organs; V_3, mandibular branch of the trigeminal nerve; MC, Meckel's cartilage). Scale bars indicate 200μm.
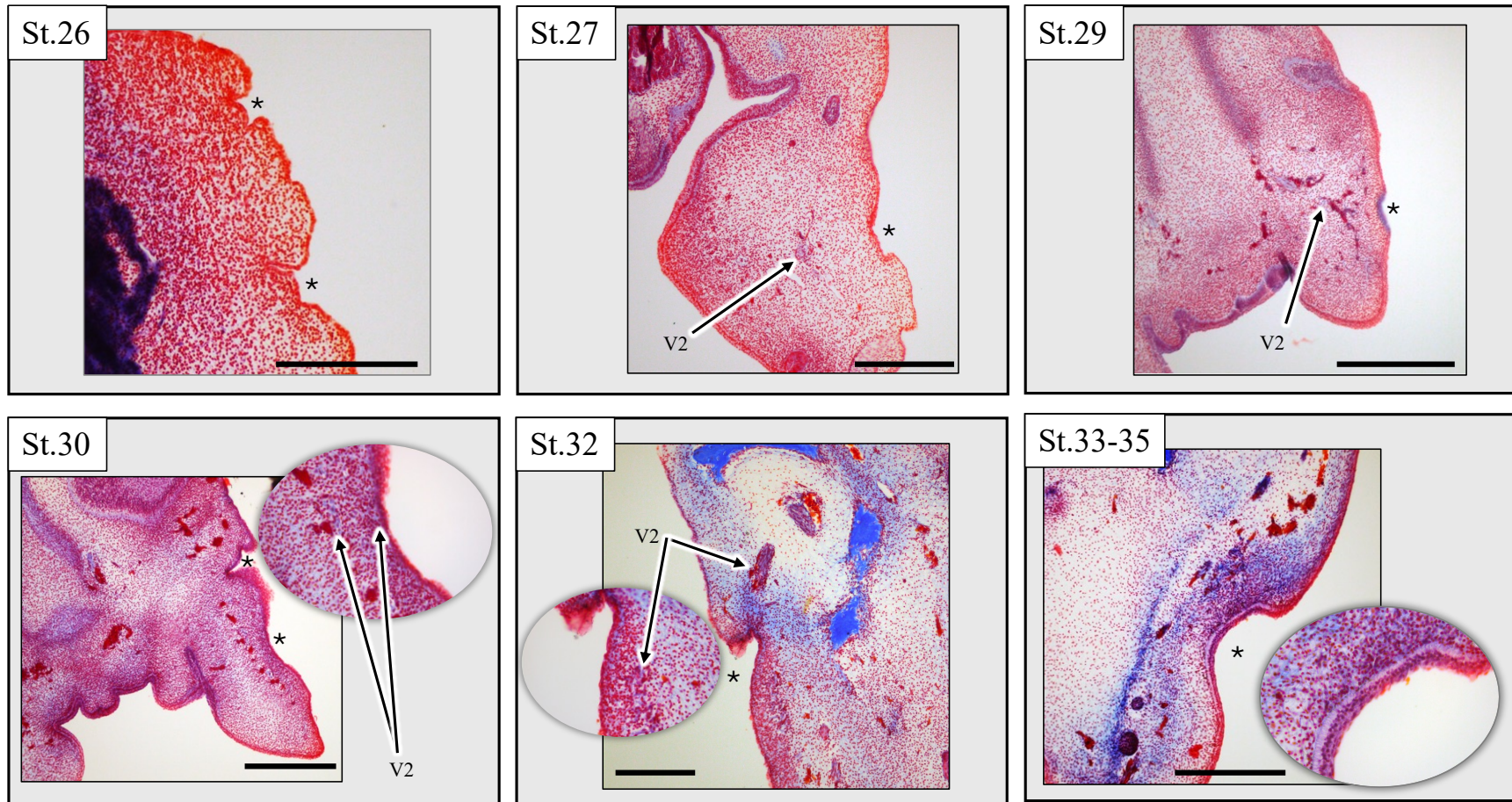
Fig. 2.3. Development of the supralabial pit organs and maxillary branch of the trigeminal nerve (which appears purple when stained with Crowder's Trichome) in *Python molurus* at stages 26, 27, 29, 30, 32, and 33-35. Supralabial pit organs are invaginating in stage 26 embryos, collected at day of hatching, and pit organ development continues through at least the latest stage available (St. 33-35). Nerves approach the periphery as early as stage 27, but do not contact the developing integument until stage 30 or slightly earlier. (asterisks indicate invaginating pit organs; V_2, maxillary branch of trigeminal nerve). Scale bars indicate 200μm.
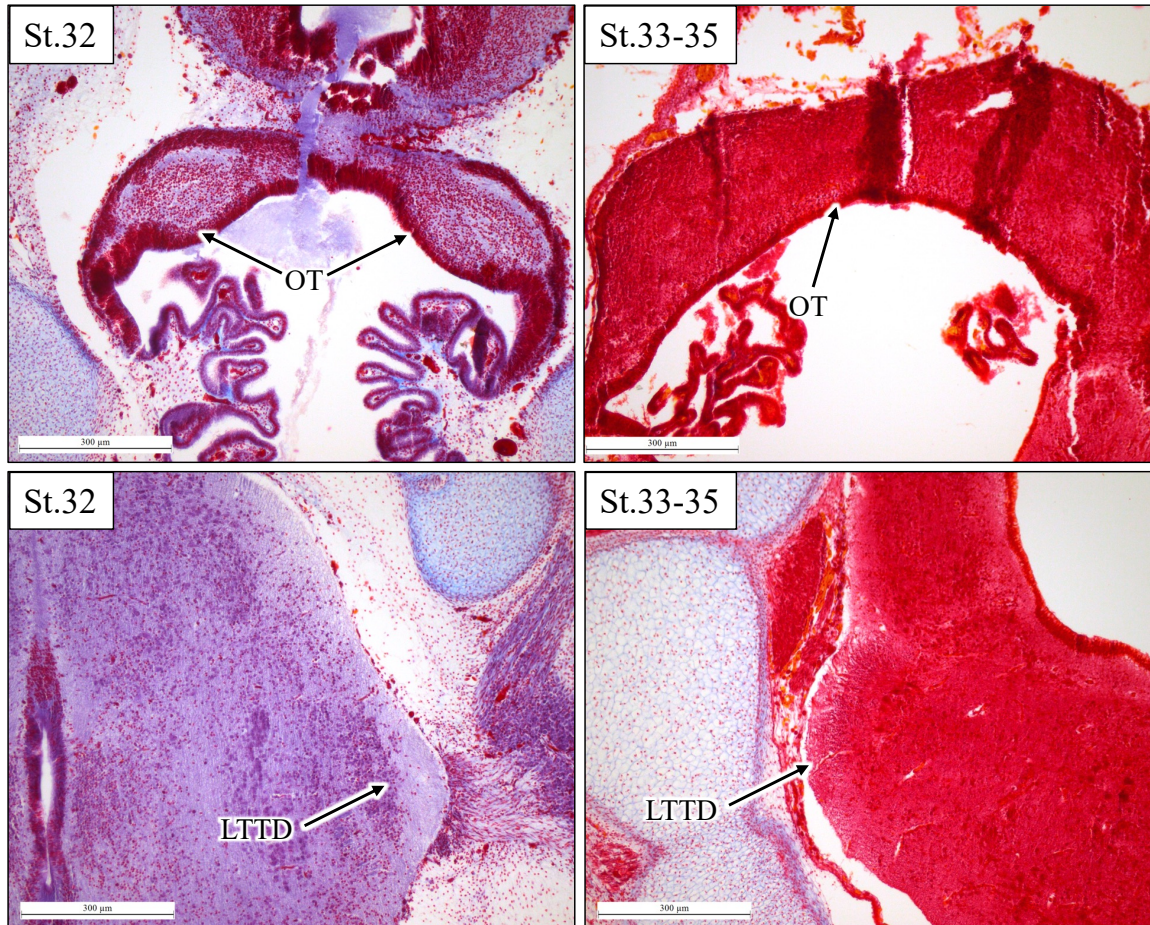
Fig. 2.4. Development and differentiation of the optic tectum (OT; top row) and lateral tract of the trigeminal descendens (LTTD; bottom row) in *Python molurus* embryos at Zehr-equivalent stages 32 and 33-35. Scale bars indicate 300μm.
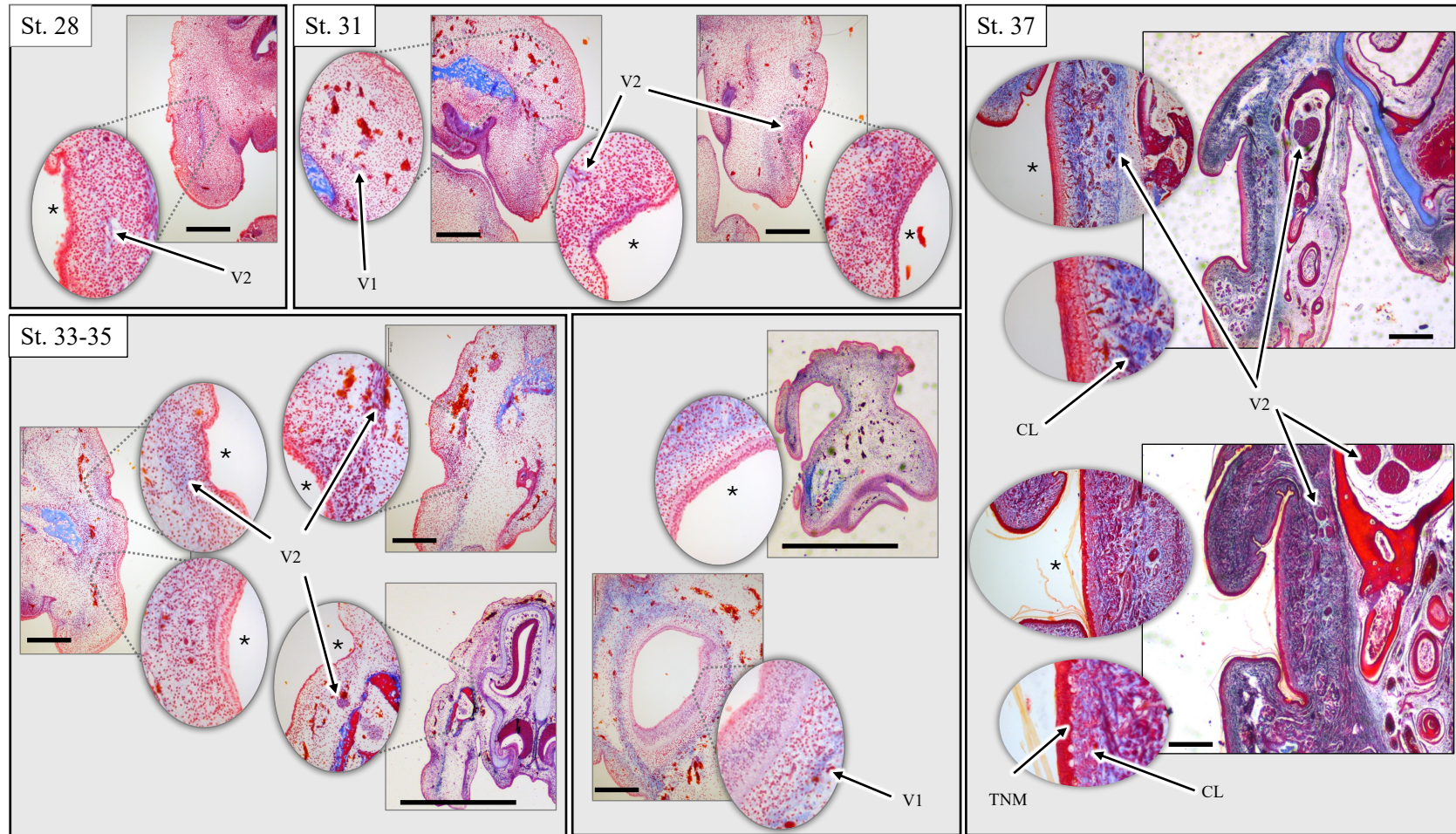
Fig. 2.5. Development of the supralabial pit organs and maxillary branch of the trigeminal nerve in *Python regius*. The pit organs begin invaginating by stage 28, with trigeminal nerve branches approaching the periphery by stage 31. The nerves do not reach the periphery until stage 33-35. Capillary loops are in contact with the terminal nerve masses by Stage 37 (asterisks indicate invaginating pit organs, V_1, ophthalmic branch of trigeminal nerve; V_2, maxillary branch of trigeminal nerve; TNM, terminal nerve mass; CL, capillary loops). Scale bars indicate 200μm.
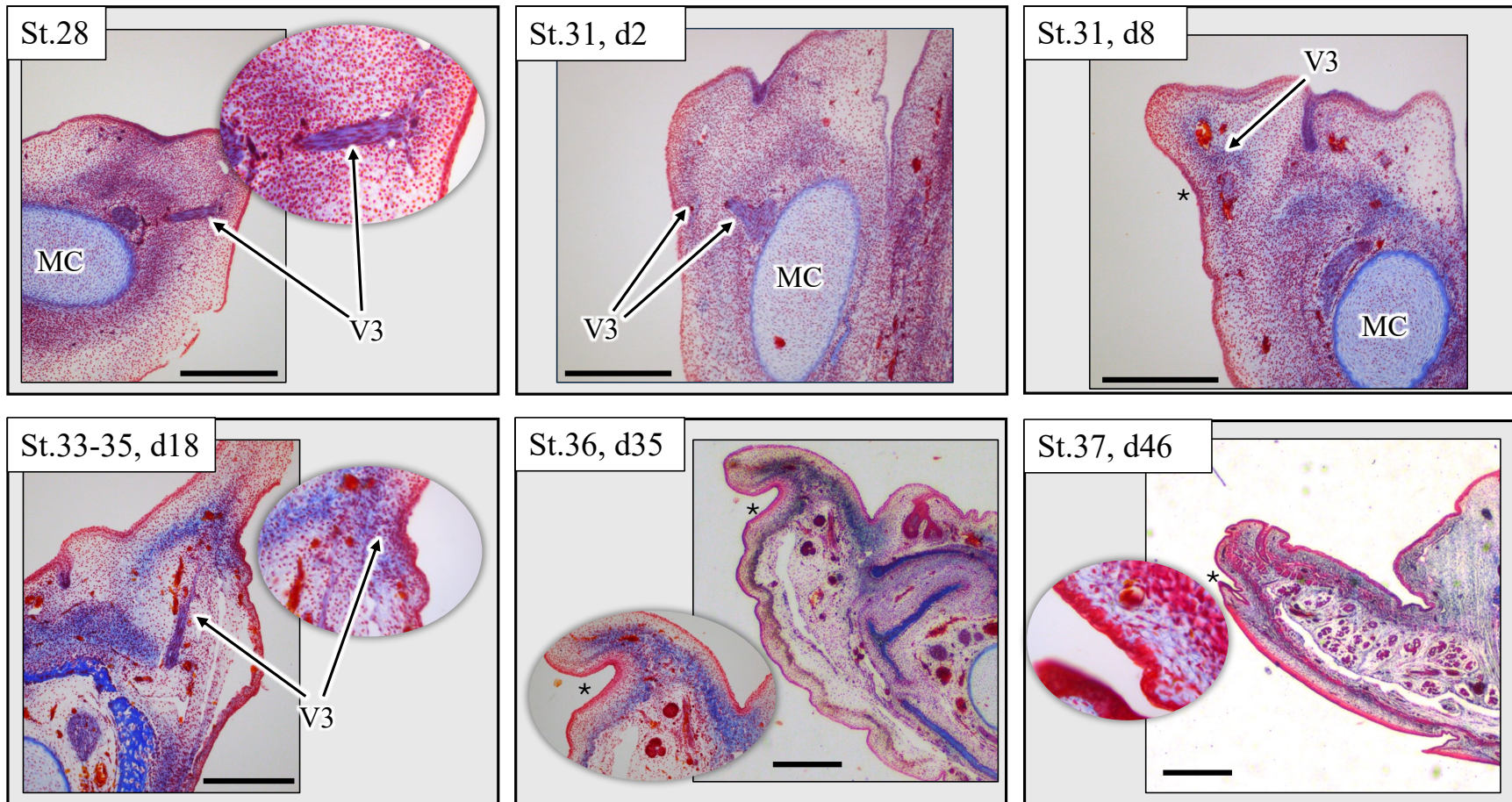
Fig. 2.6. Development of the infralabial pit organs and mandibular branch of the trigeminal nerve (which appears purple when stained with Crowder's Trichome) in *Python regius*. The mandibular nerve is in contact with the periphery by stage 28, whereas invagination of the pit organ does not begin until stage 31. (asterisks indicate invaginating pit organs; V₃, mandibular branch of trigeminal nerve; MC, Meckel's cartilage). Scale bars indicate 200μm.
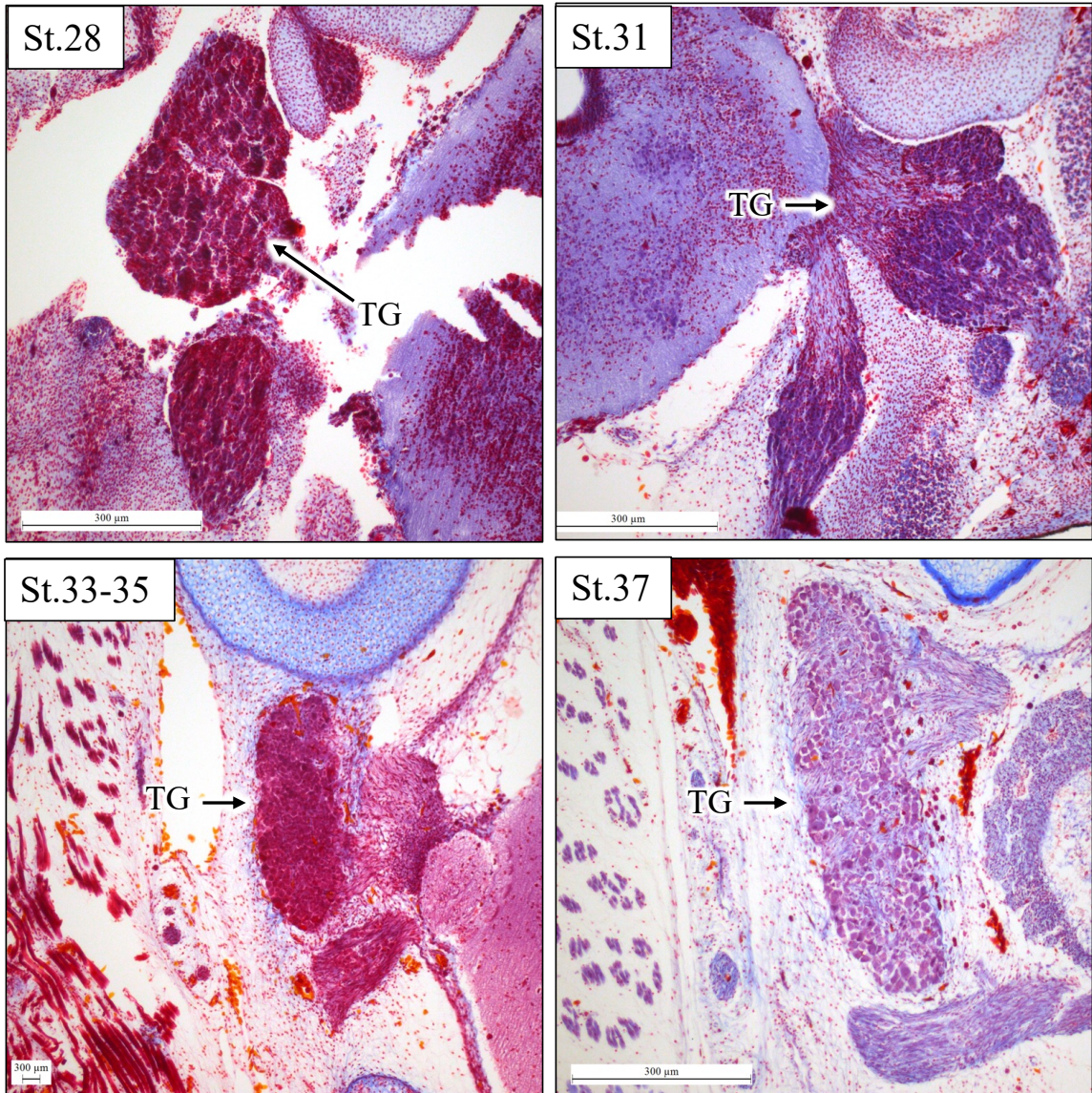
Fig. 2.7. Development and differentiation of the trigeminal ganglion (TG, indicated with arrows) in *Python regius* embryos at Zehr-equivalent stages 28, 31, 33-35, and 37. Scale bars indicate 300μm.
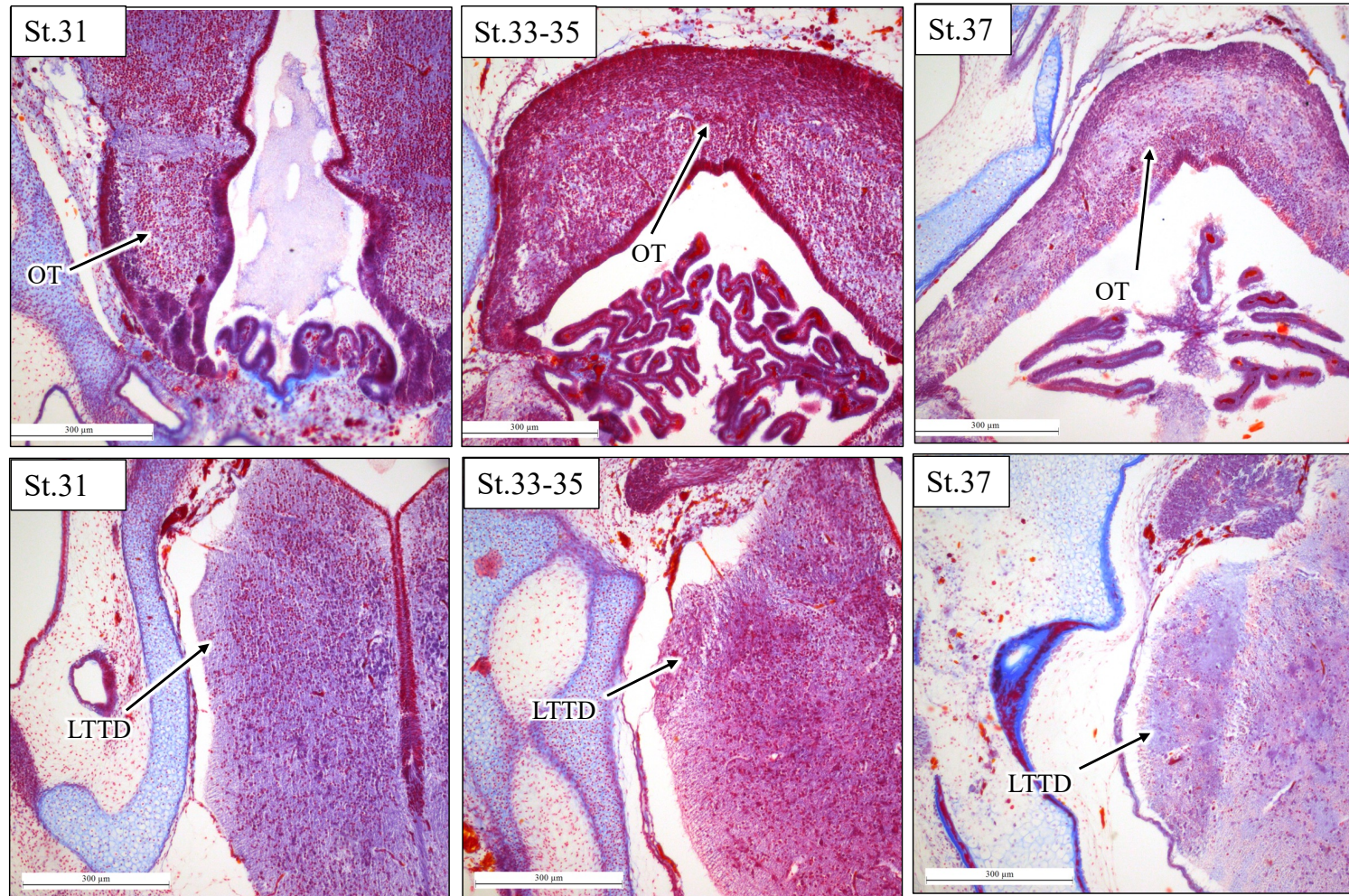
Fig. 2.8. Development and differentiation of the optic tectum (OT; top row) and lateral tract of the trigeminal descendens (LTTD; bottom row) in *Python regius* embryos at Zehr-equivalent stages 31, 33-35, and 37. Scale bars indicate 300μm.
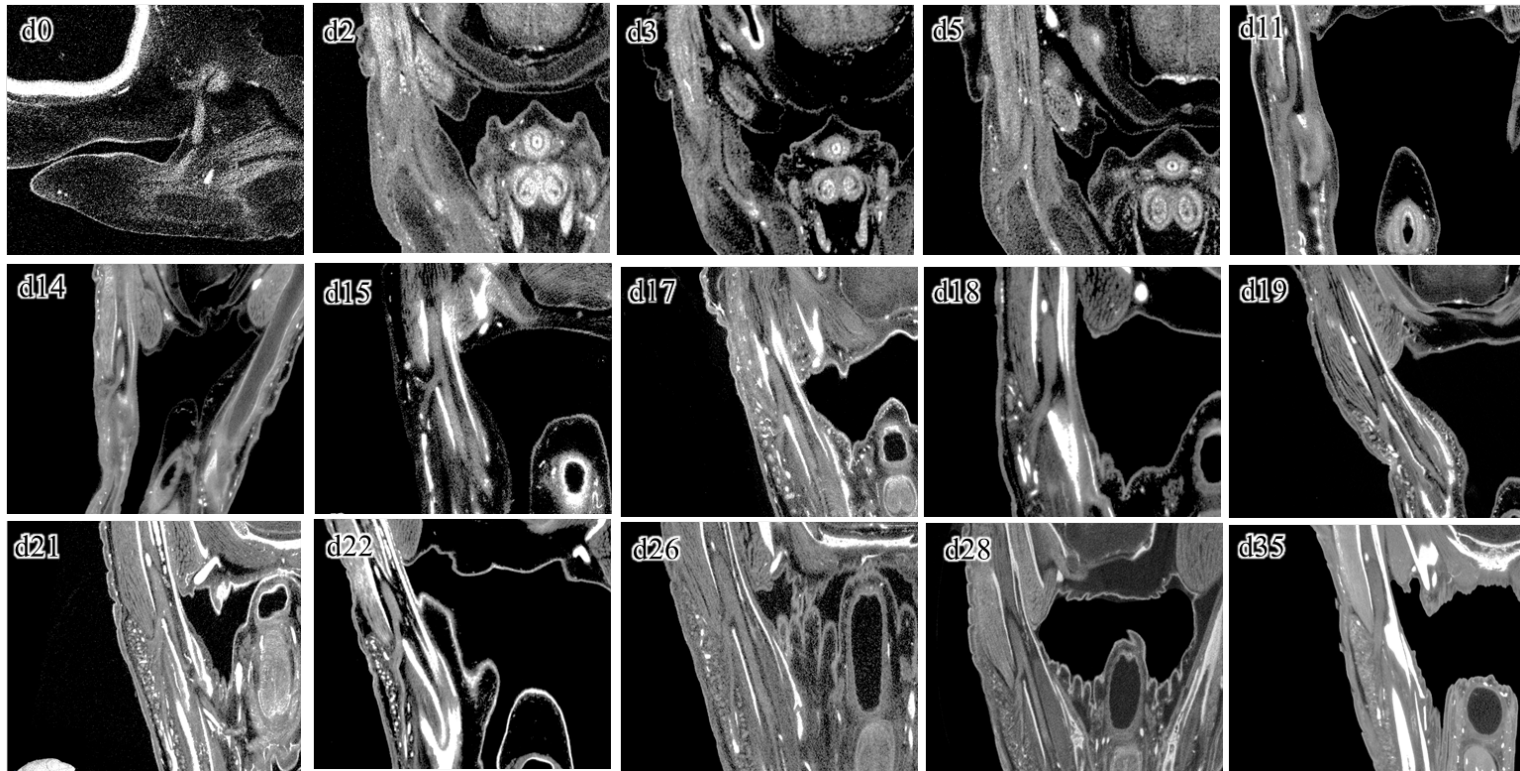
Fig. 2.9 Transverse sections from microCT volumes showing the development and differentiation of the mandibular branch of the trigeminal nerve (V₃) in embryos of *Antaresia childreni* at 15 post-ovipositional timepoints. Day 0 is shown in the sagittal plane, while the remaining timepoints are shown in the transverse plane. Arrows point to the primary branch of the mandibular nerve, with brackets indicating the peripheral terminations of the nerve's sub-branches.
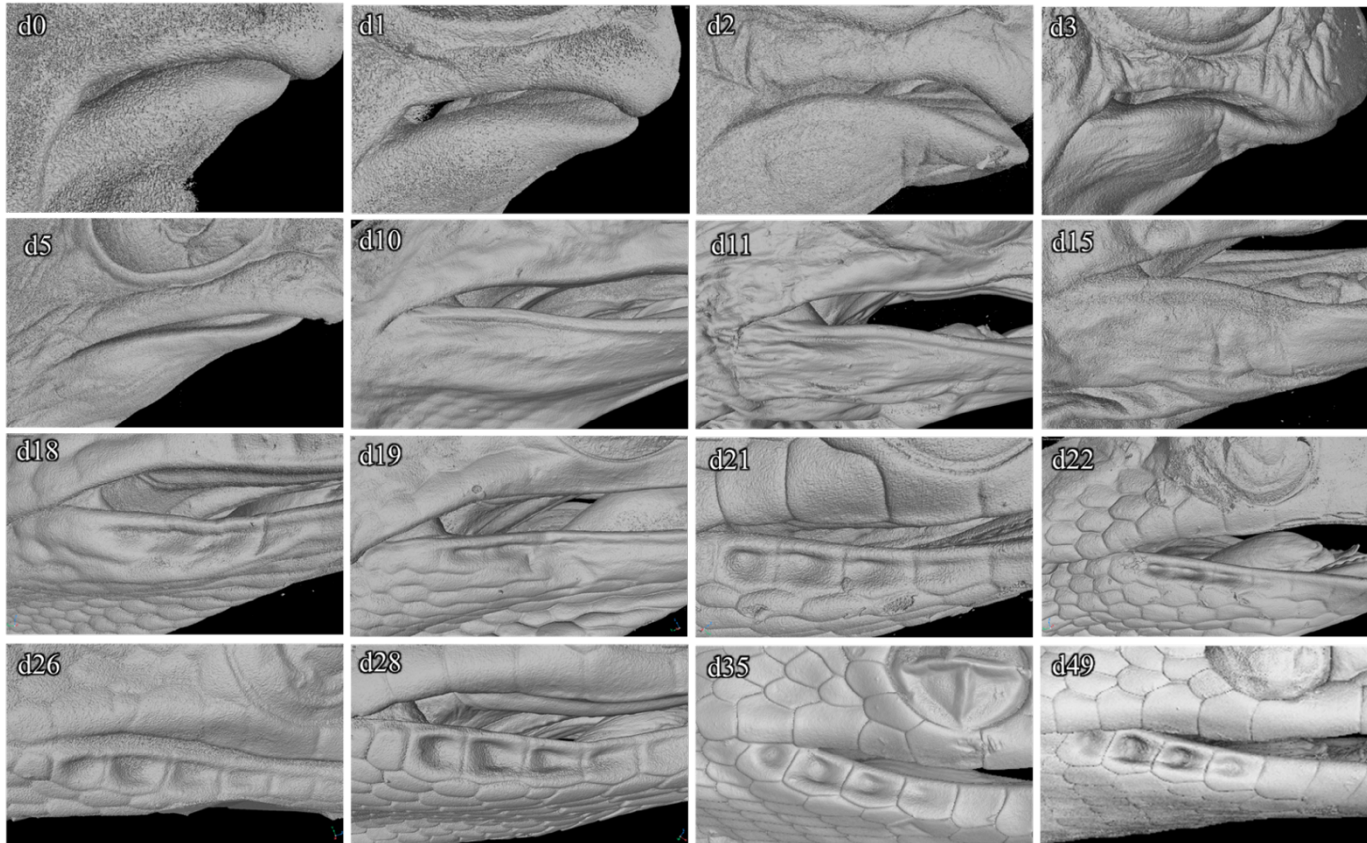
Fig. 2.10. MicroCT volume renderings depicting development and differentiation of the infralabial pit array and infralabial scales in the lower jaw of *Antaresia childreni* at 16 post-ovipositional timepoints (d = day post-oviposition, with d0 representing day of oviposition and d49 representing day of hatching). A bracket is drawn for d10 (stage 31), to indicate the appearance of a longitudinal fold within which the pit organs (indicated by blue arrows) begin to differentiate by d18 (mid-stage 34). The scale margins (indicated by red arrows) emerge by d19 (late stage 34) and are obvious by d21 (early stage 35). The pits continue to deepen and differentiate through hatching (represented by d49)
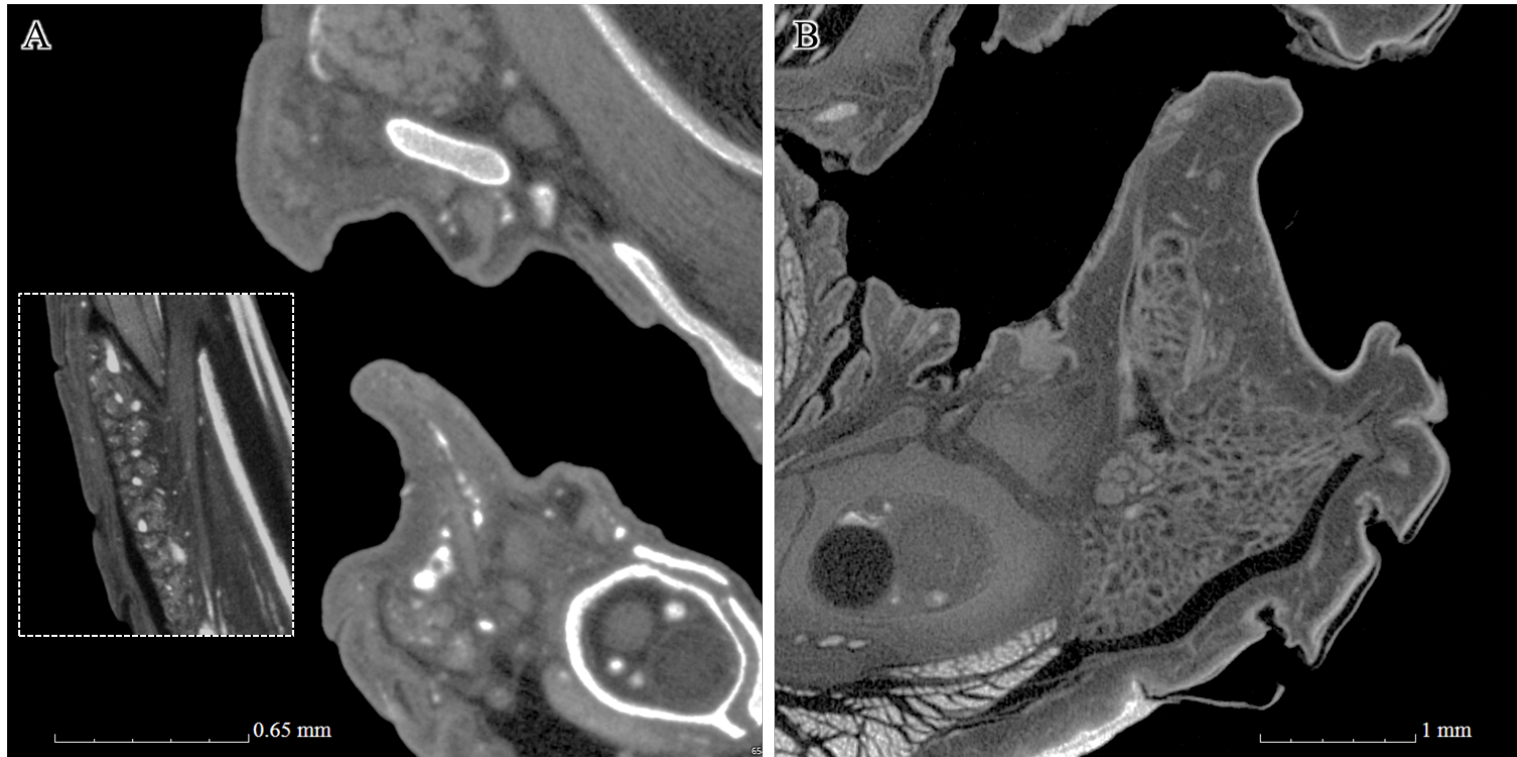
Fig. 2.11. Frontal sections from microCT volumes, showing the arrangement of nerves and blood vessels to the third infralabial pit organ of *Antaresia childreni* at (A) day 35 of post-ovipositional embryonic development and (B) in an adult. The inset image in (A) shows the association of nerves and blood vessels with the developing glandular tissue, which forms ventrolateral to the pit arrays of the lower jaw.

REFERENCES

Bullock, T. H., and F. P. J. Diecke. 1956. Properties of an infra-red receptor. The Journal of Physiology, 134(1): 47-87.

Bullock, T.H., and W. Fox, 1957. The anatomy of the infra-red sense organ in the facial pit of pitvipers. Quarterly Journal of Microscopical Science 98(2): 219-234.

Crowder, C. H. (1983). The trichrome stain: a modification. Journal of Histotechnology, 6(3), 133-134.

de Cock Buning, T.J.., and P. Dullemeijer. 1977. Thermal receptors in Python reticulatus. Acta Morphologica Neerlando-Scandinavica 15: 237–239.

Dullemeijer, P. (1959). A comparative functional-anatomical study of the heads of some Viperidae. Gegenbaurs Morphologisches Jahrbuch 99, 881–985.

Ebert, J. (2007). Infrared sense in snakes (Doctoral dissertation, Universitäts-und Landesbibliothek Bonn).

Gracheva, E. O., N. T. Ingolia, Y.M. Kelly, J.F. Cordero-Morales, G. Hollopeter, A. T. Chesler, and D. Julius. 2010. Molecular basis of infrared detection by snakes. Nature, 464(7291): 1006-1011.

Haseltine, E. C. 1978. Infrared and Visual Organization of the Tectum of Boid Snakes. Unpubl. Ph.D. diss., Indiana University, Bloomington.

Hofstadler-Deiques C. The development of the pit organ of Bothrops jararaca and Crotalus durissus terrificus (Serpentes,Viperidae): support for the monophyly of the subfamily Crotalinae. Acta Zool. 2002;83(3):175-18.

Humason, G. L. (1979). Animal tissue techniques. Animal tissue techniques, 4th ed. W.H. Freeman, San Francisco. 661

Gruberg, E. R., E. Kicliter, E. A. Newman, L. Kass, and P. H. Hartline. 1979. Connections of the tectum of the rattlesnake Crotalus viridis: an HRP study. Journal of Comparative Neurology, 188(1): 31-41.

Kishida, R., F. Amemiya, T. Kusunoki, and S. I. Terashima. 1980. A new tectal afferent nucleus of the infrared sensory system in the medulla oblongata of Crotaline snakes. Brain Research, 195(2): 271-279.

Kohl, T., Bothe, M. S., Luksch, H., Straka, H., & Westhoff, G. (2014). Organotopic organization of the primary Infrared Sensitive Nucleus (LTTD) in the western diamondback rattlesnake (Crotalus atrox). *Journal of Comparative Neurology*, *522*(18), 3943-3959.

Lynn, W.G. (1931). The structure and function of the facial pit of the pitvipers. American Journal of Anatomy 49: 97-139.

Maderson, P. F. A. (1970). The distribution of specialized labial scales in the boidae. Biology of the Reptilia, Vol. 2. (Gans, C. and Pearsons, TS ed.). 301-304.

Meszler, R. M. 1983. Fine structure and organization of the infrared receptor relays: lateral descending nucleus of V in Boidae and nucleus reticularis caloris in the rattlesnake. Journal of Comparative Neurology, 220(3): 299-309.

Meszler, R.M., C. R. Auker, and D. O. Carpenter. 1981. Fine structure and organization of the infrared receptor relay, the lateral descending nucleus of the trigeminal nerve in pitvipers. Journal of Comparative Neurology, 196: 571-584

Metscher, B. D. (2011). X-ray microtomographic imaging of intact vertebrate embryos. Cold Spring Harbor Protocols, 2011(12), pdb-prot067033.

Molenaar, G. J. 1974. An additional trigeminal system in certain snakes possessing infrared receptors. Brain Research, 78: 340-344.

Newman, E. A., E. R. Gruberg, and P. H. Hartline.1980. The infrared trigemino-tectal pathway in the rattlesnake and in the python. Journal of Comparative Neurology, 191(3): 465-477.

Newman, E. A., and P. H. Hartline. 1981. Integration of visual and infrared information in bimodal neurons in the rattlesnake optic tectum. Science, 213(4509): 789-791.

Preibisch, S., Saalfeld, S., & Tomancak, P. (2009). Globally optimal stitching of tiled 3D microscopic image acquisitions. Bioinformatics, 25(11), 1463-1465.

Ros, M. (1935). Die Lippengruben der Pythonen als Temperaturorgane. Jenaische Zeitschrift für Naturwissenschaft, 70: 1-32.

Savitzky, A. H. (1985). Development of the Thermoreceptive Pit Organs in the Boid Snake Python regius. *American Zoologist 25*(4):563.

Savitzky, A. H. (1992). Embryonic development of the maxillary and prefrontal bones of crotaline snakes. The Biology of Pitvipers, 119-141.

Schroeder, D. M., and M. S. Loop. 1976. Trigeminal projections in snakes possessing infrared sensitivity. Journal of Comparative Neurology, 1691: 1-14.

Silva, F. M., Guerra-Fuentes, R. A., Blackburn, D. C., and Prudente, A. L. C. (2023). Embryonic development of the neotropical pit viper Bothrops atrox (Serpentes: Viperidae: Crotalinae), with emphasis on pit organ morphogenesis and its evolution in snakes. *Developmental Dynamics*.

Stanford, L. R., D. M. Schroeder, and P. H. Hartline. 1981. The ascending projection of the nucleus of the lateral descending trigeminal tract: A nucleus in the infrared system of the rattlesnake, Crotalus viridis. Journal of Comparative Neurology, 201(2): 161-173.

Tan, C. K., and P. Gopalakrishnakone. 1988. Infrared sensory neurons in the trigeminal ganglia of the python (Python reticulatus)—a horseradish peroxidase study. Neuroscience letters, 86(3): 251-256.

Terashima, S. I., and R. C. Goris. 1975. Tectal organization of pitviper infrared reception. Brain Research, 83: 490-494.

Terashima, S. I., and R. C. Goris. 1977. Infrared bulbar units in crotaline snakes. Proceedings of the Japan Academy, Series B, 53(7): 292-296.

Terashima, S., and Liang, Y. F. (1991). Temperature neurons in the crotaline trigeminal ganglia. Journal of neurophysiology, 66(2), 623-634.

CHAPTER 3

MORPHOLOGY OF THE TRIGEMINAL NERVE AND ITS INNERVATION OF THE PIT ORGANS IN PYTHONS AND BOAS

INTRODUCTION

As in all vertebrate taxa, the trigeminal nerve (cranial nerve V) innervates the oro- and cranio-facial regions of snakes, including the dentigerous (toothed) bones and teeth, and the tissues of the supra- and infralabial scale rows and rostrum. Cranial nerve (CN) V also provides afferent innervation to specialized cephalic sensory organs in some snakes, such as the rostral tentacles of *Erpeton tentaculatum* (Catania et al., 2010), the oral papillae of sea snakes (Burns, 1969) and snakes generally (Nishida et al., 2000), and the pit organs of IR-imaging taxa (Lynn, 1931; Bullock and Fox, 1957; Kishida et al., 1982). The pit organs are located either within or between the scales of the loreal (pitvipers) or labial (boas, pythons) region, which are served by CN V, independent of the presence or absence of IR-imaging ability. Thus, the sensory organs of the IR-imaging system have co-opted an existing pattern of craniofacial innervation by CN V, improving on its existing somatosensory capabilities through the evolution of densely innervated, directional sensory organs, wherein free nerve endings terminate essentially directly in the surficial tissues as expanded terminal nerve masses (TNMs). These modifications allow both the detection of proximal sources of radiant heat (a common ability in vertebrates and invertebrates alike) and heat at a distance.

The loreal pits of pitvipers are served by both the ophthalmic nerve (V_1), and the superficial and deep branches of the maxillary nerve (V_2) (Lynn, 1931; Bullock and Fox, 1957; de Cock Buning et al., 1981; Goris et al., 1989; Kohl et al., 2014). Neural tracing

studies in pitvipers have revealed a partitioning of the pit membrane into three distinct sensory regions supplied by the aforementioned branches of CN V (Goris et al., 1989; Kohl et al., 2014). In *Crotalus atrox* (western diamondback rattlesnake), the superficial branch of V_2 (V_2s) serves the ventral region of the pit membrane, the deep branch of V_2 (V_2d) serves the dorsal region, and the dorsotemporal region is served by V_1, generating some overlap between V_1 and V_2d (Kohl et al., 2014). These findings differ slightly from those of Goris et al. (1989), who found that V_1 innervates the dorsal membrane, while V_2d and V_2s innervate the rostral and ventral regions, respectively, in *Agkistrodon blomhoffi* (mamushi). Regardless, both studies describe a distinct partitioning of the pit membrane, with each partition innervated by a separate branch of CN V. This partitioning of the pit membrane and observed overlap of V_1 and V_2d is reflected in differential afferent terminations in the LTTD, resulting in a spatiotopic organization of signals generated in this first central processing center (Kohl et al., 2014).

In pythons, the rostral pits (which occur in the rostral scales) and the supralabial pits (which occur in the several supralabial scales caudal to the rostral scales) are collectively referred to as the "supralabial array". All pits in the supralabial array are innervated by both V_1 and V_2. In *Python reticulatus* (reticulated python), the two rostralmost pits are reportedly innervated by V_1 exclusively, the two adjacent pits by both V_1 and V_2, and the remainder by V_2 (de Cock Buning and Dullemeijer, 1977; Tan and Gopalakrishnakone, 1988). The infralabial pit arrays of pythons are innervated by the mandibular nerve (V_3) only (de Cock Buning and Dullemeijer, 1977; Tan and Gopalakrishnakone, 1988). No studies of boid pit innervation exist, though innervation in

boas is assumed to be the same as in the pythons, with the exception that boids have no pits in the rostral scale.

While broadscale patterns of pit organ innervation by CN V in one species of python are known, and the same patterns are assumed to exist both in all other pythons and in boas, no studies address the variation in patterns of innervation that may exist within and between these lineages. There is wide inter- and intrafamilial variation evident in the external morphology of the pit organs of boas and pythons (in both the number/size/shape/position and the locations of IR-sensitive tissues within the pits themselves; Maderson, 1970), which presumably constrains thermally-mediated behaviors and may influence thermoreceptive efficiency in a given environment. This appears to be reflected in the similarity of the independently evolved pit organs of boas, pythons, and pitvipers that occupy similar habitats. For example, arboreal species appear to possess larger pit organs and/or more extensive pit organ arrays than do terrestrial species, which increases their field of view and may make arboreal species more successful predators of birds and other tree-dwelling prey. I hypothesized that a similarly wide variation in the patterns and density of CN V innervation occurs in these two lineages. Here I expanded taxon sampling to include four python species (*Antaresia childreni*, *Morelia spilota*, *P. bivittatus*, *P. regius*) and two boas (*Corallus hortulanus*, *Boa constrictor*) (Fig. 3.1). I used diffusible iodine-based contrast-enhanced computed tomography (diceCT) to describe and compare the patterns of innervation of the pit organs and labial scales between species.

MATERIALS AND METHODS

Specimen Acquisition and Husbandry of Live Snakes

Live individuals of *C. hortulanus* (N=5), *B. constrictor* (N=3), and *P. regius* (N=5), were acquired from commercial breeders. *M. spilota* (N=2) were donated from a private collection, and live *A. childreni* (N=2) were donated from a breeding colony maintained by the DeNardo Lab at Arizona State University. Additional individuals of *A. childreni* (N=5) were euthanized by another lab group at USU and their heads were donated for use in this study. Previously culled individuals of *P. bivittatus* (N=5) were obtained from the Florida Fish and Wildlife Commission's Invasive Species Management program. They were captured in Florida between 2018 and 2020, euthanized in the field via boltgun (a standard practice in management of invasive species), and stored at -20°C prior to preparation for this study. A complete list of specimens used is provided in Table 3.1.

Live snakes were housed in the USU Biology Department vivarium, in individual enclosures, on newspaper substrate, and experienced a 12:12 light dark cycle, ambient temperature of 36°C, and 45% humidity. Snakes were fed a size-appropriate diet of mice or rats, and water was provided ad libitum.

Specimen Preparation

Live snakes were initially prepared according to the vascular casting methods described later in Chapter 4. Briefly, live individuals were deeply sedated via inhalation of isoflurane gas in a sealed glass chamber, and an incision was made along the ventral scales to expose the heart. After the heart was freed from the pericardium, a lethal dose of

sodium pentobarbital, mixed with a small quantity of heparinized physiological saline, was delivered via injection into apex of the ventricle. Following vascular flushing with additional saline, casting with Microfil, and curing of the casting medium (described in Chapter 4), snakes were injected with 10% phosophate buffered formalin (PBF; Appendix A) according to standard fixation techniques for museum specimens (Pisani, 1973), arranged in long loops, and fixed flat in trays filled with 10% PBF for at least ten days prior to use. Previously frozen, thawed *P. bivittatus* and freshly euthanized *A. childreni* were not perfused with Microfil, but were simply formalin-fixed as described for vascular cast specimens. Typically, preservation in 70% ethanol would follow formalin fixation, but instead the specimens were stored in 10% PBF to avoid excessive tissue shrinkage and potential degradation of the Microfil, as had been observed in other vascular cast specimens that have been stored in ethanol for long periods.

Prior to initial scanning (to resolve details of skeletal and vascular elements only; Chapter 4), the head and neck were removed from intact specimens immediately anterior to the heart to allow easier mounting during microCT scanning. Snake heads were placed in glass jars containing 1.25% Lugol's solution (Appendix C; Callahan et al., 2021), which reversibly binds to soft tissues, rendering them radio-opaque, and enabling x-ray radiographic detection. Jars were wrapped in aluminum foil to protect from light and placed on a shaker to ensure even staining. Complete penetration of stain was confirmed via quick scanning (~15min/scan) before longer scans were acquired. Most specimens were stained for only ~two weeks, though the largest species (*M. spilota*) required a staining duration of ~three months to achieve adequate penetration of stain.

MicroCT Scanning and Reconstruction of 3D Volumes

DiceCT scans were generated using a Nikon XT H 225 ST microCT scanner. The process of scan acquisition is depicted in Fig 3.2. Floral foam was used to stabilize specimens during scan acquisition. To do so, blocks of floral foam were carved into tubes, within which individual snake heads were placed, and the heads and foam were wrapped in plastic wrap to avoid tissue drying and shrinkage. Each wrapped specimen was mounted in a flat-bottomed glass cylinder to prevent movement during scan acquisition. Floral foam was used due to its relative radio-transparency compared to other stabilizing materials.

Individual specimens were placed on the stage inside the microCT chamber, and scans were acquired at 2s exposure, 18dB gain, and 4476 projections with a frame averaging of 1. Due to interspecific differences in relative size and density of specimens, scan parameters for voltage, current, power, and pixel spacing varied, and were optimized for each individual specimen (Table 3.2), to ensure that the highest resolution was achieved and that there was adequate contrast between material and background. Once projections were acquired, I used CT 3D Pro (Version 6.8.7977.22560; Nikon Metrology) to reconstruct volumes. I performed an automatic search for the dual centers of rotation and applied a beam-hardening correction of level 2 for all scans. Volumes were cropped to fit the specimen and reduce file size and were exported as both 16-bit VGL files and 16-bit TIFF stacks.

Analysis of 3D Volumes

Reconstructed volumes were imported into VG Studio Max (Version 3.5, Volume Graphics GnbH), grayscale values were calibrated for material and background, and these values were mapped to 10,000 and 50,000, respectively. I then used the Region Growing tool, with tolerance adjusted as needed, to generate regions of interest for CN V_1-V_3, the trigeminal ganglion, the supra- and infralabial scale rows, and the pit arrays, for examination of intra- and interspecific patterns of innervation to the labial scales and pit organs.

RESULTS

Variation in Pits and Pit Arrays

Boa constrictor

As previously noted, *Boa constrictor* entirely lacks macroscopic evidence of true pit organs between either the supra- or infralabial scales. However, I did observe small depressions on the caudal edges of infralabial scales 2-15 and supralabial scales 10-14 (Fig. 3.3). These depressions were vaguely circular, and were only visible under microCT examination.

Corallus hortulanus

Unlike *B. constrictor*, *Corallus hortulanus* does possess obvious pit organs in both supralabial and infralabial arrays. While the supralabial array in pythons is present in the rostral and anterior regions of the face, the supralabial array in *C. hortulanus* involves only the more caudal supralabial scales (supralabial scales 6-11). The

caudalmost extent of this array falls at the rictus oris, and its most anterial extent occurs

ventral to the anterior edge of the orbit. As described in previous studies, these pit organs

do not form within the scales, but rather are formed from the depressed rostral and caudal

margins of adjacent scales (Bullock and Barrett, 1968; Ebert,2008) that meet to form a V-

shaped space. For pits 3-5 (counting from the front of the array), the top and bottom of

the inter-scale space is enclosed by the dorsal and ventral edges of the scales, which curl

down or up to surround them (Fig. 3.4). In doing so, the curled scale edges effectively

form an aperture. The largest and deepest supralabial pits are pits 4 and 5. In the

infralabial array, the ventral margin of the pitted scales is folded over, but the dorsal

margin is not. Instead, when the mouth is closed, the ventral edge of the supralabial

scales form the dorsal border of the infralabial pit aperture. The largest and deepest pits in

this array and the overall number of pits mirrored those in the supralabial array in all

individuals examined.

Morelia spilota

Morelia spilota possesses rostral pit organs, anterior supralabial pit organs, and a

well-developed infralabial pit array. The rostral pit organs occur as a single pair of

crescent-shaped invaginations on either side of the midline in the superior halves of the

rostral scale (Fig.3.5). The three pits of the supralabial array appear as inverted-teardrop-

shaped depressions in the superior, caudal corners of supralabial scales 1-3 (Fig.3.5).

Both the relative size of the aperture and the depth of the supralabial pit organs decrease

from rostral to caudal, with supralabial pit 1 being the largest and deepest in the anterior

array. There are eight pits in the infralabial array, occurring from infralabial scale 6 to

scale 13. Pit 8 is angled with the aperture facing nearly fully dorsad, but a gradual

inferiolateral tilt from caudal to rostral shifts each preceding pit accordingly, such that the fundi of the rostralmost pits in this array face outward. The pit fundus is broad and curved, having a cup-like shape, thickly enfolded by the dorsal and ventral edges of each scale, which lend the pit apertures a square appearance externally. There is a rostral to caudal increase in size from infralabial pit 1 to pit 6, with pit 6 being the largest in this array in terms of both aperture and depth. There is then a rapid decrease in size from pit 6 to pit 8. Interestingly, while other IR-imaging taxa appear to have pit organs that are pink in color (due to lack of pigmentation in the fundus and dense blood supply to the heat-sensitive tissues), the pit fundi in both the supra- and infralabial arrays of *M. spilota* are black, reflecting the dense pigmentation of these tissues (Fig 3.6).

Antaresia childreni

The supralabial pits were absent in all *A. childreni* examined, though the infralabial pit array in this species is well-developed and involves infralabial scales 9-11 (Fig 3.7). There is apparent variation in the rostralmost extent of this array, with some individuals having shallow depressions in infralabial scales 7 and 8 (Fig 3.7). However, only the four pits occupying scales 9-11 were well-developed, and these were consistent between individuals. Each infralabial pit organ is shifted toward the caudalmost edge of the scale it occupies, with the larger pits involving more of the scale's surface. At first glance, it appears that there is a caudal-to-rostral decrease in pit size, but closer examination shows that the relative size of both the aperture and depth are greater for the third pit of this array. The pit fundus is relatively narrow and vertically elongate, bordered rostrally and caudally by the slightly angled walls of the pit cavity. This gives each pit a cone-like shape.

Python regius

      Python regius possesses well-developed rostral and anterior supralabial pit organs

(Fig 3.8). As in both *M. spilota* and *P. bivittatus*, the pit organs of the anterior upper jaw

are shaped like inverted tear drops. However, the tops of these tear drops are expanded,

giving the impression of a nearly circular aperture. Rather than forming within the rostral

and supralabial scales, the pits in this array appear to involve two or more adjacent scales.

The rostral pit occurs dorsal to the lateral angle of the rostral scale, and is bracketed on its

dorsal and lateral borders by a narrow, r-shaped scale. Supralabial pit 1 occurs in the

dorsolateral angle of the first supralabial scale. It is bordered dorsally by the nasal scale,

and laterally by a narrow, v-shaped scale (Fig. 3.8). Supralabial pits 2-4 also form in the

dorsolateral angle of their respective supralabial scales, and are bordered laterally by

narrow, v-shaped scales. Dorsally each of these pits is bordered by two separate scales.

Supralabial pit 2 is bordered by the nasal and the first postnasal, whereas pit 3 is bordered

by the first and second postnasal scales and pit and 4 by the second and third postnasal

scale. Some individuals possess a fifth supralabial pit (Fig. 3.8). When present, this pit is

much smaller, shallower, and narrower than the other pit organs in the supralabial array. It

is also the only supralabial pit that appears to form entirely within its supralabial scale.

The rostral and first supralabial pit face forward, while pits 3-5 point laterally. The largest

and deepest of the supralabial pits is pit 2, which occupies a region in the curve of the

rostrum, and thus a portion of its fundus faces forward, while the remainder faces

laterally.

      The infralabial array is present in *P. regius*, though it consists of only three to four

small, shallow, rounded depressions in the ventrocaudal corners of scales 8-11 (Fig 3.8).

Pits 2 and 3 in this array are the largest and deepest, relatively speaking, and are consistently present between individuals. Pits 1 and 4 vary in occurrence and shape, sometimes appearing as circular pits (like the others in the array) and sometimes only as a vague, medial, inward folding of the scales involved (Fig. 3.8).

Python bivittatus

The rostral and supralabial pit organs of *Python bivittatus* are similar in shape and position to those of *M. spilota*, though the morphology of the scales that border them is more similar to that of *P. regius* (Fig. 3.9). Despite these similarities, the pits in this array appear much narrower than in either *M. spilota* or *P. regius*, and there are only two supralabial pits. The infralabial pits are similar to those of *P. regius*, in that they exist as shallow depressions (Fig.3.9). In all individuals, this array implicates only infralabial scales 10-12. The shape of these pits varies between individuals, appearing as either regular, vaguely ovoid depressions in the caudal half of the scales involved, or as an inward folding across all or part of middle of the scale.

Innervation of the Pit Arrays and Labial Scales

As previously described, the major cranial nerve serving the supra- and infralabial scales and/or pit organs is the trigeminal nerve, CN V. In all taxa examined V_1 innervates the rostral scale or pits, the superficial and deep branches of V_2 innervate the supralabial scales/pit array, and V_3 innervates the infralabial array. The greatest variation is evident in the innervation involving the maxillary nerve (Fig 3.10) Even in the absence of supralabial pit organs (as in *A. childreni*), the maxillary nerve exhibits some degree of sub-branching. Less variation is observed in the mandibular nerve (Fig 3.10), although

species with well-developed infralabial pit arrays exhibit more extensive sub-branching of V_3 and a relatively higher density of nerve fibers to the pit organs. There is both inter- and intrafamilial variation in innervation of the pit organs by CN V, which is described in detail below.

Boidae

The ophthalmic branch of CN V contacts the peripheral tissues of the rostral scale in both of the boid species examined, but, in the absence of rostral pit organs in boids, it does not exhibit any notable branching as it extends anteriorly (Fig 3.11,3.12). In *C. hortulanus,* the maxillary nerve divides into the superficial and deep branches, the latter of which subdivides into two primary branches (Fig 3.11). Supralabial scales 3-7 are served by V_{2D}, which further subdivides, sending three of those divisions to scales 3-5, and three to scales 5-7. Scale 5, therefore, receives innervation from two separate sub-branches. The superficial branch of CN V sub-branches to innervate the caudal supralabial pit array in *C. hortulanus*. Pits 1-3 receive fibers from $V_{2S}a$ only, and pit 5 is also only innervated by $V_{2S}d$. The rostral- and caudal edges of the scales that form pit 4 are innervated by $V_{2S}b$ and $V_{2S}c$, respectively. The caudal infralabial pit array of *C. hortulanus* is densely innervated by the mandibular nerve, which divides into five sub-branches at the level of the pit array (Fig 3.11). The rostral and caudal edges of the adjacent scales that are depressed to form the pits of the infralabial array receive innervation from either one branch or from separate sub-branches, as follows: V_3a innervates the entirety of pit 1 and the rostral edge of pit 2; V_3b innervates the caudal edge of pit 2 and the rostral edge of pit 3; V_3c innervates the caudal edge of pit 3 and the

rostral edge of pit 4; V_3d innervates the caudal edge of pit 4 and the rostral edge of pit 5; and V_3e innervates the caudal edge of pit 5 and the entirety of pit 6.

While *B. constrictor* lacks obvious pit organs, both the maxillary and mandibular nerves divide extensively to contact the regions of the supra- and infralabial scale rows, respectively (Fig 3.12). These regions of the scales are reportedly sensitive to infrared stimulation (Bullock and Barrett, 1968). In *B. constrictor*, the maxillary nerve has three primary branches, which subdivide as they extend toward the peripheral tissues, generating three distinct regions of innervation. Scales 1-7 are served by V_{2D}, 8-16 by V_2sa, and 17-21 by V_2sb. Four slender, forked fibers extend from V_{2D}, with scales 1-3, 3-4, 4-5, and 6-7 receiving innervation from each of the four fibers, respectively. Five fibers from V_2sa innervate scales 8-9, 8-11, 12-14, 15, and 16, with scales 8-11 sharing innervation by two of these fibers. The caudalmost sub-branch, V_2sb, projects fibers that innervate scale 17, scales 18-19, and scales 20-21, with no scales in this series innervated by more than one nerve fiber. The mandibular nerve of *B. constrictor* has two sub-branches, V_3a and V_3b (Fig 3.12). Similar to the maxillary nerve, V_3a projects four delicately forked fibers to innervate the anterior-most infralabial scales, with individual fibers supplying scales 1-4, 4-5, 6-7, and 7-8. The innervation of the caudal infralabial scales by V_3b is more reminiscent of the innervation of the region in the other species examined, in being more dense and projecting many smaller nerve fibers. V_3b has two distinct divisions, with the more anterior division serving scales 11-17, and the posterior division serving scales 18-21.

Pythonidae

In *Antaresia childreni*, the ophthalmic nerve contacts the rostral scale, and the

maxillary nerve branches extensively to contact the supralabial scales (Fig 3.13).

However, although the maxillary nerve exhibits extensive branching, most of the

supralabial scales are innervated by only a single sub-branch, rather than the dense

terminal arborizations found in the other two pythonids examined here. The exception is

the second supralabial scale, which is innervated by two sub-branches of V_{2D}. Innervation

of the infralabial pit array by the mandibular nerve is much more robust, with five sub-

branches serving this array (Fig 3.13). Pits 1-2 in the infralabial array are served by V_3a

only, whereas pit 4 receives innervation exclusively from V_3d. The deepest pit organ in

the infralabial array, pit 3, receives innervation from both V_3b and V_3c. These two sub-

branches supply the rostral and caudal halves of the pit fundus, respectively.

The rostral pit of *Morelia spilota* on each side is exclusively innervated by the

ophthalmic nerve (Fig 3.14). As in other taxa examined, V_{2D} supplies the majority of the

anterior supralabial scales, but in *M. spilota* that branch does not exhibit any sub-

branching (Fig 3.14). Instead, pits 2 and 3 of the supralabial array are both densely

innervated by V_{2D}, and pit 4 (the smallest and most shallow pit in the array) is innervated

by V_{2S}. The pit organs of the caudal infralabial array are larger and deeper than those of

the other taxa examined and are served by five sub-branches of the mandibular nerve (Fig

3.14), in a pattern similar to that of *A. childreni*. Pits 1-3 are served by V_3a only, pit 4 by

V_3b only, and pits 6-7 by V_3e only. Pit 5, however, is innervated by both V_3c and V_3d.

Of the taxa examined, the rostral and supralabial pits of *P. regius* are the largest and the

supralabial array is the most extensive. As in *M. spilota*, the rostral pit on each site is

exclusively innervated by ophthalmic nerve, though the nerve fibers contacting the pit are much more dense (Fig 3.15). The deep branch of the maxillary nerve serving this array divides into six sub-branches (Fig 3.15). Pit 2 is served by $V_{2D}a$, pit 3 by $V_{2D}a$-$V_{2D}d$, pit 4 by $V_{2D}d$ and $V_{2D}e$, pit 5 by $V_{2D}f$ and V_{2S}, and pit 6 by V_{2S}. Pit organs in the infralabial array are much smaller and shallower than in either *M. spilota* or *A. childreni* and receive only weak innervation from V_3.

In *P. bivittatus* the rostral pit organ on each side is innervated by V_1, and the three supralabial pits by V_{2D}, which subdivides to supply each of these pits with its own nervous supply (Fig. 3.16). The infralabial pits are much less highly structured, presenting less as individual pit organs and more as a horizontal groove across the three scales involved. Each of these weakly defined pits receives its own subbranch of V_3, though innervation of this array is similarly as weak as in *P. regius*.

DISCUSSION

It is well known that the pit organ arrays in all IR-imaging taxa are innervated by one or more major rami of the trigeminal nerve. Previous studies in pythons and boas have utilized gross dissection to examine innervation of the pit arrays of the upper and lower jaws, establishing that the rostral pits are generally innervated by V_1, the supralabials by V_2, and the infralabials by V_3 (Lynn, 1931). Despite the observation that pythons and boas possess multiple pit organs organized in arrays along the upper and lower jaws, and that the morphology of these arrays varies substantially among taxa, no previous studies have described a similar level of variability among the sub-branches of the trigeminal rami. Horseradish peroxidase tracing studies in *Malayopython reticulatus* have confirmed that pits of the upper jaw receive afferent innervation from V_1 (rostral

and first supralabial) and V_2 (all supralabials), and infralabial pits from V_3 (Tan &

Gopalakrishnakone, 1988). In such studies, HRP was applied to individual pit organs in

each array and traced to the trigeminal ganglion. However, placement of the tracer into a

given pit was much too general to permit the detection of the extensive sub-branching I

have observed in both V_2 and V_3.

In the three species of pythons I examined that possess rostral pit organs, these

pits are served exclusively by V_1. This result in *Morelia spilota* differs from a previous

report by Warren and Proske (1968), who asserted that all pits in the supralabial array of

this species (to include the rostral pit) are innervated by V_2, with no involvement from

V_1. However, diceCT allowed for in situ observation and tracing of the nerve branches

innervating each of the pits in the supralabial array, and the nerve that innervates the

rostral pit in *M. spilota*, *P. bivvittatus*, and *P. regius* unquestionably arises from the

ophthalmic ganglion (thus it is definitely V_1). The density of peripheral nerve fibers in V_1

appears to correlate with the size and depth of these rostral pit organs. V_1 extends forward

from the ophthalmic ganglion to innervate the rostral scale of all taxa examined, though

species that lack rostral pits are less extensively and densely innervated by this trigeminal

ramus.

The deep branch of V_2 exhibits the greatest interspecific variation. The superficial

branch of V_2 in three of the pythons examined (*M. spilota*, *P. regius*, *P. bivittatus*) did not

exhibit any sub-branching, whereas it was split into two subbranches in the fourth species

(*A. childreni*). This was not the case for either of the two boas examined. In *C.*

hortulanus, the caudal supralabial array was densely innervated by four sub-branches of

V_{2S}. Despite possessing only shallow pits, the superficial ramus of V_2 in *B. constrictor*

still exhibits extensive sub-branching to innervate the labial scales in this region. Although the innervation is much less dense than that observed in *C. hortulanus*, the general pattern of sub-branching and the regions innervated are consistent between both boid species.

Both the innervation of the caudal infralabial scales and the fanlike projection of V_3 following its exit from the mandibular foramen of the compound bone are evolutionarily conserved. Although this general pattern of innervation is not unique to the IR-imaging snakes, the extensive sub-branching and increased density of nerve fibers when infralabial pits are present is noteworthy.

Anterograde tracing has demonstrated that pitviper pits are simultaneously innervated by V_1 and both the superficial and deep branches of V_2 (Goris et al., 1989; Kohl et al., 2014). Thus, the pit membrane in pitvipers pits is partitioned into three distinct sensory regions by the V_1, V_{2S}, and V_{2D}. When traced from the pit to the LTTD, these spatial relationships are preserved. No pit organs in the pythons and boas I examined are innervated by two separate trigeminal rami, although some pit organs in these taxa do receive innervation from two or more sub-branches of a given ramus. For example, supralabial pit 2 in *P. regius* is positioned at the curve of the rostrum, and its innervation by four distinct subbranches of V_{2S} partitions the fundus into four distinct regions. Thus, position of an IR stimulus relative to such pit organs presumably stimulates a given region or regions, with information transmitted via specific subbranches. This suggests that innervation of a single pit organ by multiple subbranches of a given nerve imparts a greater degree of directional sensitivity, as information transmitted via separate sub-branches may be similarly spatiotopically mapped in the

optic tectum. The locations of the pits that receive multiple sub-branches may, therefore, be quite critical for IR imaging.

TABLES AND FIGURES

Table 3.1. Specimens examined for diceCT examination of the pit organs and trigeminal nerve.

Family	Taxon	Specimen ID #
Pythonidae	*A. childreni*	HBP-013
		HBP-014
		F15
		F29
		F59
		M30
	M. spilota	HBP-015
		HBP-016
	P. bivittatus	PyBi-056
		PyBi-089
		PyBi-315
		AHS L-10091
	P. regius	HBP-044
		HBP-045
		HBP-046
		HBP-047
		HBP-048
Boidae	*B. constrictor*	HBP-023
		HBP-024
		HBP-025
	C. hortulanus	HBP-018
		HBP-019
		HBP-020
		HBP-021
		HBP-030
		HBP-040

Table 3.2. DiceCT scan parameters for each specimen examined.

Specimen ID #	Beam Energy (kV)	Beam Current (µA)	Pixel Spacing (µm)	Exposure (ms)	Gain (dB)
HBP-013	95	100	14	1000	24
HBP-014	95	205	14	1000	18
F15	83	120	12	1000	18
F29	85	118	13	1000	18
F59	85	118	12	1000	18
M30	85	118	13	1000	18
HBP-015	90	215	27	1000	18
HBP-016	120	210	26	1415	12
PyBi-056	100	180	19	1000	18
PyBi-089	95	211	29	2000	12
PyBi-315	95	189	19	1000	18
AHS L-10091	95	211	28	2000	12
HBP-044	90	210	15	1000	18
HBP-045	90	210	15	1000	18
HBP-046	95	200	19	1000	18
HBP-047	85	118	13	2000	18
HBP-048	87	115	13	2000	18
HBP-023	95	100	12	1000	24
HBP-024	95	100	14	1000	24
HBP-025	95	100	11	1000	24
HBP-018	80	200	16	250	18
HBP-019	80	200	17	250	18
HBP-020	85	200	18	250	18
HBP-021	75	165	14	1000	24
HBP-030	80	135	15	1000	24
HBP-040	80	135	15	1000	24
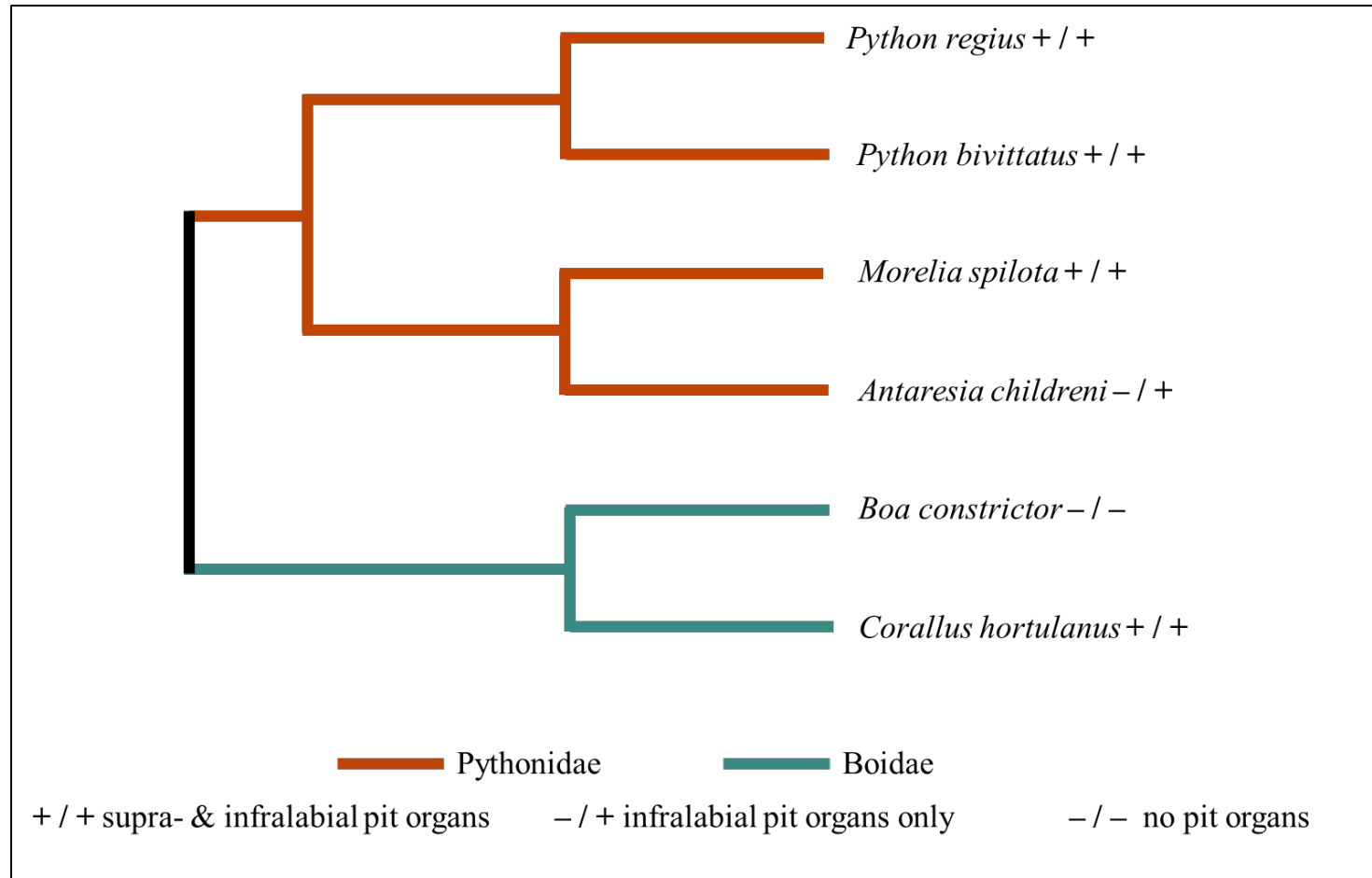
Fig. 3.1. Cladogram based on Reynolds et al. (2013), showing the relationships between the species of boas and pythons examined. Plus (+) and minus (–) symbols indicate presence or absence of pit organs in (Pythonidae) or between (Boidae) the supra- and/or infralabial scales
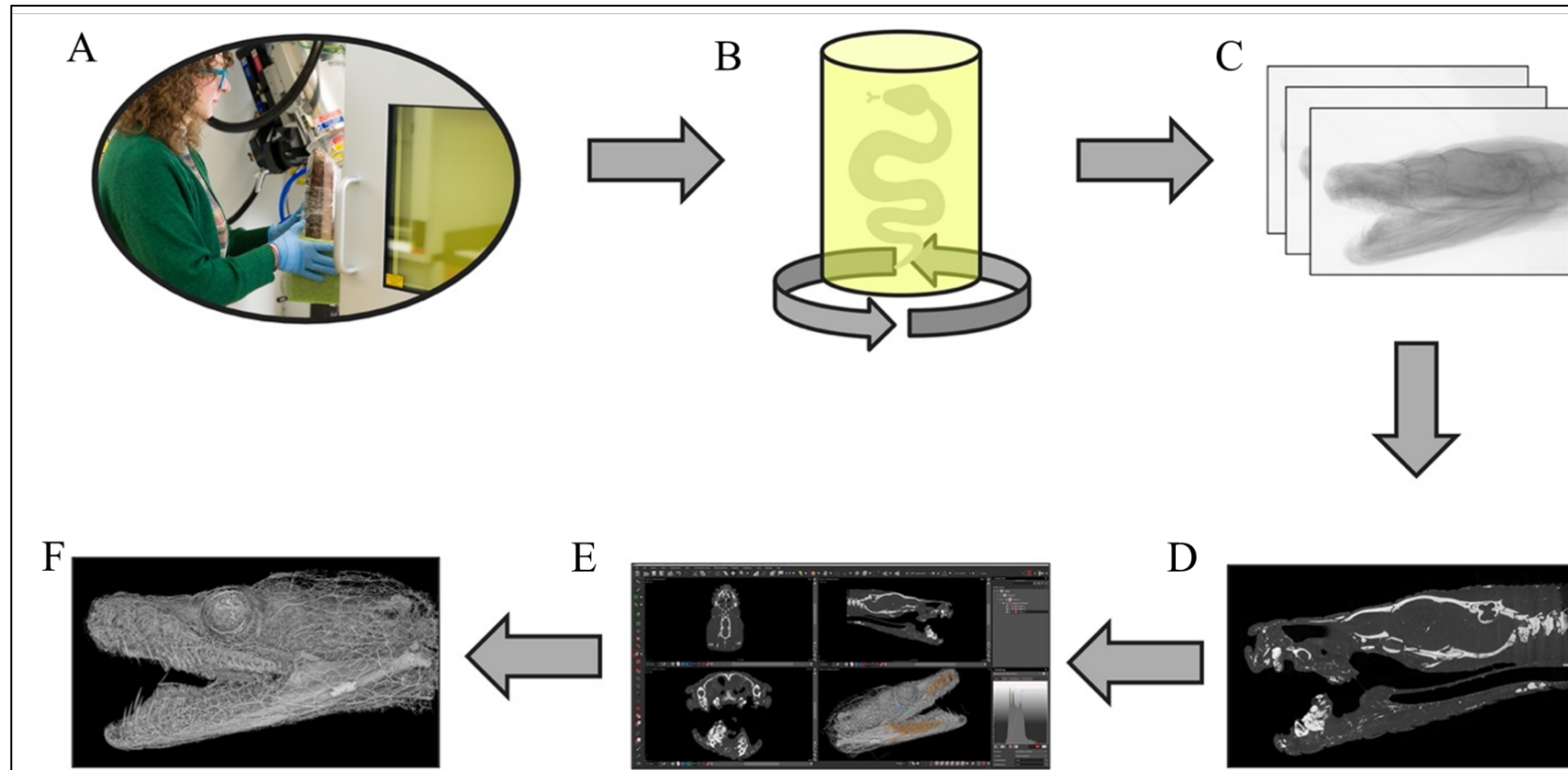
Fig. 3.2. Diagram depicting the steps of microCT scan acquisition and analysis: (A) loading specimen into the instrument chamber; (B) scanning of specimen as it rotates 360°; (C) acquisition of 2D radiographic projections; (D) reconstruction of 2D radiographs into 3D volume; (E) use of software (VG StudioMAX) to segment regions of interest (ROIs) from the 3D volume; (F) generation of a 3D rendering of segmented ROIs.
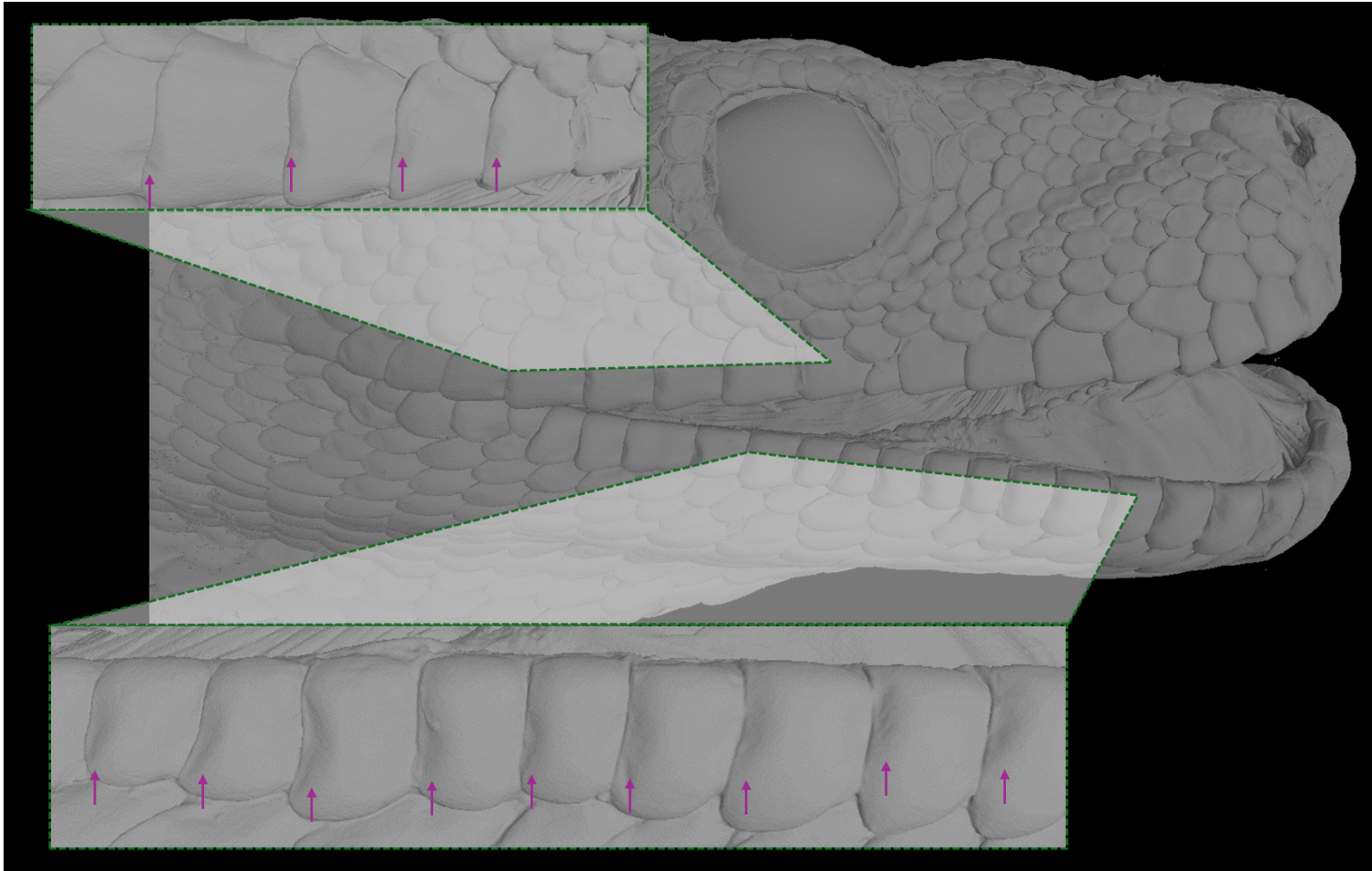
Fig. 3.3. The labial scales of *Boa constrictor* possess depressions on their caudal margins (depressions indicated by purple arrows)
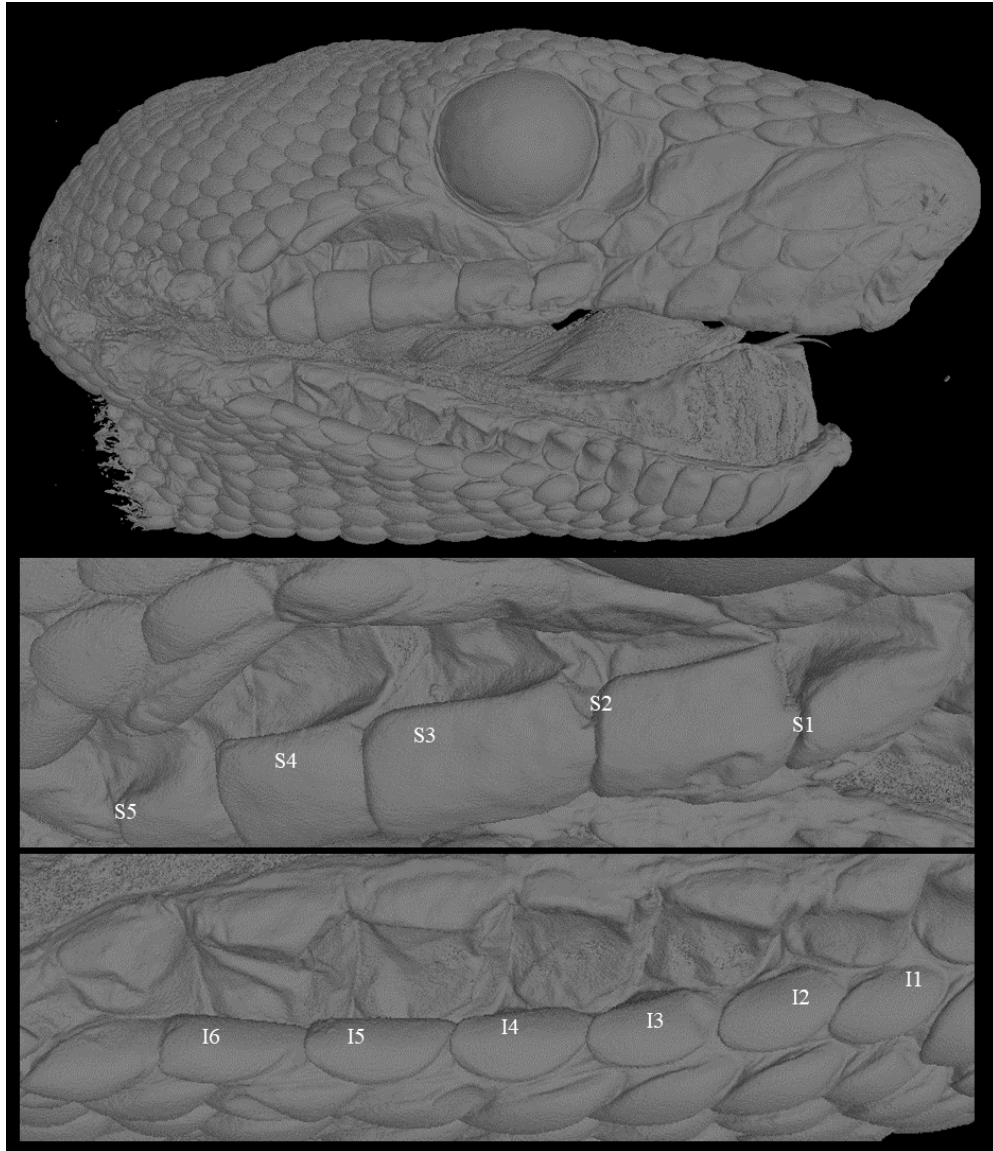
Fig. 3.4. The pit arrays in *Corallus hortulanus* are located on the caudal supralabial and caudal infralabial scales. There are five pits present in the supralabial array (S-1 through S-5), between supralabial scales 6-11, and six pits present in the infralabial array (I-1 through I-6) between infralabial scales 10-16.
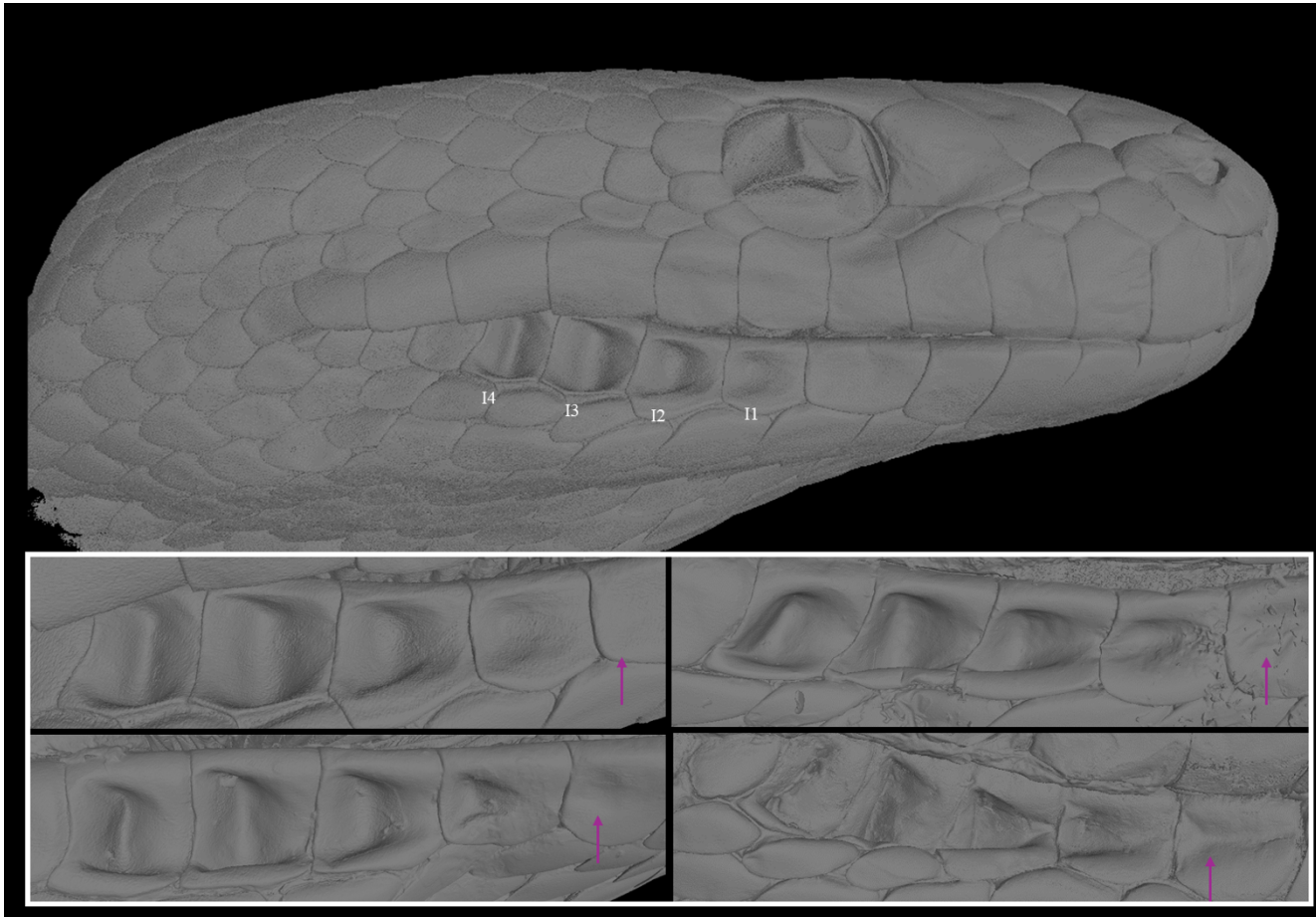
Fig. 3.6. *Antaresia childreni*, lacks supralabial pit organs, but it has a well-developed infralabial array (I-1 through I-4 in this individual). This array always includes at least four pit organs, though there is some individual variation (shown in the four bottom panels). There are consistently at least four pit organs located within infralabial scales 8-11, but some individuals also possess an additional, shallow pit organ within scale 7 (indicated by purple arrows)
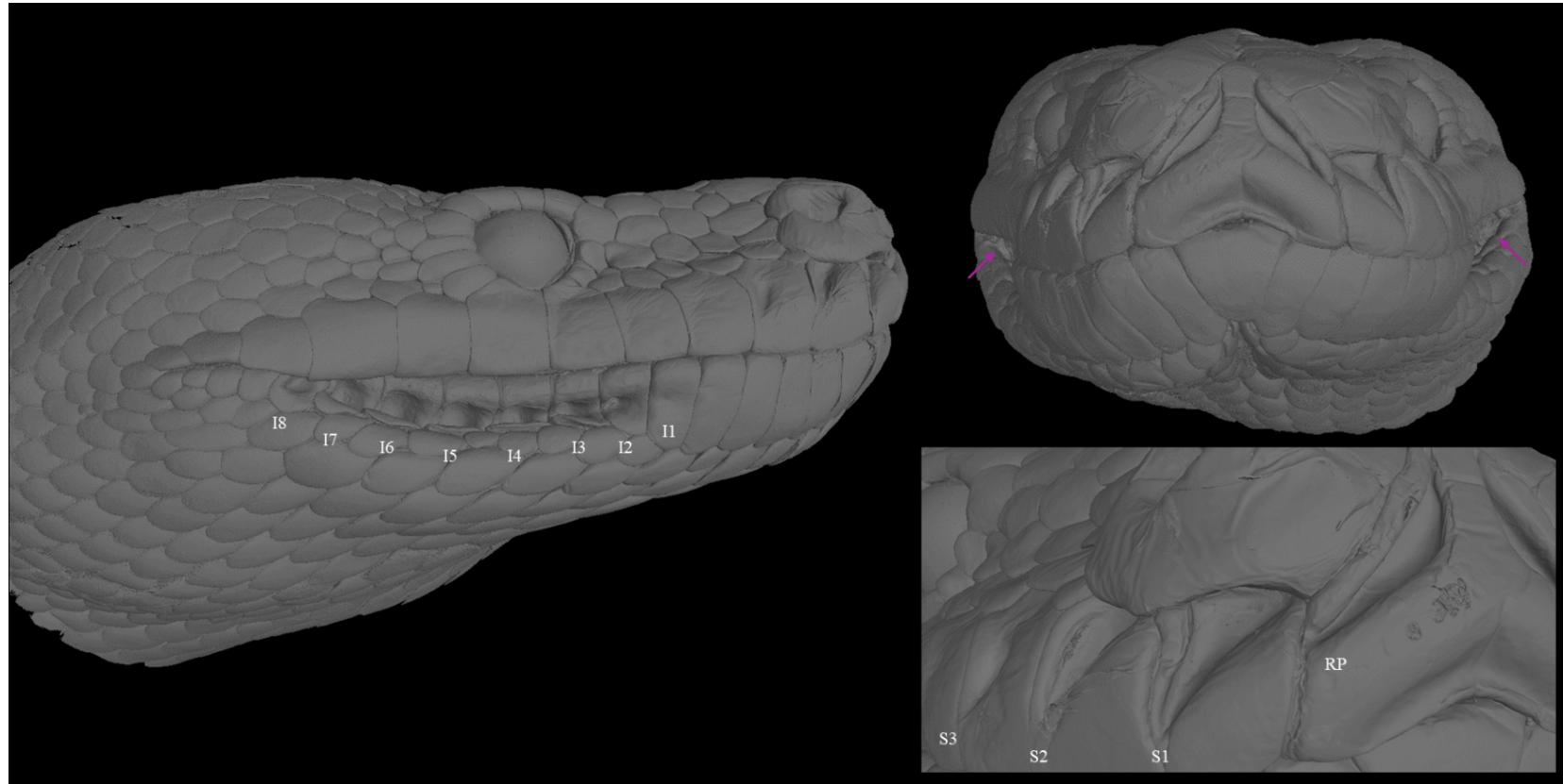
Fig. 3.6. *Morelia spilota* possesses a rostral pit organ (RP) and three supralabial pit organs (S-1 through S-3) in the supralabial array, and eight pits in the infralabial array (I-1 through I-8). The deepest pits in the infralabial array (I-5 and I-6, marked with red   arrows) are tilted to receive stimulation from infrared stimuli positioned in front of the face.
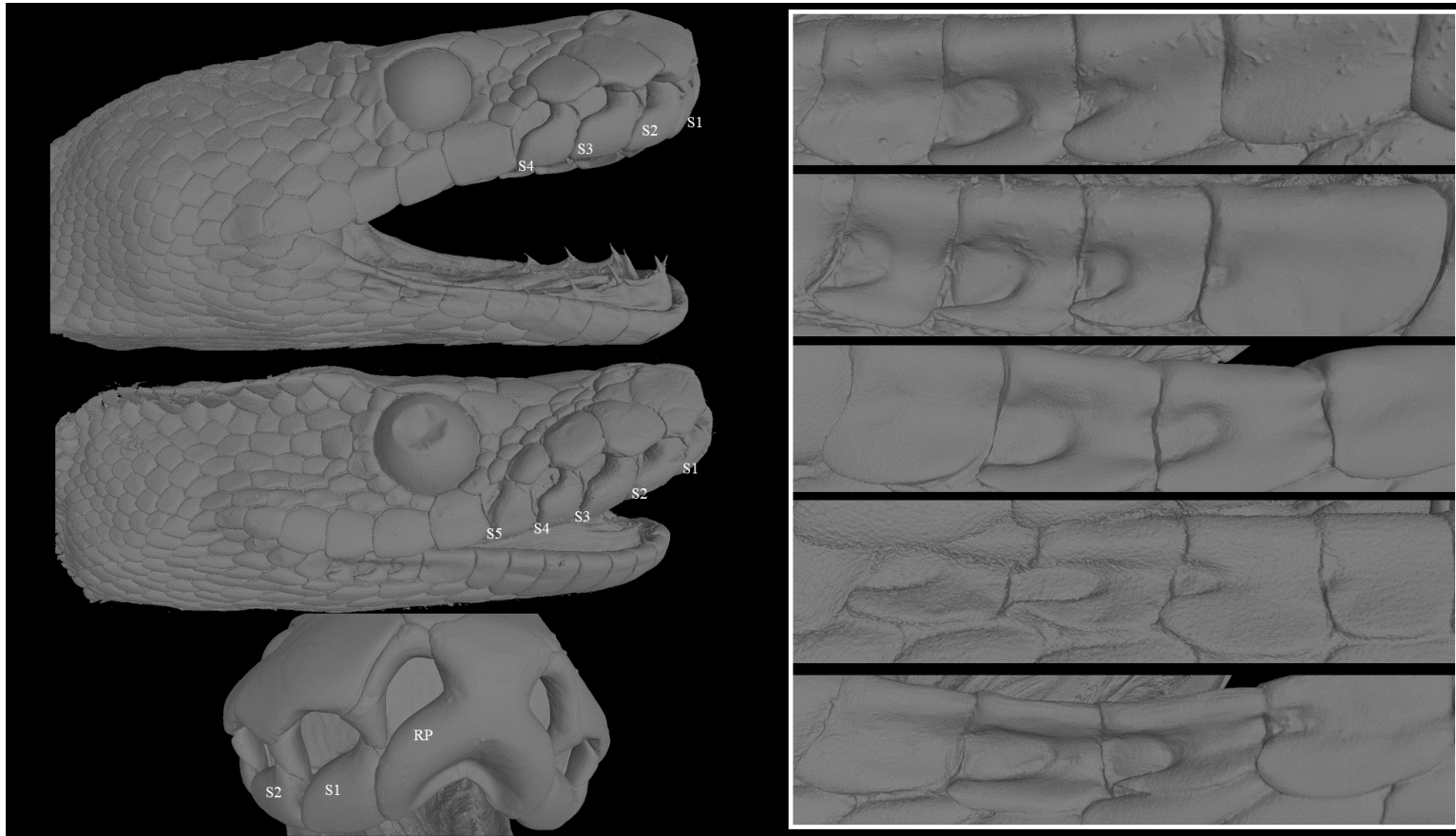
Fig. 3.7. Intraspecific variation in the number of pits in the supra- and infralabial arrays of *Python regius.* In the supralabial array, the rostral pit (RP) is consistently present, and there are at least 4 supralabial pits (S-1 through S-4) located in supralabial scales 1-4. Some individuals possess an additional pit (S-5) in supralabial scale 5. The number of pit organs in the infralabial array also varies (shown in the five panels at the right). The two deepest infralabial pits are consistently present and are located in infralabial scales 9 and 10. Additional pits are sometimes present in infralabial scales 8 and 11 (indicated by red arrows).
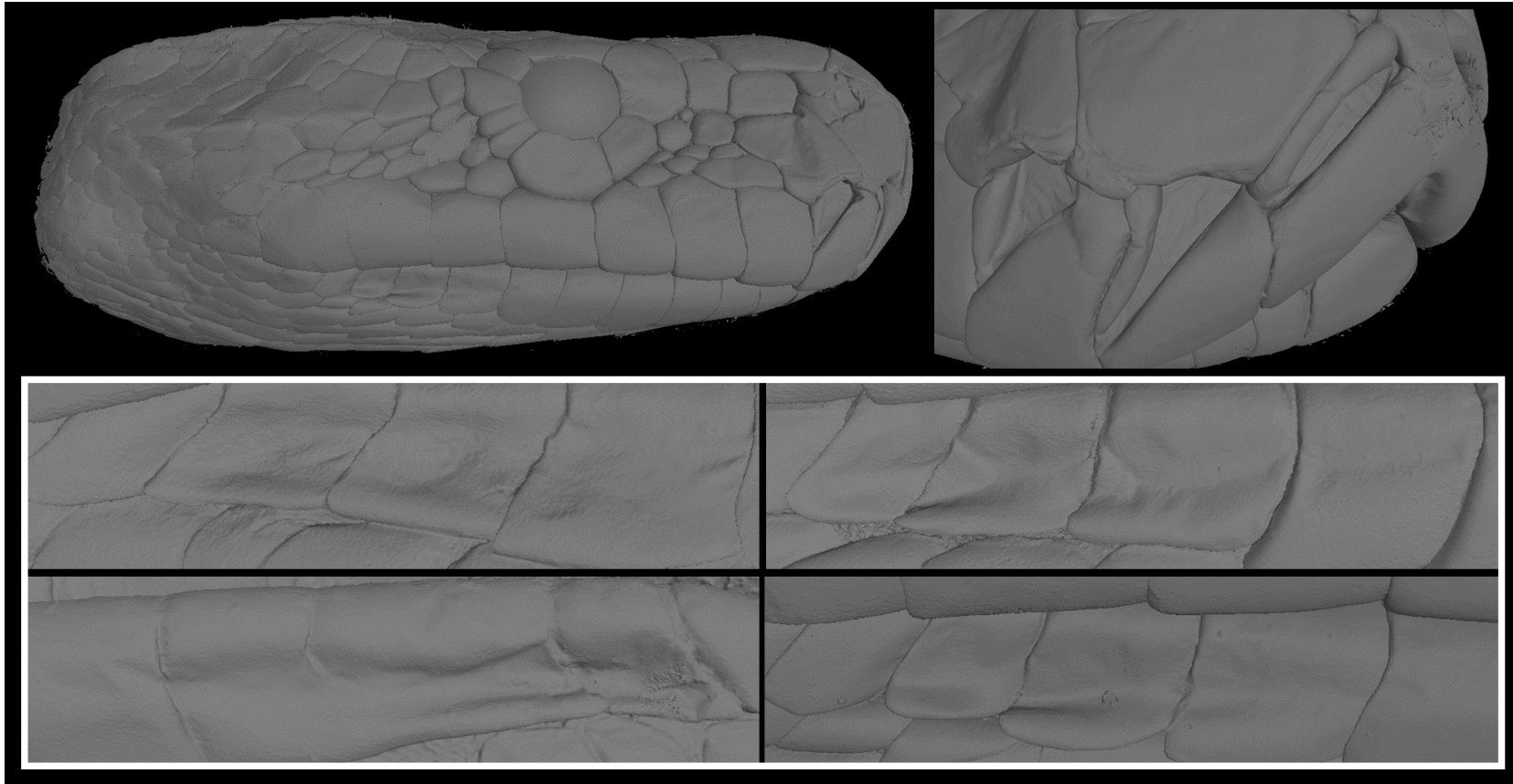
Fig. 3.8. *Python bivittatus* possesses three pit organs in its supralabial array, including the rostral pit (RP) and two supralabial pits (S-1 and S-2). The number of pits in the infralabial array exhibits substantial intraspecific variation (shown in the four bottom panels*).
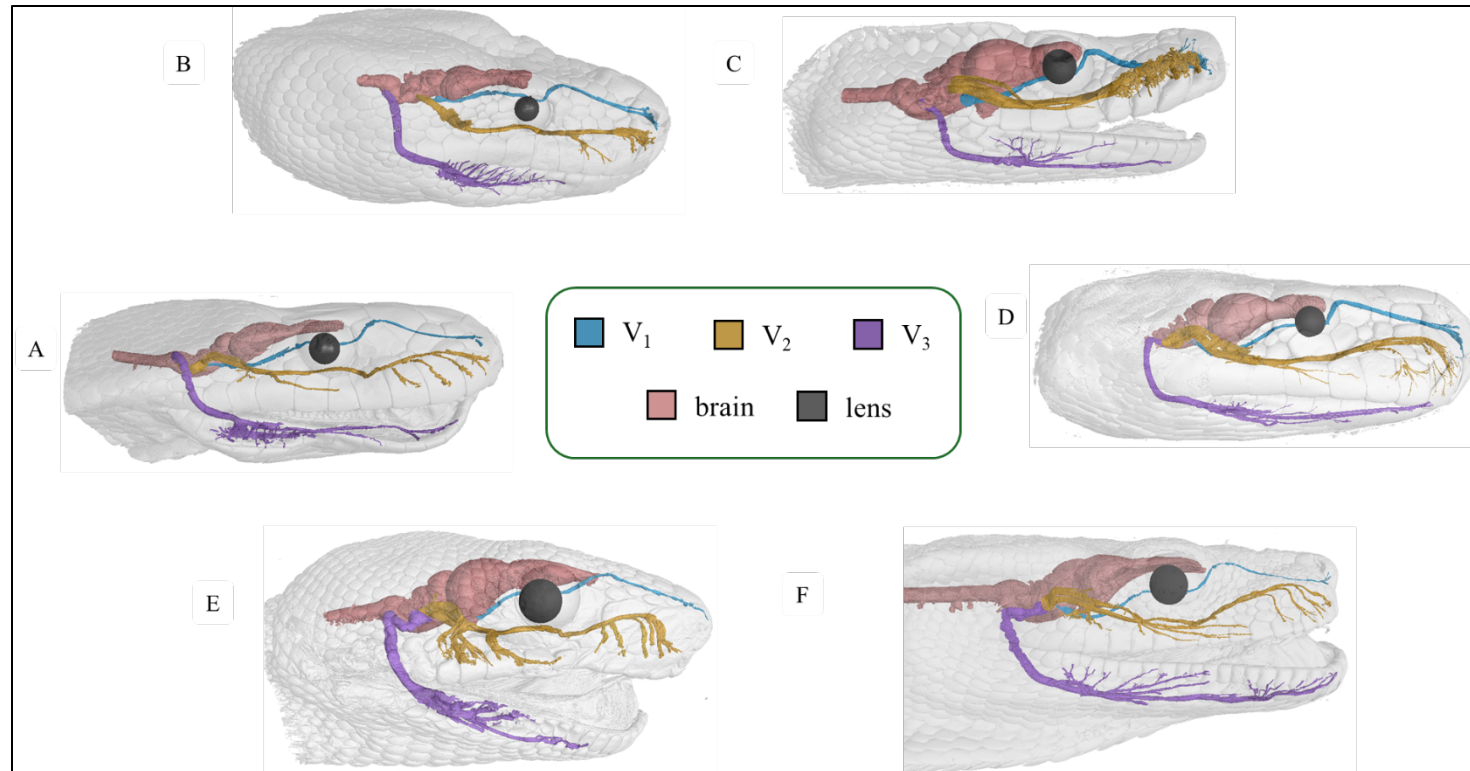
Fig. 3.9. There is substantial variation in the trigeminal nerve between the species examined, particularly in the morphology of the maxillary nerve, which is heavily modified where it innervates the supralabial pit arrays. The ophthalmic branch (V_1) innervates the rostrum, and in pythons with rostral pits (B, C, D) it sends several sub-branches to the rostral pits. Branching of the mandibular branch (V_3) serving the caudal infralabial region is consistent between taxa, with a denser distribution of sub-branches correlating with deeper and more numerous pits in the infralabial array. (A, *Antaresia childreni*; B, *Morelia spilota*; C, *Python regius*; D, *P. bivittatus*; E, *Corallus hortulanus*; and E, *Boa constrictor*. V_1 is blue, V_2 is orange, V_3 is purple. The lens of the eye [black] and brain [pink] are included, to indicate the relative positions of the nerves)
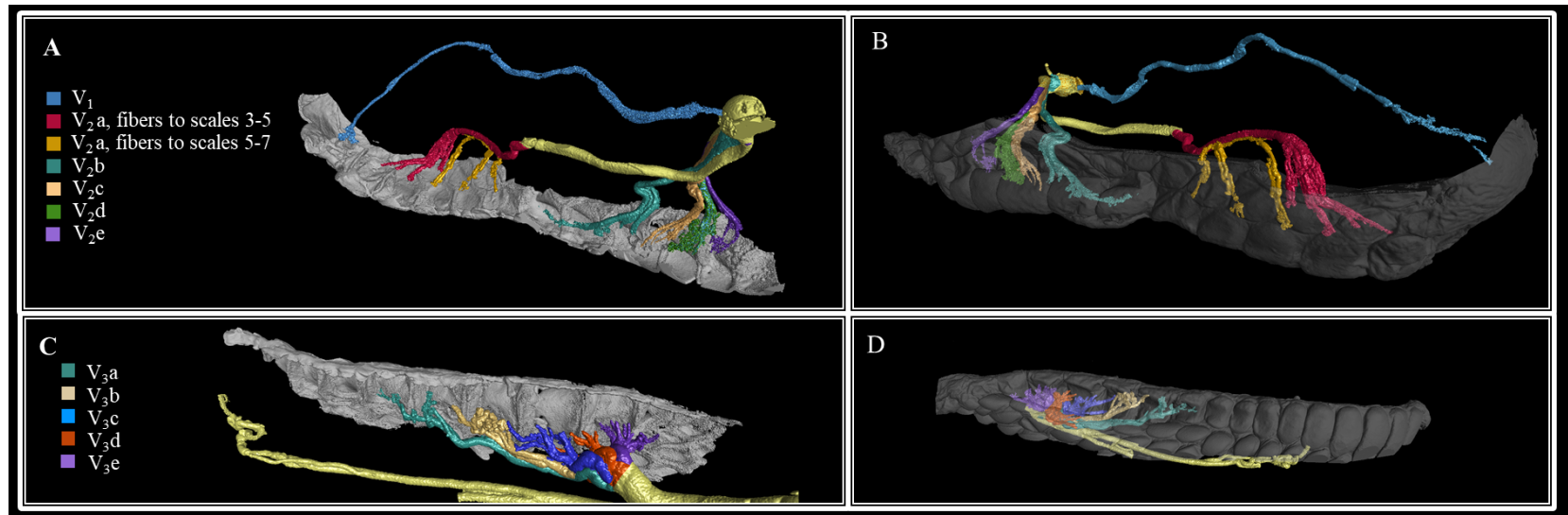
Fig. 3.10. Innervation of the supralabial (A,B) and infralabial (C,D) scales in *Corallus hortulanus*. Pit 4 in the supralabial array of receives innervation from two sub-branches of the superficial branch of the maxillary nerve (V$_2$S). Pits 4 and 5 in the infralabial array each receive innervation fromtwo2 sub-branches of the mandibular nerve (V$_3$). The relationship between the nerves and the scales or pits they innervate is shown in internal view (A, C) and external view (B, D). Inset identifies the colors assigned to individual sub-branches.
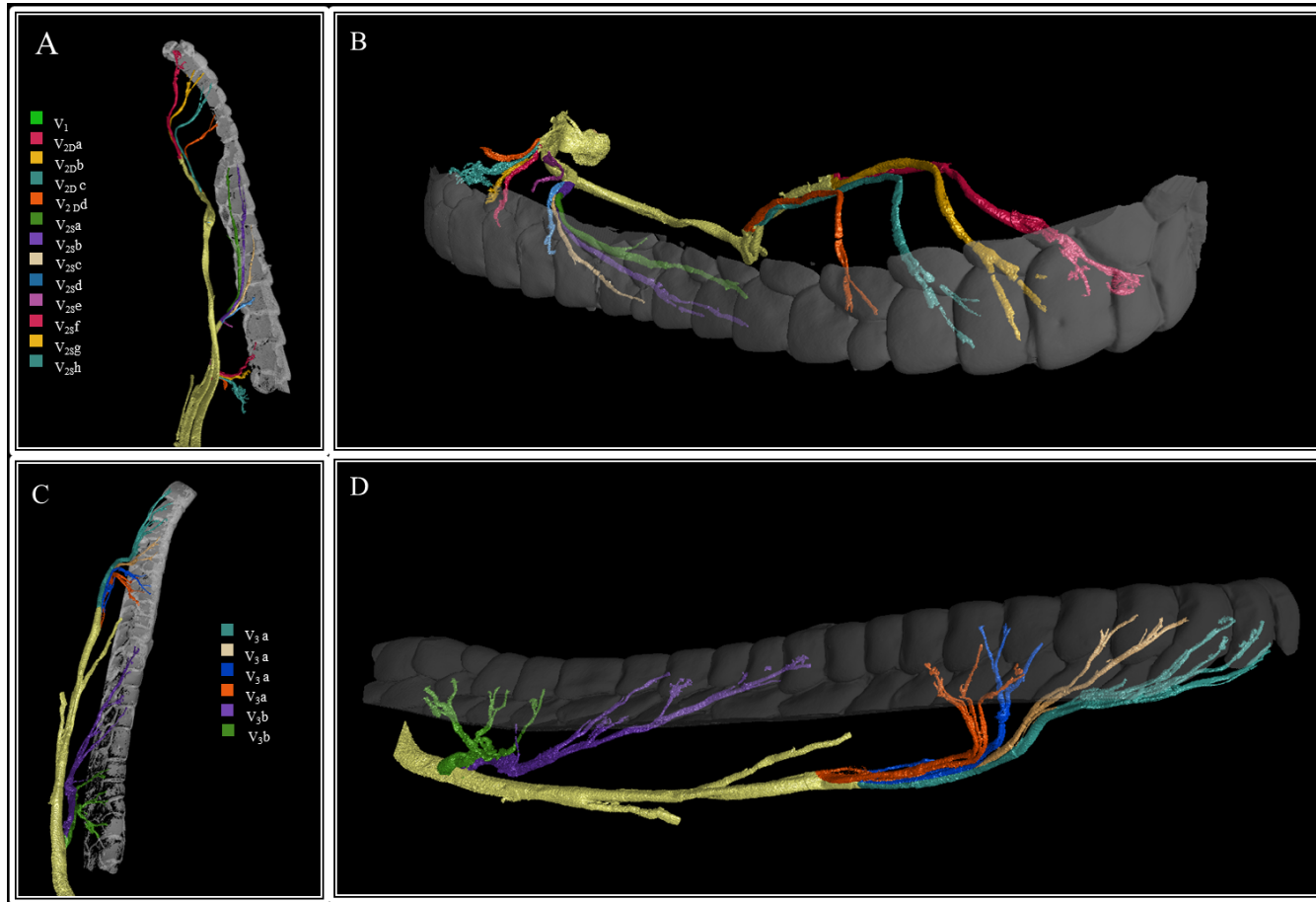
Fig. 3.11. Innervation of the supralabial (A,B) and infralabial (C,D) scales in *Boa constrictor*. Although there are no substantial pit organs in either the supra- and infralabial scales, there is still some sub-branching of all three branches of the trigeminal that innervate the labial scales in this species. The relationship between the nerves and the scales they innervate is shown in both internal view (A, C) and external view (B, D). Inset identifies the colors assigned to individual sub-branches.
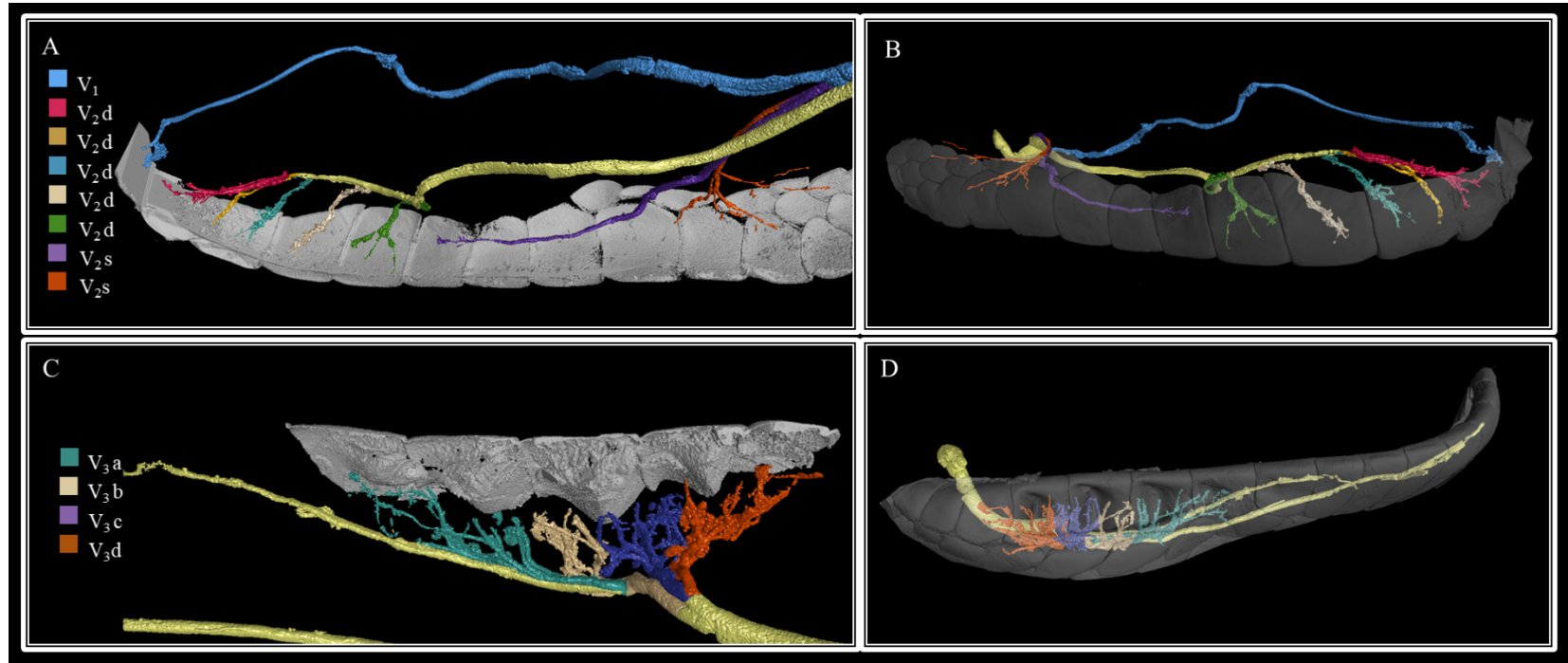
Fig. 3.12. Innervation of the supralabial (A,B) and infralabial (C,D) scales in *Antaresia childreni.* Although there are no pit organs present in the supralabial scales, there is some degree sub-branching of the maxillary nerve is seen innervating the supralabial scales. An infralabial pit array is present, as is extensive sub-branching of the mandibular nerve (V_3). Pit 3 in the infralabial array receives innervation from two sub-branches of V_3. The relationship between the nerves and the scales they innervate is shown both from the internal view (A, C) and external view (B, D). Inset identifies the colors assigned to individual sub-branches.
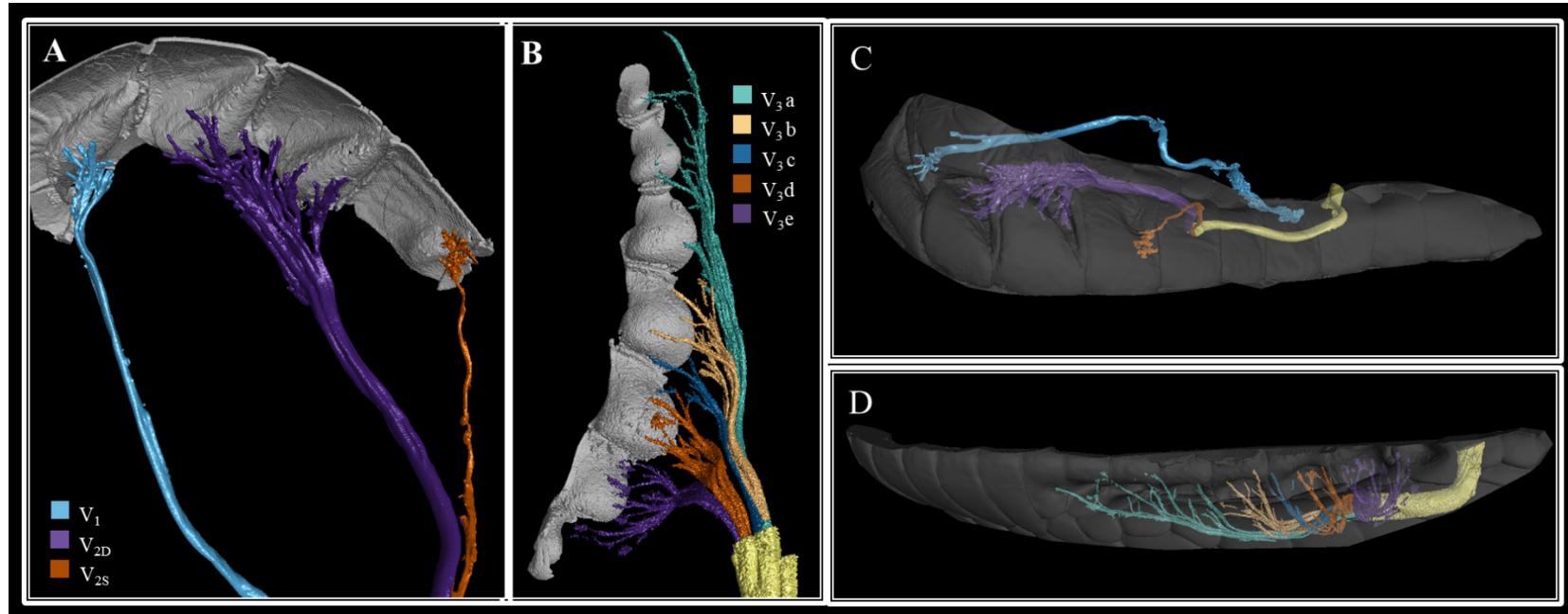
Fig. 3.13. Innervation of the supralabial (A, C) and infralabial (B, D) pit organ arrays in *Morelia spilota.* The rostral pit is innervated exclusively by the ophthalmic nerve (V_1), and supralabial pit 3 is innervated exclusively by the superficial branch of the maxillary nerve (V_2S), whereas supralabial pits 1 and 2 are innervated by both the superficial and he deep branch of the maxillary nerve (V_2D). Pits 4 and 5 in the infralabial array each receive innervation from two sub-branches of the mandibular nerve (V_3), with sub-branch 3 innervating both of these pits. The relationship between the nerves and the scales they innervate is shown in both internal view (A, C) and external view (B, D). Inset identifies the colors assigned to individual sub-branches.
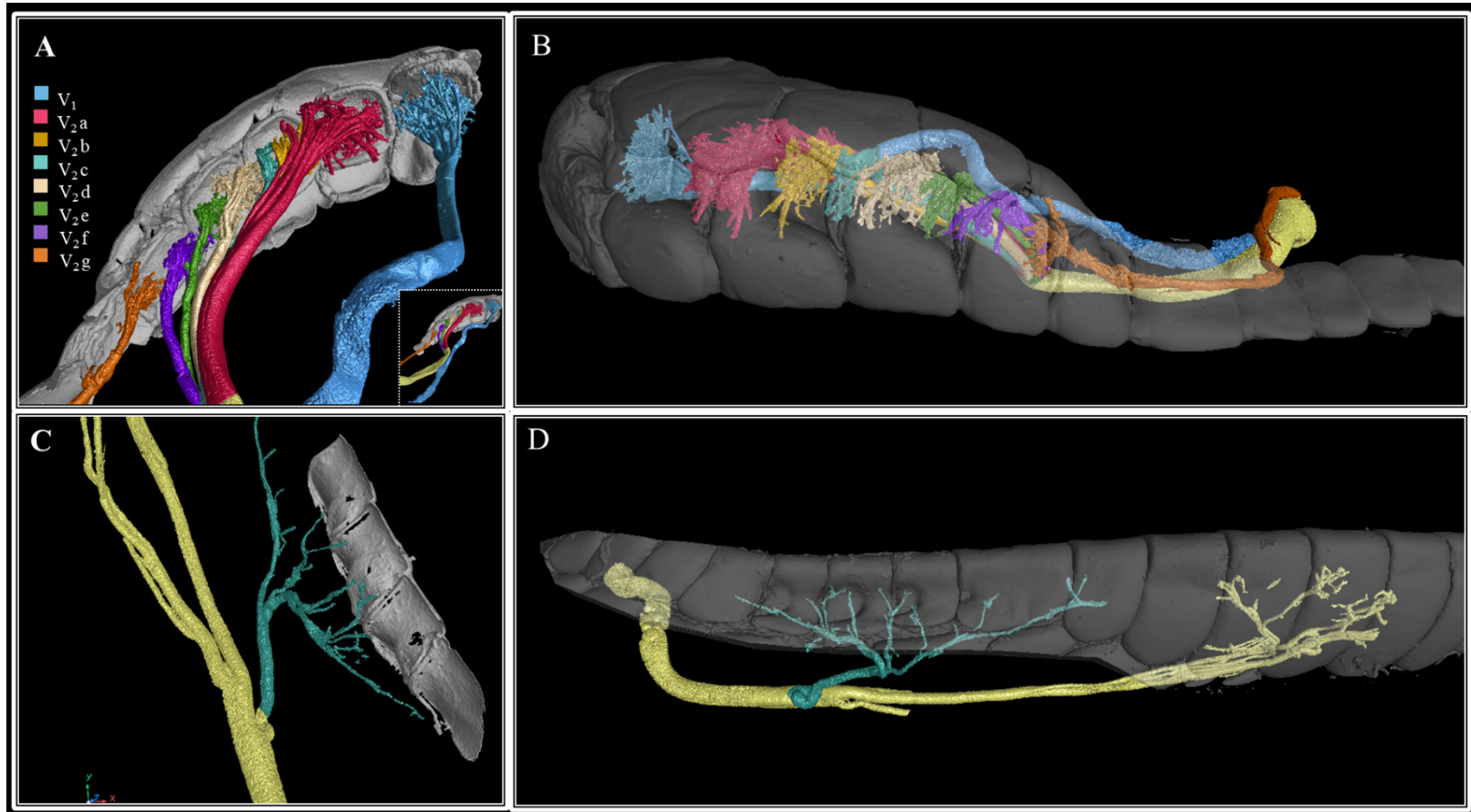
Fig. 3.14. Innervation of the supralabial (A,B) and infralabial (C,D) pit organ arrays in *Python regius*. The rostral pit is innervated exclusively by the ophthalmic nerve (V1), and supralabial pit 1 is nnervated by sub-branch A of the deep branch of the maxillary nerve (V$_2$Da). The remaining pits in the supralabial array each receive innervation from multiple sub-branches of V$_2$, with pit 3 innervated by V$_2$D a-d. The infralabial array is weakly innervated by the mandibular nerve (V$_3$), with no substantial sub-branching of that nerve evident. The relationship between the nerves and the scales the innervate is shown in both internal view (A, C) and external view (B, D). Inset identifies the colors assigned to individual sub-branches
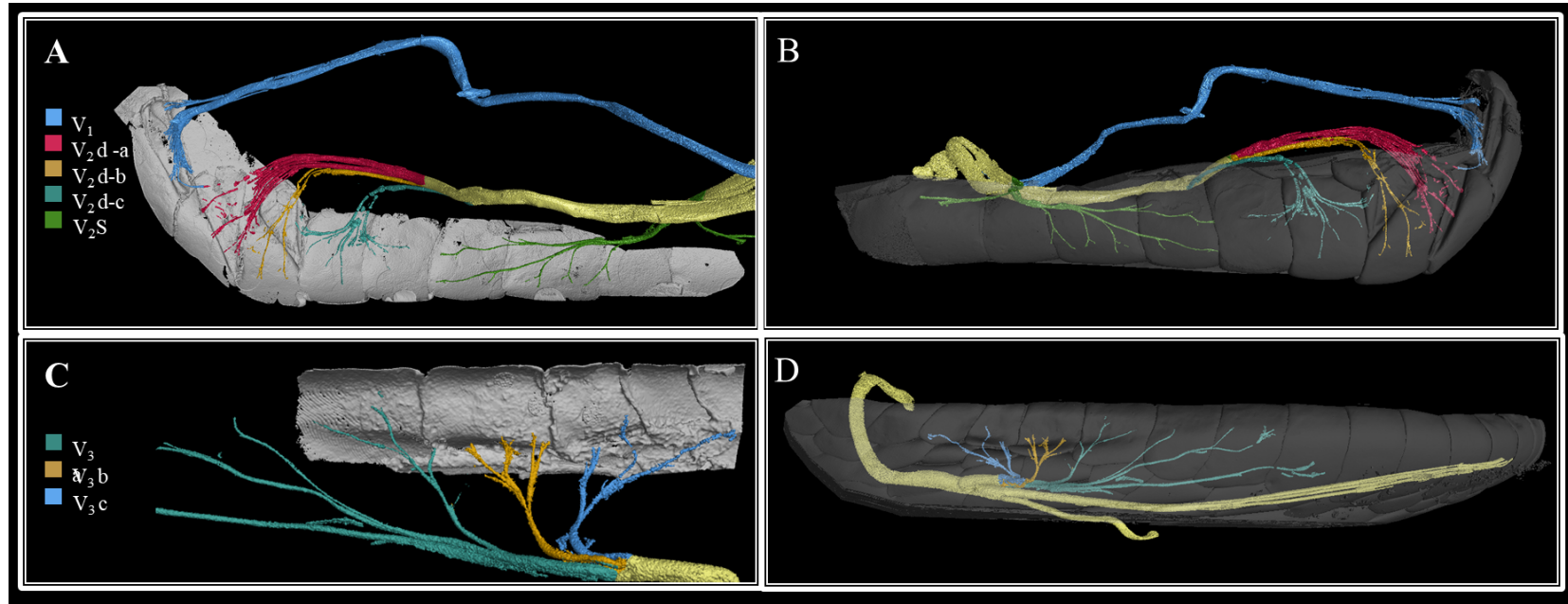
Fig. 3.15. Innervation of the supralabial (A,B) and infralabial (C,D) pit organ arrays in *Python bivittattus.* The rostral pit is exclusively innervated by the ophthalmic nerve (V$_1$), supralabial pit 1 is innervated by sub-branch A of the deep branch of the maxillary nerve (V$_2$Da), and pit 2 is innervated by V$_2$Db. Although the infralabial array is only weakly innervated by the mandibular nerve (V$_3$), three distinct sub-branches of that nerve evident. The relationship between the nerves and the scales they innervate is shown in both internal view (A, C) and external view (B, D). Inset identifies the colors assigned to individual sub-branches

REFERENCES

Bullock, T.H., and W. Fox, 1957. The anatomy of the infra-red sense organ in the facial pit of pitvipers. Quarterly Journal of Microscopical Science 98(2): 219-234.

Bullock, T. H., & Barrett, R. (1968). Radiant heat reception in snakes. Commun Behav Biol, 1, 19-29.

Burns, B. 1969. Oral sensory papillae in sea snakes. Copeia, 1969(3): 617-621.

Callahan, S., J.M. Crowe-Riddell, R. S. Nagesan, J.A. Gray, and A.R. Davis Rabosky, (2021). A guide for optimal iodine staining and high-throughput diceCT scanning in snakes. Ecology and Evolution, 11(17): 11587-11603.

Catania, K. C., D. B. Leitch, and D. Gauthier. 2010. Function of the appendages in tentacled snakes (Erpeton tentaculatus). Journal of Experimental Biology, 213(3): 359-367.

de Cock Buning, T.J.., and P. Dullemeijer. 1977. Thermal receptors in Python reticulatus. Acta Morphologica Neerlando-Scandinavica 15: 237–239.

de Cock Buning, T., R. C. Goris, and S.I. Terashima. 1981. The role of thermosensitivity in the feeding behavior of the pitviper, Agkistrodon blomhoffi brevicaudus. Japanese Journal of Herpetology, 9: 7-27.

Ebert, J. (2008). Infrared sense in snakes (Doctoral dissertation, Universitäts-und Landesbibliothek Bonn).

Goris, R. C., T. Kadota, and R. Kishida. 1989. Innervation of snake pit organ membranes mapped by receptor terminal succinate dehydrogenase activity. Current Herpetology in East Asia: 8-16.

Kishida, R., S.I. Terashima, R. C. Goris., and T. Kusunoki. 1982. Infrared sensory neurons in the trigeminal ganglia of crotaline snakes: transganglionic HRP transport. Brain Research, 241(1): 3-10.

Kohl, T., M.S. Bothe, H. Luksch, H. Straka, and G. Westhoff. 2014. Organotopic organization of the primary Infrared Sensitive Nucleus (LTTD) in the western diamondback rattlesnake (Crotalus atrox). Journal of Comparative Neurology, 522(18): 3943-3959.

Lynn, W.G. (1931). The structure and function of the facial pit of the pitvipers. American Journal of Anatomy 49: 97-139.

Maderson, P. F. A. (1970). The distribution of specialized labial scales in the boidae. Biology of the Reptilia, Vol. 2. (Gans, C. and Pearsons, TS ed.). 301-304.

Nishida, Y., S. Yoshie, and T. Fujita. 2000. Oral sensory papillae, chemo-and mechano-receptors, in the snake, Elaphe quadrivirgata. A light and electron microscopic study. Archives of Histology and Cytology, 63(1): 55-70.

Pisani, G. R. (1973). A guide to preservation techniques for amphibians and reptiles.

Reynolds, R. G., M. L. Niemiller, and L. J. Revell. 2014. Toward a Tree-of-Life for the boas and pythons: Multilocus species-level phylogeny with unprecedented taxon sampling. Molecular Phylogenetics and Evolution, 71: 201-213.

Tan, C. K., and P. Gopalakrishnakone. 1988. Infrared sensory neurons in the trigeminal ganglia of the python (Python reticulatus)—a horseradish peroxidase study. Neuroscience letters, 86(3): 251-256.

Warren, J. W., & Proske, U. (1968). Infrared receptors in the facial pits of the Australian python Morelia spilotes. Science, 159(3813), 439-441.

CHAPTER 4

CEPHALIC VASCULAR PATTERNS AND PIT ORGAN MICROVASCULATURE
OF BOAS AND PYTHONS

INTRODUCTION

While both the morphology and innervation of snake pit organs influence the

sensitivity and function of the infrared-imaging system (de Cock Buning, 1985;

Molenaar, 1992; Bakken and Krochmal, 2007; Bakken et al., 2012), another aspect that

likely impacts heat vision is the blood supply to the pit organs (Amemiya et al., 1999;

Nakano et al., 2000; Goris et al., 2003, 2007). Pit organs are underlain by a dense

vascular network, which is externally and macroscopically evident in some taxa (e.g.,

Python regius) as it lends a pink appearance to the pit fundus (Fig 4.1.). Because pit

organs are used to detect radiant heat and distinguish warm objects (e.g., a prey item

such as a small mammal) from a cooler background (e.g., surrounding vegetation), a

temperature decrease at the level of the pit membrane improves the likelihood of

stimulus detection and prevents the formation of thermal "after-images" (Goris et al.,

2007). Thus, the vascular network is hypothesized to play an important physiological

role: increasing blood supply to the pit organ, and thereby contributing to maintenance

of an optimal thermal state through cooling of the IR-sensitive tissues (Amemiya et al.,

1999; Goris et al., 2003; Goris et al., 2007).

The terminal nerve masses (TNMs) within the pit membrane of crotalines or the

pit fundus of boas and pythons are extremely sensitive to changes in temperature of the

pit membrane, generating action potentials in response to temperature changes as low

as 0.001°C (Bullock and Diecke, 1956; Hensel 1975; de Cock Buning et al., 1981;

Ebert and Westhoff, 2007). In the phototransduction pathway of the visual system, rhodopsin is activated by incoming photons, resulting in hyperpolarization of the retinal cell membrane. This generates a cyclical signal cascade that ultimately brings the membrane back to its depolarized, resting state. It is just as important that the TNMs of the pit organs be returned to a depolarized state following activation, in order for the pits to function effectively as infrared-imaging sensors. However, unlike the lateral eyes of the visual system, the pit organs of the infrared-imaging system lack the photopigments necessary to undergo such a process. Instead, capillary networks supply the pit membrane with blood, and the temperature of this blood is the same temperature as the body of the snake. Blood supply to the pits functions to cool the TNMs, returning them to body temperature, keeping them from constantly generating action potentials, and sending confounding signals to the optic tectum.

Physiological studies of blood flow microdynamics suggest that the blood vessels supplying the pit membrane do indeed function to cool the pit and increase sensitivity to radiant heat (Goris et al., 2003; Goris et al., 2007). When an infrared laser stimulus was applied to only a small area of the pit membrane, researchers observed an increase in blood flow at the point of stimulation (Goris et al., 2007). Severing of the nerve bundles innervating the pits resulted in no changes in blood flow when the same stimulus was presented (Goris et al., 2007). Additionally, capillaries in the pit membrane are extensively contacted by pericytes with projections containing smooth muscle fibers that appear to control vasodilation and vasoconstriction (Nakano et al., 2000). Taken together, the pericytes and their projections to the capillaries of the pit membrane and the observation that change in

blood flow to the pits only occurs with IR-stimulation of the TNMs suggest communication between the TNMs and the adjacent capillary network.

Several studies have used traditional histology and electron microscopy to examine the morphology of the blood vessels associated with the pit organs of crotaline snakes (pitvipers), describing a dense describing a dense and extensive capillary network concentrated within the pit membrane (Fig 4.2 A-B; Amemiya et al., 1999; Nakano et al., 2000; Goris et al., 2003). The vessels of the crotaline pit membrane lie in a single, flat layer of capillary loops, parallel to the TNMs, with each loop encircling a cluster of TNMs (Fig 4.3 A; Amemiya et al., 1999; Goris et al., 2003). Only one such study exists for a member of any other infrared-capable family, wherein researchers demonstrated that *P. regius* also possesses an extremely dense, and morphologically more complex, capillary network (Goris et al., 2003; Goris et al., 2007). In *P. regius*, the vessels do not lie flat within the tissues, but instead project loops toward the surface of the pit membrane (Fig 4.2 C), perpendicular to the TNM layer (Fig 4.3 B). Each loop exhibits a dome-like expansion at its apex, and the authors noted that if the vessels were unspooled, they would resemble "a string of beads" (Goris et al., 2007). The expanded apices of those loops increase the surface area of the vessels in contact with the TNMs. The vessels of slimmer diameter that connect adjacent loops were proposed to slow the passage of blood through the circuit, causing the blood to remain for longer within the pit fundus, thereby absorbing more heat.

The ultrastructure of the capillary networks of pit membranes has been described in several species of pitvipers (Amemiya et al., 1999; Nakano et al., 2000;

Goris et al., 2003) and in one species of python (Amemiya et al., 1996). No previous

works included additional pythonid or boid species. Furthermore, no descriptions of

the overall patterns of the blood supply to the supralabial and infralabial pit arrays

exist, nor do any descriptions of the major vessels supplying those structures. Given

the substantial inter- and intrafamilial variation in the pit organs of boas and

pythons, as well as the extraordinary interspecific variation in patterns of innervation

to those structures (described in Chapter 3), I hypothesized that the species with the

largest and most extensive pit organs would have a more extensive blood supply to

those pits. Here, I expanded taxon sampling to include three species of python (*A.*

childreni, *M. spilota*, and *P. regius*) and two species of boas (*B. constrictor* and *C.*

hortulanus). I used microCT scanning of vascular cast specimens to examine

interspecific variation in the vascular networks of the supra- and infralabial pit

arrays and scales, together with the major vessels supplying those vascular networks.

MATERIALS AND METHODS

Specimen Selection, Acquisition, and Husbandry

To examine inter- and intrafamilial variation in pit organ microvasculature in

pythons and boas, I acquired adults of the following five species: *Antaresia childreni,*

Python regius, Morelia spilota, Boa constrictor, and *Corallus hortulanus.* Unlike many

other anatomical methods, visualization of the microvasculature via vascular casting

requires the use of fresh tissue. Because blood clots rapidly occlude capillaries and other

small blood vessels post-mortem, is essential that clotting be prevented and blood cells be

flushed from the vessels immediately following euthanasia and confirmation of death.

Once blood has been removed, it is necessary to fill the vessels quickly with a compound that preserves the vessels in their normal configuration before they collapse. That is why existing museum specimens, which are useful for many other anatomical studies, cannot be used effectively to study the microvasculature. Therefore, live snakes were acquired and prepared specifically for this study. Most snakes were acquired from commercial breeders, with the exception of *A. childreni*, which were donated from a colony maintained by the DeNardo Lab at Arizona State University.

Prior to vascular casting, live snakes were housed in the Vivarium of the USU Department of Biology, in separate enclosures on newspaper bedding, under a 12:12 light:dark cycle, at ambient temperature of 36°C, and 45% humidity. Snakes were fed a diet of mice or rats, and water was provided ad libitum.

Vascular Casting

Individuals were placed into a glass chamber and profoundly sedated with isoflurane until cessation of the tail-pinch response was demonstrated. Once sedated, the location of the heart was confirmed by palpation, and a longitudinal incision was made in the ventral skin, to expose the heart and the great vessels. The pericardium was carefully opened, and the ventricle exposed to permit delivery of a lethal injection of a 1:3 solution of sodium pentobarbital in heparinized saline to the ventricle. Once death was confirmed by cessation of the heartbeat, the ventricular wall was cut, and a polyethylene catheter, with a small cuff at the tip, was inserted from the ventricle into the right aortic arch (Fig 4.4). Placement of the catheter into the correct vessel was confirmed by injecting a small volume of heparinized saline through the catheter and monitoring which vessel filled with fluid. After confirmation of placement, a ligature was placed around the catheterized

vessel, tightened, and tied, to secure the cuffed catheter. An initial volume of heparinized saline was injected through the catheter, and when the right atrium filled from venous return of the injection mass, the atrial wall was cut to allow blood and saline to drain from the body. Additional heparinized saline, generally about 180-300 ml, depending on the size of the specimen, was injected through the catheter. Clearing of the blood from cephalic vessels was observed by checking for blanching of the oral mucosa. Once the fluid leaving the opened right atrium returned clear, an appropriate volume of Microfil (Table 4.1.), a radio-opaque latex solution, was mixed, drawn into one or more syringes, and injected into the vascular system through the same catheter. The volume of Microfil required to replace the circulating blood was estimated as ~3% of blood volume (Enok et al., 2016), although additional Microfil was mixed and perfused through the tissues to ensure maximal filling of vessels and capillaries. Following delivery of the full volume of Microfil, the specimen was allowed to cure at room temperature for 2 hours. During that time, the syringe remained attached to the catheter to maintain pressure on the vascular system. After ~2 hours of curing, the syringe was removed, and the specimen was fixed in 10% phosphate-buffered formalin (PBF; Appendix A) for at least several days. Often specimens were maintained in 10% PBF even after fixation was complete, rather than being transferred to 70% ethanol, as is standard procedure for museum specimens. Experience suggests that Microfil degrades when exposed to ethanol for long periods of time.

MicroCT Scanning and Reconstruction of 3D Volumes

In order to visualize the intact cephalic vascular system, including the major vessels supplying and draining the pit arrays, heads of vascular cast specimens were

examined using X-ray microcomputed tomography (microCT). To do so, specimens that had been vascular cast and fixed were secured in floral foam (a radio-transparent material) and wrapped tightly in plastic wrap to prevent desiccation and movement during scanning. Wrapped specimens were mounted and centered on a stage inside the chamber of a Nikon XT H 225 ST microfocus computed tomography scanner fitted with a reflection target. High resolution scans of the cephalic blood supply and cranial bones were acquired for each specimen using the parameters listed in Table 4.2.

To achieve even greater resolution of the fine vessels of the pit arrays, I carefully removed the supra- and infralabial scale rows from one individual of each species. Those tissues were placed in microcentrifuge tubes, secured with floral foam, and scanned at resolutions of 2-3.5μm (Table 4.3) with a transmission target.

Following scan acquisition, I used CT 3D Pro reconstruction software (Version 6.8.7977.22560; Nikon Metrology) to generate three-dimensional volumes as both 16-bit VGL files (for use with VGStudio Max) and 16-bit TIFF stacks (for processing in other programs, e.g., 3D Slicer).

Analysis of 3D Volumes

VGStudio Max (Version 3.5, Volume Graphics GnbH) to generate regions of interest (ROIs). The ROIs included the cranial bones, general cephalic vasculature, arterial supply, venous drainage, and the microvasculature of the pit arrays (or labial scales, in those species lacking pit organs in a given region).

RESULTS

Broad patterns of the cephalic vasculature will be described for Pythonidae and Boidae, to provide proper orientation for the vessels of interest: the arterial supply and venous drainage of the supralabial and infralabial pit organ arrays and their associated labial scale rows. As in other vertebrates, the arteries of the head arise from the internal and external carotid arteries, and the veins that drain that blood ultimately converge on the internal and external jugular veins and the spinal vein.

Patterns of Arterial Blood Supply

In the majority of the species examined, the left and right common carotid arteries each split at the angle of the jaw to form the internal and external carotids. The internal carotids extend dorsomedial from this branching point and meet to form an anastomosis at the level of the basioccipital. Following their points of divergence from the internal carotids, the external carotids descend ventromedially to supply many (but not all) features of the lower jaw, while the internal carotids give rise to the facial and mandibular arteries.

In all taxa examined, from both families, the mandibular artery diverges from the facial carotid and immediately descends ventrolaterally to enter the mandibular fossa. As it continues on its rostrad path through the compound bones, and then the dentaries, it gives rise to three sub-branches. The first of these branches exits via the mandibular foramen of the compound bone to supply the soft tissues in a portion of the infralabial scale row (as in *B. constrictor*, which lacks pits) or the caudal infralabial pit organ arrays (in all other taxa examined). The other two sub-branches exit via foramina located closer to the rostral end of the dentary bone, to supply adjacent facial tissues. Beyond supplying

soft tissue structures lateral to the inferior tooth rows, the mandibular artery also supplies blood to these teeth and to the dental lamina, wherein successive generations of replacement teeth are formed.

Following their divergence from the mandibular arteries, the facial carotids further divide to supply blood to the orofacial regions of the upper jaws. The inter- and intrafamilial variations in arterial patterning that most directly impact blood supply to the pit organs are those that emerge from the facial carotid, as described below.

Pythonidae

There is noticeable asymmetry in the left and right facial carotids in pythonids. On both the left and right sides, the pterygoid artery emerges from the facial carotid at the level of the prootic and extends anterolaterally along the dorsal surface of the pterygoid. The pterygoid artery exhibits a sharp medial curve at the point of articulation between the pterygoid and ectopterygoid, as it extends to supply the muscles and tissues caudolateral to the orbit, terminating posterior to the orbit.

The left and right facial carotids continue anteromedially, following the divergence of the pterygoid arteries, to the rostral edge of the parietals. This is the anterior extent of the right carotid, but the left facial carotid divides at this point, sending branches through the optic foramina on either side of the skull. These branches further split into the infraorbital and supraorbital arteries, the latter extending rostrally and then ventrally. As the infraorbital artery extends rostrally, the pterygopalatine artery branches from the ventral surface of the infraorbital artery, just dorsal to the articulation between the pterygoid and palatine bones, projecting ventrocaudad before curving sharply and extending laterad over the point of articulation between the ectopterygoid and maxilla.

The infraorbital artery continues to travel rostrally ventromedial to the eye, curving to pass through a foramen in the palatine bone. As it passes through this foramen, it splits to form the palatine and maxillary arteries. The palatine artery sends branches to the palatine dentition and surrounding soft tissue structures in the roof of the mouth. The maxillary dentition is supplied by the maxillary artery, which also sends sub-branches through the maxillary foramina to supply blood to the supralabial scale rows.

The basilar artery arises immediately caudal to the carotid anastomosis, and first extends along the ventromedial surface of the braincase. It forms an anastomosis with the medial branch of the right facial carotid as it extends forward. The basilar artery passes dorsally over the point where the left facial carotid splits as the cerebral artery. This rostral trajectory continues along the dorsal surface of the parabasisphenoid. It divides initially at the rostral edge of the frontal bones, sending a branch through a foramen into the nasal bone, which then splits into the lateral and medial nasal arteries. The medial nasal artery passes between the vomer and septomaxilla, then through a foramen on the premaxilla to supply the rostral scale.

This pattern of arterial blood supply is largely the same in all three species of pythons examined, with the tissue of the rostral and supralabial scales (i.e., the scales in which the pit organs form) supplied by the nasal and maxillary arteries, respectively. However, there are some interspecific differences:

1. The two individuals of *A. childreni* (Fig 4.5) examined lack any external evidence of pit organs in the rostral and supralabial scales, and possess only minor arterial supply to those facial regions.

2. *Morelia spilota* (Fig 4.6) possesses four pit organs in its supralabial array, which extend laterocaudally around the curve of the rostrum. Each of those pits is shaped like an inverted teardrop. The medial portion of the rostral pit receives blood via the lateral nasal artery, whereas the lateral portion is supplied by a sub-branch of the maxillary artery that emerges from the rostralmost maxillary foramen. Sub-branches emerging from the second and third maxillary foramina supply the first supralabial pit organ. The second supralabial pit organ is served by sub-branches emerging from the third and fourth maxillary foramina, while the third supralabial pit (the most caudal pit in the supralabial array) receives sub-branches from the fourth maxillary foramen only.

3. The arterial blood supply to the supralabial pit organs in *P. regius* (Fig 4.7) is notably more complex. The rostral pit is supplied by the medial nasal artery via several substantial sub-branches, which together extend from the nasal artery as iy curves ventrally over the front of the snout. The palatine artery passes through a foramen on the palatine, extending medially, and then rostrally, where it anastomoses with the medial nasal artery. Each of the supralabial pit organs is supplied by sub-branches of the maxillary artery, which emerge from the maxillary foramina and form looping anastomoses beneath each pit. The supraorbital artery continues forward along the interior surface of the frontal bone, beneath the roof of the skull, and curves laterally to pass through a foramen of the prefontal bone. At this point, the supraorbital artery forms an anastomosis with the rostralmost extent of the main maxillary artery as it emerges from the caudalmost foramen of the maxilla.

Boidae

The arterial supply in both species of boids examined (*B. constrictor* and *C. hortulanus*) exhibits almost entirely the same pattern, with subtle differences existing between those who possesses deep, obvious pit arrays (*C. hortulanus;* Fig 4.8) and those whose pit arrays are less well defined (*B. constrictor;* Fig 4.9) of pit arrays. The asymmetry of the arterial supply to the cranium and upper jaw is less pronounced than in the pythons, although it is still evident.

After the mandibular artery descends, the facial carotid gives rise to the pterygoid artery. This artery emerges substantially farther forward in *B. constrictor* than in *C. hortulanus*. In the latter species, the pterygoid artery emerges at the point of bifurcation between the facial carotid and mandibular arteries. The left and right facial carotids continue on a rostromedial trajectory along the floor of the braincase, before meeting to form an anastomosis at the level of the basioccipital.

Immediately caudal to the point of anastomosis between the left and right facial carotids, the right facial carotid gives rise to the cerebral artery. The cerebral artery extends rostrally through the braincase, and divides into both of the common nasal arteries at the rostral edges of the frontal bones. The common nasal artery passes through the nasal bone and as it does so, it further divides into the lateral, medial, and ventral nasal arteries. The medial nasal artery then passes between the vomer and septomaxillary bone, and then through a foramen in the premaxilla to supply the rostral scales.

Differences in the blood supply to the upper jaw and nasal region in boids begin at the point where the facial carotid arteries anastomose. The following differences were observed between the two species examined:

1. In *B. constrictor* (Fig 4.9), a short, laterally curved branch of the facial carotid artery arises and passes through the optic foramen. This branch immediately forks, and the rostralmost branch forms the infraorbital artery. The caudal branch bifurcates again, to form the supraorbital and pterygopalatine arteries. The pterygopalatine extends laterally to exit the orbit, before curving and extending rostrally along the supralabial scales. The infraorbital artery passes through a foramen on the prefrontal bone, before splitting into the maxillary and palatine arteries. A sub-branch of the maxillary artery passes through the rostralmost maxillary foramen, then bifurcates. The more anterior branch wraps around the curve of the rostrum, and the other branch extends caudally to anastomose with the pterygopalatine artery.

2. In *C. hortulanus* (Fig 4.8), unlike *B. constrictor*, the short branch from the facial carotid anastomosis is absent. Instead, the pterygopalatine splits directly from the anastomosis, just medial to the optic foramen. Both resulting arteries pass through the optic foramen together, and the infraorbital artery extends through a foramen on the prefrontal bone before bifurcating into the maxillary and palatine arteries. The pterygopalatine artery extends laterally to exit the orbit, before curving sharply rostral. As it extends rostrally, the pterygopalatine artery gives rise to several sub-branches that supply the caudal supralabial pit array of this species, which are comprised of depressions between the supralabial scales just below the orbit.

Patterns of Venous Drainage in Pythons and Boas

The venous drainage of the lower jaw, upper jaw, and braincase generally conforms to the one complete account of the cephalic veins based on another lineage of snakes. Bruner (1907) described the major cephalic veins of *Tropidonatrix natrix* (now *Natrix natrix*, sensu lato, Colubridae: Natricinae). Broadly, that pattern of venous drainage is as follows:

The infralabial region, including the infralabial pits when present, is drained by the mandibular vein, which travels caudally along the lower jaw before curving ventrolaterally beneath the jaw to contact the internal jugular vein. Beneath the pit array, the mandibular vein receives blood from the capillary network via a delta-like series of venules that converge to form the larger collecting veins, mirroring the shape formed by the nerve supply to these pits. Very little variation is observed in the venous drainage of the caudal infralabial pit organs, and a similar pattern is even observed in *B. constrictor*, which lacks pit organs.

As it projects laterally from the midline of the snout, the rostral vein of each side gives rise to the medial and lateral nasal veins, the maxillary vein, and the supralabial vein. The medial and lateral nasal veins travel caudally from their points of origin to meet behind the nasal capsule, where they form the common nasal vein. The common nasal vein anastomoses with the palatopterygoid vein, which emerges from the subnasal sinus. A secondary anastomosis of the palatopterygoid vein occurs with the maxillary vein at the level of the prefrontal. The palatopterygoid vein ultimately drains directly into the internal jugular vein. The common nasal vein, maxillary vein, and supralabial veins, which carry blood from the rostral and supralabial regions, all drain into the orbital sinus.

Blood from the orbital sinus, in turn, drains into the common posterior vein, and ultimately to the internal jugular vein.

Inter- and intrafamilial differences in venous drainage are observed in regions where the arterial blood supply is also modified to accommodate the rostral and supralabial pit organs:

1. For the scales within which lie the rostral and supralabial pit organs of *P. regius*, the dorsal and, to a lesser extent, lateral margins are bracketed by veins that drain the dense capillary networks within these scales (Fig 4.7). In the case of the rostral and first two supralabial scales, this role is served by the rostral vein. At the dorsal center of the second supralabial pit organ, the rostral vein sends a branch dorsomedially, as the lateral nasal vein. This bracketing of individual supralabial pits is not observed in *M. spilota* (Fig 4.6).

2. Both *P. regius* and *M. spilota* possess an extensive vascular plexus covering the nasal and rostral regions of the head. The plexus appears venous in nature, draining into the medial and lateral nasal veins (Fig 4.6; Fig 4.7). The location of this dense vascular plexus suggests a functional association with the rostral and anteriormost supralabial pit organs, and perhaps also with the tissues within the nasal capsule in both species. This vascular plexus is much more pronounced in *M. spilota* than in *P. regius*, and it is present to a considerably lesser degree in *A. childreni* (Fig 4.5). In both boas, a vascular plexus covers the region of the nasal capsule, but it does not involve the supralabial scales (Fig 4.8; Fig 4.9).

3. The caudal supralabial pits of *C. hortulanus* are drained by a vein that enters the orbit at the ventrocaudal margin and immediately anastomoses with the orbital sinus.

Pit Organ Microvasculature

When pits are viewed in transverse section, using the microCT images of vascular cast specimens, a distinct "clear area" between capillary network of the pit organ and the deeper vessels that supply and drain them (Fig 4.10). This is true for all pit-bearing taxa examined.

Pythonidae

Python regius

The looping arrangement of vessels previously described in *P. regius* by Goris et al. (2003) was readily observed, even in lower resolution scans. The scans reveal that the capillary networks underlying the membranes in the rostral and supralabial pits of *P. regius* are exceptionally dense (Fig 4.11A-C), whereas those underlying the caudal infralabial array are relatively sparse (Fig 4.11D). Beyond visualizing the capillary loops and their expanded apices, use of microCT scans allowed for visualizing the extent of the vessels supplying and draining the loops, as well as establishing the relationship between adjacent loops and the microvascular elements from which they arise (Fig 4.11).

Each vascular element within the dense array of looped vessels arises from arterioles of the maxillary artery. The latter branches for the distal one-third of its length into two to three sub-branches, each of which gives rise to the loops that are in contact with the pit membrane (Fig 4.11). These loops appear to connect to each other

occasionally at the level of the pit membrane, and there also appear to be connections between adjacent arterioles at various points along their lengths. The veins that drain the capillaries of the pit membrane in *P. regius* seem to anastomose with the capillary bed at points along the perimeter of the pit, that appear to be draining into the veins that bracket the pit-bearing supralabial scales dorsally.

Morelia spilota

Attempts to segment the microCT images of the capillary loops of *M. spilota* were not entirely successful, but it appeared that some capillary loops contacted the pit membrane in both the supra- and infralabial pit arrays (Fig. 4.12 A-D). In the rostral and supralabial pits of *M. spilota*, the blood supply to the pit membrane does not appear to be as dense or as highly organized as that of *P. regius*, whereas that of the infralabial array was noticeably more substantial in *M. spilota* than in *P. regius*. The vessels surrounding the rostral and supralabial pit organs are large and numerous, and appear to associate directly with the extensive venous plexus of the rostral and nasal region in this species. In the infralabial scale row, the arterioles terminating at these capillary beds traveled to their destination along with the respective sub-branches of CN V_3 that innervated a given pit in the array (Fig 4.12C).

Antaresia childreni

There was no evidence of rostral or supralabial pit organs in the two individuals of *A. childreni* examined, although occasional weak depressions are reportedly present in some individuals (Kluge, 1983). The lack of pit organs was reflected in a notably less organized capillary network underlying the rostral and supralabial scales (Fig 4.13 A).

The caudal infralabial pit arrays in this species are well developed and consist of three to five pits each. A relatively flat layer of interconnected capillaries lies just deep to the fundus of each pit and apparently is in contact with the pit membrane (Fig 4.13 B-C). The morphology of the capillary network differs from that reported in *P. regius* by Goris et al. (2002), in that the loops do not project as strongly perpendicular to the fundus. Nonetheless, bulbous expansions at the apex of each loop are present (Fig 4.13 B). There are also fewer projections from the arterioles supplying the network in *A. childreni*, compared to *P. regius.*

Boidae

Boa constrictor

The supra- and infralabial scale rows of *B. constrictor* exhibit the typical arrangement of capillaries expected in labial scales lacking pit organs (Fig 4.14 A-B). Facial scales in this species are distinctly hexagonal, whereas the labial scales are pentagonal and verticaly elongate. Small vessels closely follow the borders of these scales, such that the division between adjacent labial scales is marked by a vertical vessel (Fig 4.14 A-B). Unfortunately, the quality of the vascular casts of *B. constrictor* were relatively poor, and it appears that many of the capillaries within the labial scales did not fill completely in any of the three individuals prepared. It is also possible that, lacking pit organs, the microvasculature presented greater resistance to Microfil than in species with pits.

Corallus hortulanus

The vessels forming the borders of adjacent labial scales are similarly present in *C. hortulanus*, although this species also exhibits a modified capillary network deep to the infrared-sensitive tissues in the supra- and infralabial pit arrays, similar to that observed in the pythons (Fig 4.15; Fig 4.16). There is a consistent difference between the capillaries in labial scales that lack pits (Fig 4.16 A, C) and those where pit organs are present (Fig 4.16 B, D). In the former, the capillaries are somewhat irregular and are arranged in a net-like pattern several layers deep. The capillary networks underlying the supra- and infralabial pit organs are much more highly organized. As in the pythonid species examined, the organized capillary network is clearly associated with the infrared-sensitive regions of the pit arrays. In transverse sections of the supra- and infralabial arrays, there are clear aggregations of capillaries on the rostral and caudal edges of each pit-bearing scale (Fig 4.15 C, D).

DISCUSSION

Strengths and Weaknesses of Vascular Casting

Vascular casting is an effective method of visualizing the macro- and micro-vasculature, but it is not without its difficulties. Even assuming that all steps leading up to and including placement of the catheter proceed perfectly (a process that is technically challenging), problems can still arise during the perfusion itself. Blood clots can impede filling of fine vessels, air bubbles in the Microfil can result in gaps in the cast, and excessive injection pressure can result in ruptured vessels. The possibility of vascular rupture, especially at the level of the capillaries, is a persistent problem, leading to small

masses of extravascular casting medium. Conversely, however, insufficient perfusion pressure can lead to incomplete filling, which constitutes a greater problem for studies of microvascular anatomy. Early attempts to perfuse tissues at physiological pressure resulted in incomplete filling of capillaries, whereas higher pressure can exaggerate the diameter vessels with thinner walls, such as the larger veins.

Inclusion of *P. regius* may seem redundant, as the microvasculature supplying the pit membrane in this species had already received substantial attention in previous works (Amemiya et al., 1996; Goris et al., 2003). However, I wished to compare the details of the microvascular network of the pit organs as revealed by Microfil with that previously described from scanning electron microscopy of corrosion casts. The results reported here confirmed the efficacy of Microfil as a casting medium for even dense microvascular networks. Both methods have their advantages. Corrosion casting media tend to be less viscous, providing an image of the vasculature at more nearly physiological pressure. However, corrosion casts are brittle, and the microvasculature of only a small area can be studied at one time. Microfil provides a flexible cast, which can be easily dissected, and the application of microCT can place the area of interest in a broader anatomical context. Beyond employing *P. regius* for validation of Microfil as a medium for casting dense vascular networks, I also sought to examine the broader pattern of blood supply to and from the pit organs, both in *P. regius* and in the other pythonid and boid taxa examined. That pattern of vascular supply to the pit organs had not been considered in previous studies.

Arteries and Veins

Observations of the major cephalic vessels generally align with descriptions of the arteries (von Bourgondien and Bothner, 1969) and veins (Bruner, 1907) of other snake lineages. Despite some interfamilial variation in overall cephalic arterial patterns, the major arteries supplying the supra- and infralabial pit arrays (or labial scale rows, when pits are absent) are the same in each taxon. This is largely true for the veins as well.

Major differences in the arterial supply to the regions of interest primarily occur at the level of the arterioles. When a pit organ is present within or between one or a pair of labial scales, the arterioles consistently send extensions perpendicularly to the pit fundus or sensory region, to supply the capillary beds. Where pits are absent or not exceptionally well defined (as in *Boa constrictor*), so too are these perpendicular projections. In transverse sections, the larger vessels deep to those projections and the capillary network that they serve appear as two relatively dense and distinct layers. The space between those layers is interspersed with arterioles, but in microCT scans of cast but unstained tissues, the space largely appears empty. That seemingly empty space apparently contains the sub-branches of the trigeminal nerve as they approach the pit membrane. In histological sections of late-stage embryos of *Python regius* (described in Chapter 2) the apparently empty space appears to represent a supportive collagen network through which smalls vessels and nerve fibers extend to contact the pit fundus.

The vascular plexus of pythons implicates the rostral and first few sets of supralabial pit organs, and also extends caudally over the nasal capsule. Previous studies in the crotaline snake, *Crotalus durissus*, have utilized infrared thermography to examine the feeding success relative to degree of evaporative respiratory cooling of the rostral

tissues (Cadena et al., 2013). When the rostrum was cooled, targeting and striking

performance was improved, and the snakes examined altered their respiratory rate when

presented with a prey item (Cadena et al., 2013). This suggests that pit organ temperature

is passively maintained by the microvasculature underlying the pits, and augmented by

respiration. Given the association of the python vascular plexus with the pits at the

anterior of the rostrum and with the tissues of the nasal region, it is possible that pythons

also benefit from a similar respiratory cooling process.

Microvasculature of the Pit Organs

Goris et al. (2003) likened the capillaries of the pit fundus of *P. regius* and their

expanded apices to a string of beads, suggesting that if one were to align them

"anastomosis to anastomosis" they would appear as such a string. Passive control of

blood flow would occur along this length as it flowed from the narrower diameter

connections (strings, in this analogy) to the bulbous expansions (the "beads"). This is

perhaps true within a given loop, but it does not consider the relationship between

adjacent loops, or between their respective arterioles, involving connections that occur

deeper beneath the fundus. The loops extend from arterioles, and there are connections

not just between adjacent loops, but also between adjacent arterioles as they approach the

fundus. Ultimately, the arterioles within a given pit organ in the supralabial receive blood

from the same sub-branch of the maxillary artery, and those in the mandibular array from

the mandibular artery.

My observations suggest an arrangement of vessels that is much less tidy, though

no less intricately organized and interconnected. Rather than a string of beads, I propose

that, if cut at the point of divergence from their major artery and of convergence into their

major vein, and then flattened, the microvasculature would form a shape more akin to a

spiderweb. In *Agkistrodon blomhoffi*, the network of uniform-diameter capillaries in the

cup-shaped pit membrane is weblike, with arterioles extending parallel to the base of the

membrane (Fig 4.2 A-B; Amemiya et al., 1999). Rather than running parallel to the

fundus, the arterioles supplying the capillary network in boas and pythons project

perpendicular to the pit fundus (Fig 4.2 C, Goris et al., 2003; Fig 4.11). Ignoring the

irregularity in capillary diameter and the perpendicular orientation of the arterioles

supplying the capillaries in boids and pythonids, the weblike arrangement I am proposing

would be similar to that observed in pitvipers. This proposed arrangement is more

obvious in *A. childreni* (Fig 4.13) and *C. hortulanus* (Fig 4.15)*, both of which have

capillary networks that already lie in a much flatter layer beneath the pit fundus than that

of *P. regius*.

Previous studies have examined the regions of IR-sensitive tissues in the pits of *P.
regius* (Amemiya et al., 1996) and *C. hortulanus* (Ebert, 2007) using succinate

dehydrogenase (SDH) staining of the mitochondria of the TNMs. The infrared sensitive

tissues of *P. regius* are concentrated at the base of the pit fundus (Fig 4.17 A), and

microCT confirms what others have observed using histology and electron microscopy,

that the capillaries are in direct contact with the TNM-rich layer of the fundus. As a boid,

the "pit organs" of *Corallus hortulanus* are not truly pits, but rather are depressions

formed between the margins of adjacent labial scales. Ebert (2007) similarly used SDH

staining for mitochondrial rich TNMs and determined that, in *C. hortulanus*, the IR-

sensitive tissues occur on the rostral and caudal margins of these scales (Fig 4.17 B-C).

The regions of increased and specialized vascular supply that I observed in that species correspond with the reported locations of the TNMs.

The close association of a morphologically distinct capillary network and the infrared-sensitive tissues of the pit organs of pythons and boas suggests a few things:

1. *Supplying oxygen and nutrients to the pits*: The TNMs within the pit membrane or fundus are rich in mitochondria. While a high level of mitochondria is common to the tissues of sensory organs generally, the number of mitochondria in the TNMs of IR-imaging snakes is much higher than is typical (Terashima and Goris, 1970; Amemiya et al., 1996). Increased blood supply to regions of dense innervation functions in providing the infrared-sensitive tissues and the nerves that supply them with oxygen and nutrients necessary to sustain these sense organs.

2. *Maintenance of an optimal thermal state*: Dense microvasculature at the level of the pit organ may, as previously suggested (Amemiya et al., 1996; Goris et al., 2003; Goris et al., 2007) serve to cool the pit organs of pythons by controlling the flow of blood to and from the IR-sensitive tissues. While the morphologically more complex arrangement of vessels in *P. regius* perhaps confers an advanced degree of cooling to the pits of this taxon, the looping arrangement of vessels and their expanded apices were observed in all pit-bearing taxa examined. This suggests that all taxa that possess this microvascular morphology are similarly capable of controlling blood flow to the pits and thus maintaining them at an optimal thermal state.

3. *Conservation of cell signaling pathways*: In crotaline snakes the pit microvascular network is flattened and tightly arranged within a thin pit membrane. All of the

pythons and boas examined exhibit a similar web-like connection of vessels, though absent the spatial constraints of the crotaline pit membrane, the vessels send projections perpendicular to the IR-sensitive tissues of the pit. Nevertheless, a modified, web-like microvascular network underlies the pit organs of all taxa that possess them. This network is also consistently closely associated with the TNMs, and IR-stimulation has been shown to affect blood flow in this network in both pitvipers and pythons. This suggests a conservation of the cell-signaling pathways that control pit organ development, specifically the processes that underscore concurrent recruitment of the blood vessels and trigeminal nerve branches to the peripheral tissues during pit invagination.

TABLES AND FIGURES

Table 4.1. Volumes of Microfil components mixed for each vascular cast specimen. Blood volume was calculated ~3% of body mass, and the total volume of Microfil delivered was intended to consistently exceed this volume to ensure complete filling of the entire vascular system.

Taxon	ID #	Body Mass (g)	Microfil Compound (mL)	Diluent (mL)	Curing Agent (mL)	Total Volume of Microfil (mL)
Antaresia childreni	HBP-013	520.40	19.2	24	2.16	40
	HBP-014	525.12	19.2	24	2.16	40
Morelia spilota	HBP-015	4082.34	72	90	8.1	150
	HBP-016	3629.20	72	90	8.1	150
Python regius	HBP-044	159.80	19.2	24	2.16	40
	HBP-045	161.65	19.2	24	2.16	40
	HBP-046	165.19	19.2	24	2.16	40
	HBP-047	166.81	19.2	24	2.16	40
	HBP-048	181.78	19.2	24	2.16	40
Boa constrictor	HBP-023	150.21	4.8	6	0.4	10
	HBP-024	250.45	4.8	6	0.4	10
	HBP-025	165.31	4.8	6	0.4	10
Corallus hortulanus	HBP-018	135.20	4.8	6	0.4	10
	HBP-019	133.15	4.8	6	0.4	10
	HBP-020	140.10	4.8	6	0.4	10
	HBP-021	135.65	19.2	24	2.16	40
	HBP-030	136.19	19.2	24	2.16	40
	HBP-040	199.81	19.2	24	2.16	40

Table 4.2. MicroCT scan parameters for each specimen examined using a reflection target.

Species	ID #	Beam Energy (kV)	Beam Current (µA)	Pixel Spacing (µm)	Exposure (ms)	Gain (dB)
A. childreni	HBP-013	80	200	13	1000	18
	HBP-014	80	125	13	1000	24
M. spilota	HBP-015	80	200	29	250	18
	HBP-016	80	200	26	250	18
P. regius	HBP-044	90	200	17	1000	18
	HBP-045	90	200	15	1000	18
	HBP-046	90	200	14	1000	18
	HBP-047	130	100	13	2000	12
	HBP-048	130	100	13	2000	12
B. constrictor	HBP-023	80	200	11	250	18
	HBP-024	95	100	13	1000	24
	HBP-025	80	150	11	250	18
C. hortulanus	HBP-018	80	200	15	250	18
	HBP-019	80	200	14	250	18
	HBP-020	85	200	17	250	18
	HBP-021	85	200	14	1000	18
	HBP-030	85	200	16	1000	18
	HBP-040	85	200	16	1000	18

Table 4.3 MicroCT scan parameters for the supralabial and infralabial scales and pit arrays examined using a transmission target.

Species	Scale Row	Beam Energy (kV)	Beam Current (μA)	Pixel Spacing (μm)	Exposure (ms)	Gain (dB)
A. childreni	Supralabial	85	24	2	2000	24
	Infralabial	85	24	2	2000	24
M. spilota	Supralabial	85	24	3.5	2000	24
	Infralabial	85	24	3.5	2000	24
P. regius	Supralabial	90	22	2	1000	24
	Infralabial	85	24	2	2000	24
B. constrictor	Supralabial	85	24	2	2000	24
	Infralabial	85	24	2	2000	24
C. hortulanus	Supralabial	85	24	2	2000	24
	Infralabial	85	24	2	2000	24

Fig. 4.1. Photograph of the supralabial pit array of *Python regius*. The tissues of the pit fundus receive their pink coloration from the dense capillary network that supplies them. Arrows indicate each of the pits in the supralabial array [Photo credit: Rachel Keefe]
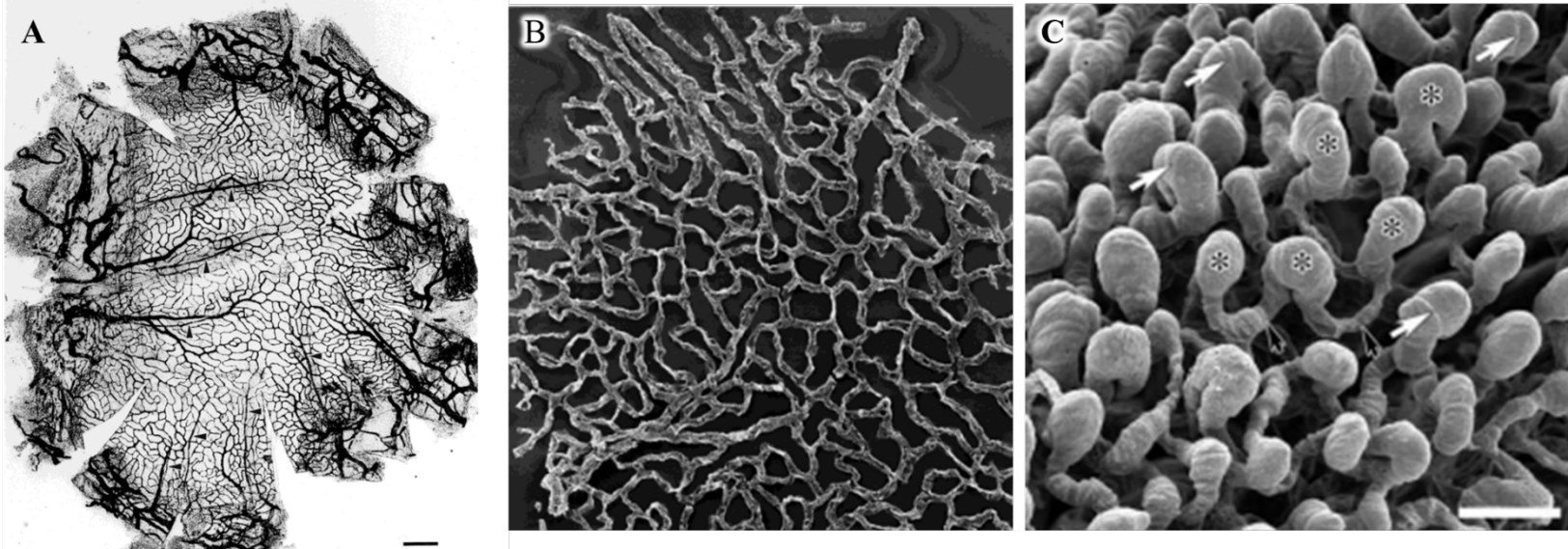
Fig. 4.2. The microvasculature underlying the pit organs in crotaline snakes (A, B) lies flat within the thin pit membrane, whereas that of the fundus in python pits is arranged in loops that project perpendicularly to the pit membrane (C). The microvasculature of the pit organ of *Agkistrodon blomhoffi* is shown following perfusion with India Ink (A) and in a scanning electron micrograph of a corrosion cast (B) [from Amemiya et al. (1999)]. The pit organ microvasculature of *Python regius* (C) is depicted in a scanning electron micrograph of a corrosion cast [from Goris et al. (2003)]
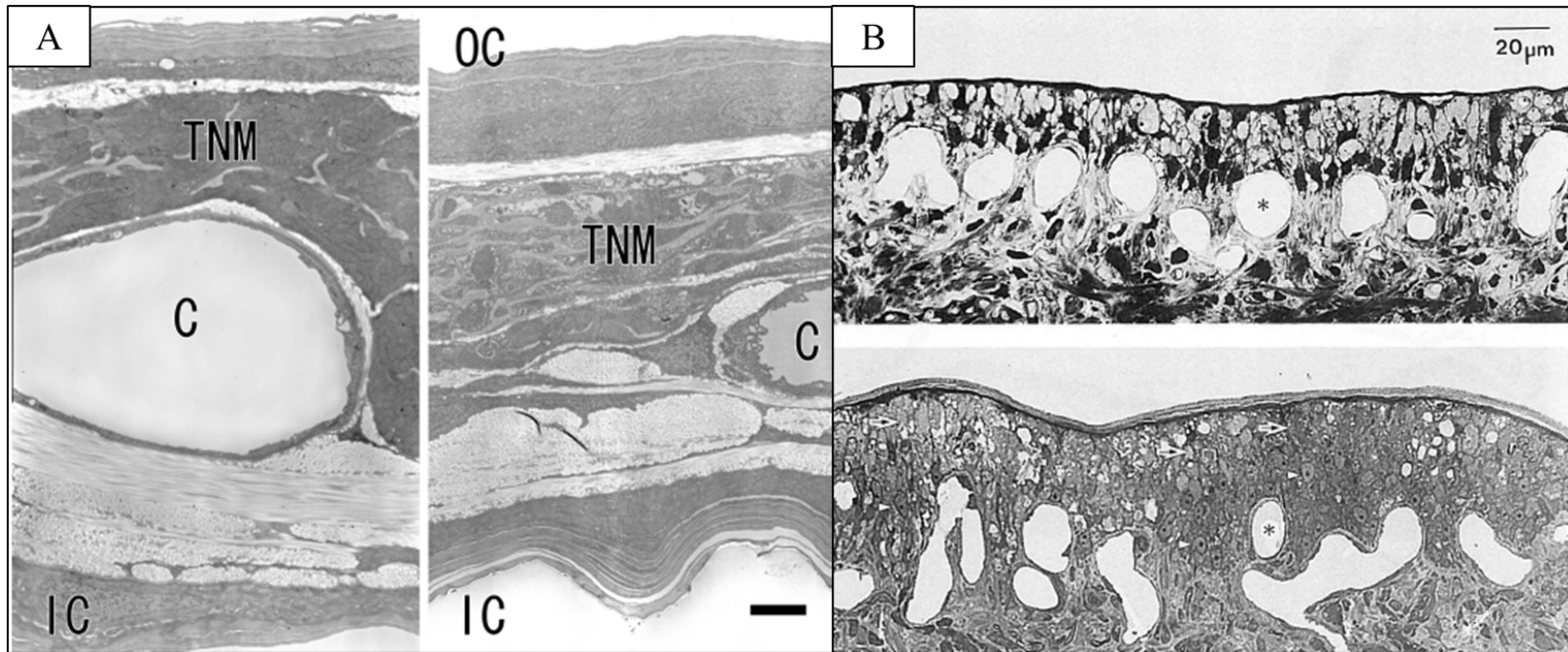
Fig. 4.3. The association between the capillaries of the pit organ and the terminal nerve masses (TNMs) are shown in semi-thin sections of the pit organs of (A) the crotaline snake *Gloydius blomhoffi* [from Goris et al. (2007)] and (B) the pythonid snake, *Python regius* [from Amemiya et al. (1996)]. In (A), the TNMs and capillaries are labeled directly. In (B), capillaries are denoted by asterisks and the arrows point to TNMs.
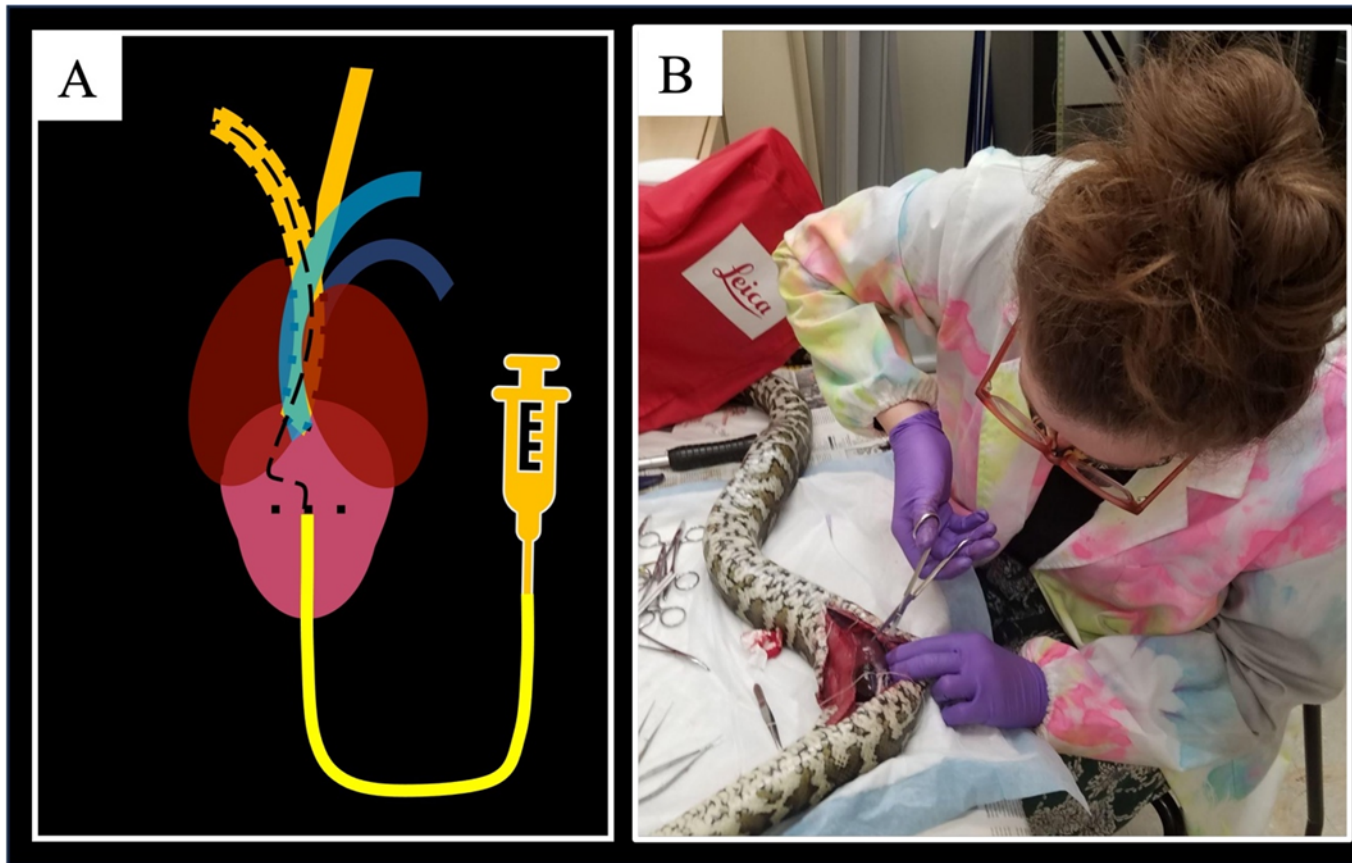
Fig. 4.4. Vascular casting procedure in snakes. (A) Diagram showing placement of the catheter (represented as a dashed black line) into the right aortic arch (orange) through an incision in the ventricle (pink). (B) Image of a vascular casting procedure in process, prior to exposure of the heart, in *Morelia spilota.*
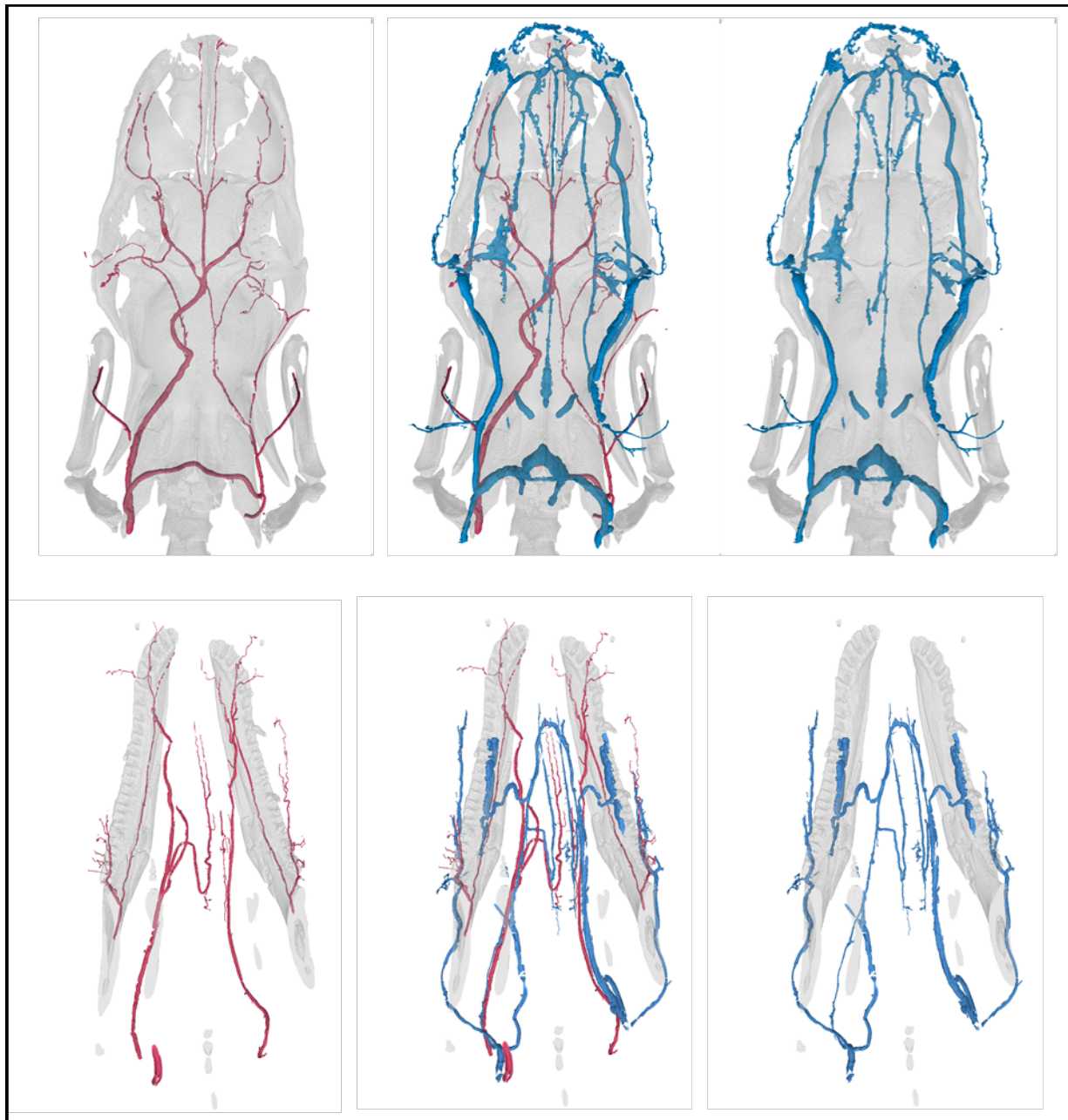
Fig. 4.5. Cephalic blood supply in *Antaresia childreni*. Top row depicts blood vessels of the upper jaw and braincase; bottom row depicts blood vessels of the lower jaw. Arteries are shown in red, veins in blue.
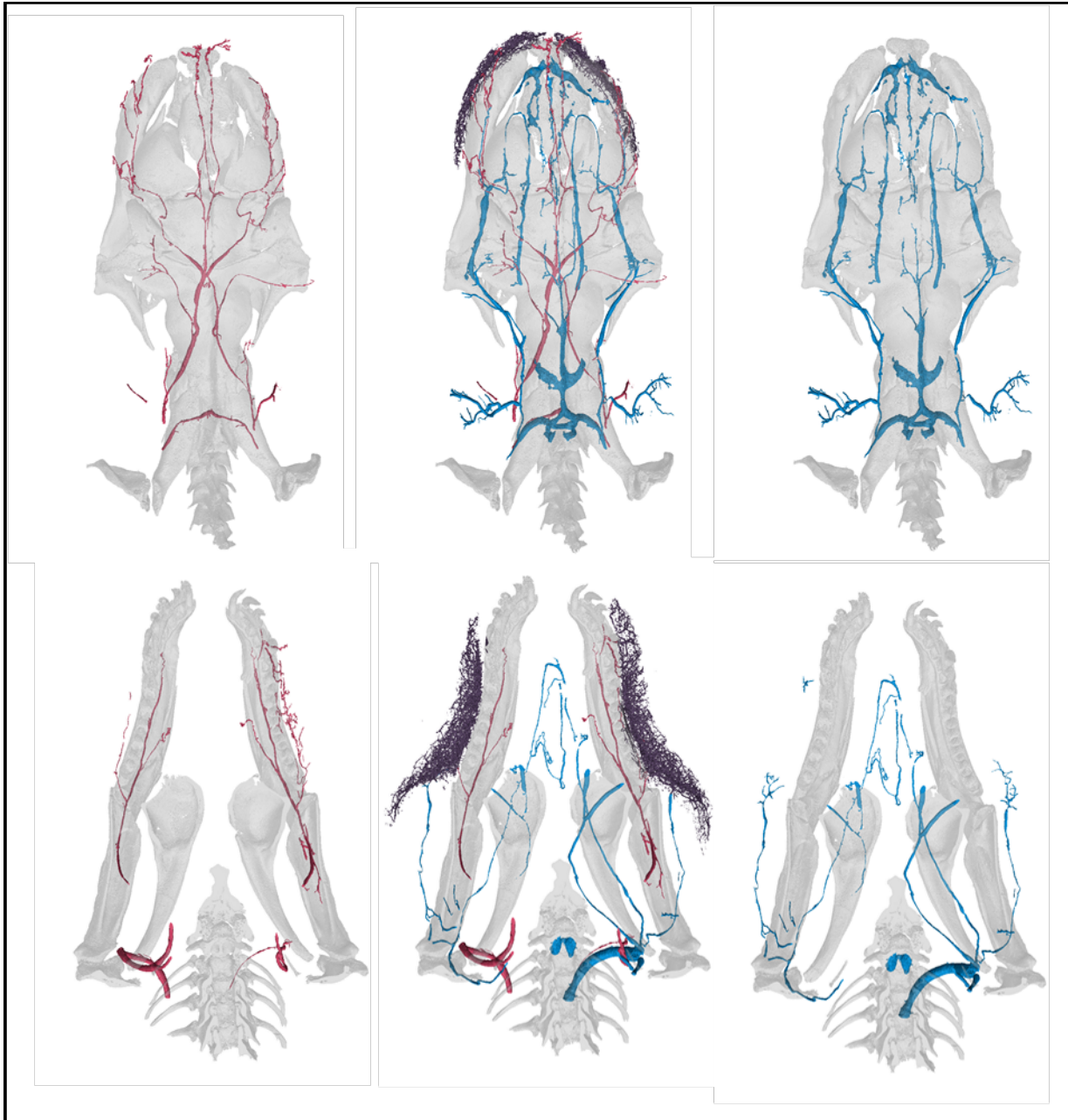
Fig. 4.6. Cephalic blood supply in *Morelia spilota*. Top row depicts blood vessels of the upper jaw and braincase; bottom row depicts blood vessels of the lower jaw. Arteries are shown in red, veins in blue
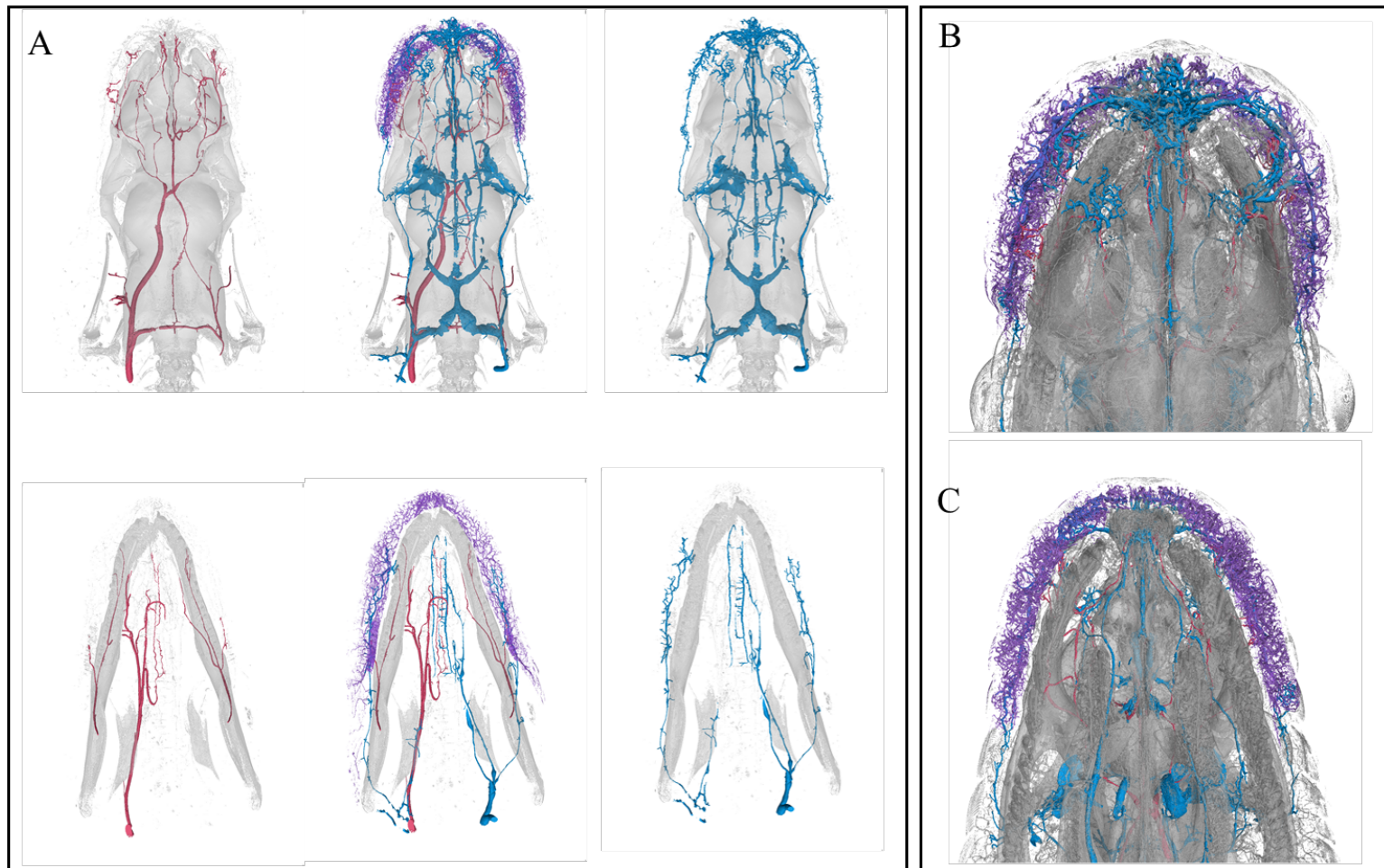
Fig. 4.7. (A) Cephalic blood supply patterns in *Python regius*. Top row depicts blood vessels of the upper jaw and braincase; bottom row depicts blood vessels of the lower jaw. Arteries are shown in red, veins in blue. The arrangement of arteries and veins relative to the dense vascular network surrounding the supralabial array (purple) is shown in dorsal (B) and ventral (C) views of the rostrum.
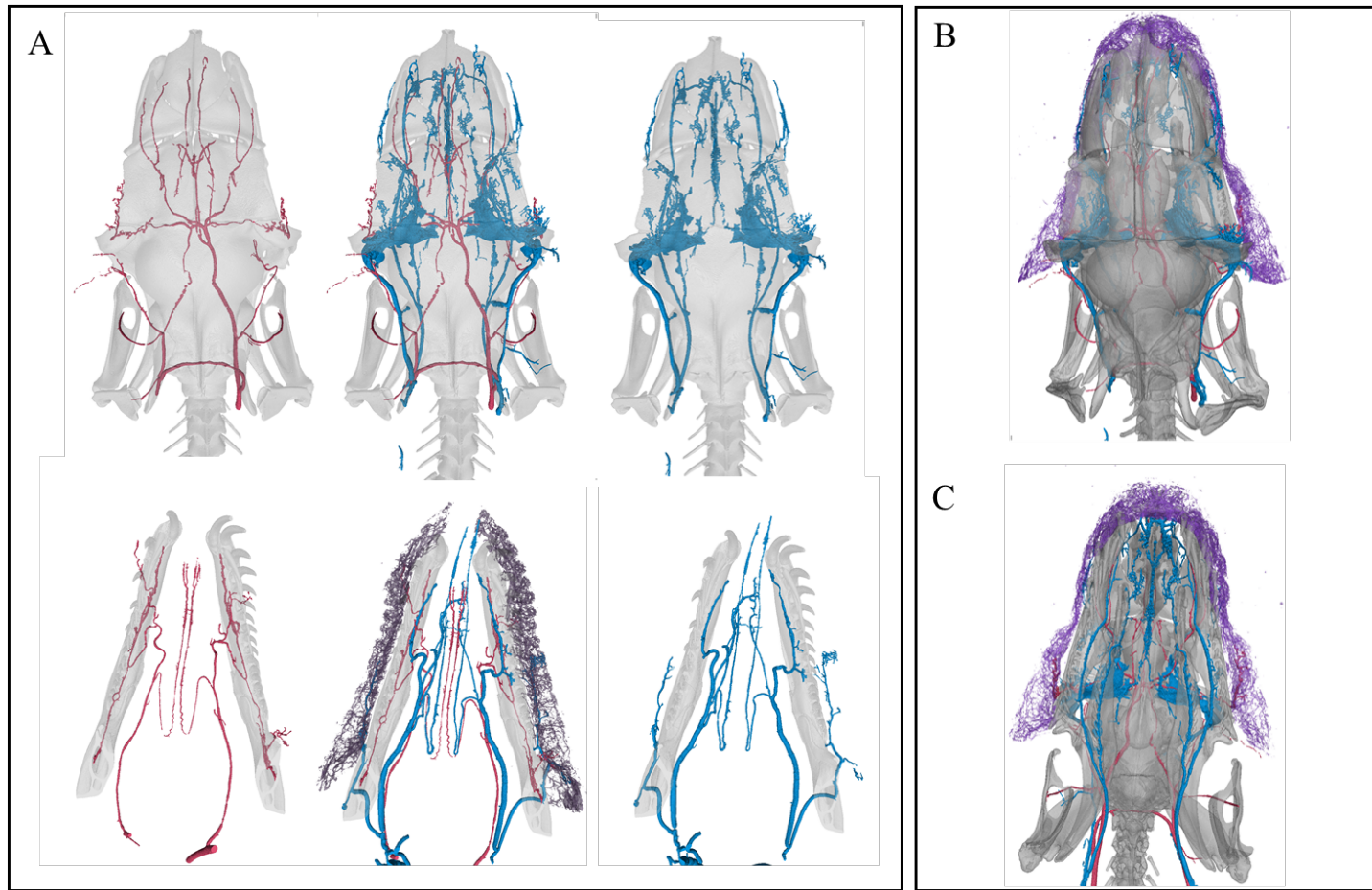
Fig. 4.8. (A) Cephalic blood supply in *Corallus hortulanus*. Top row depicts blood vessels of the upper jaw and braincase; bottom row depicts blood vessels of the lower jaw. Arteries are shown in red, veins in blue. The arrangement of arteries and veins relative to the dense vascular network surrounding the supralabial array and supralabial scales (purple) is shown in dorsal (B) and ventral (C) views of the upper region of the head.
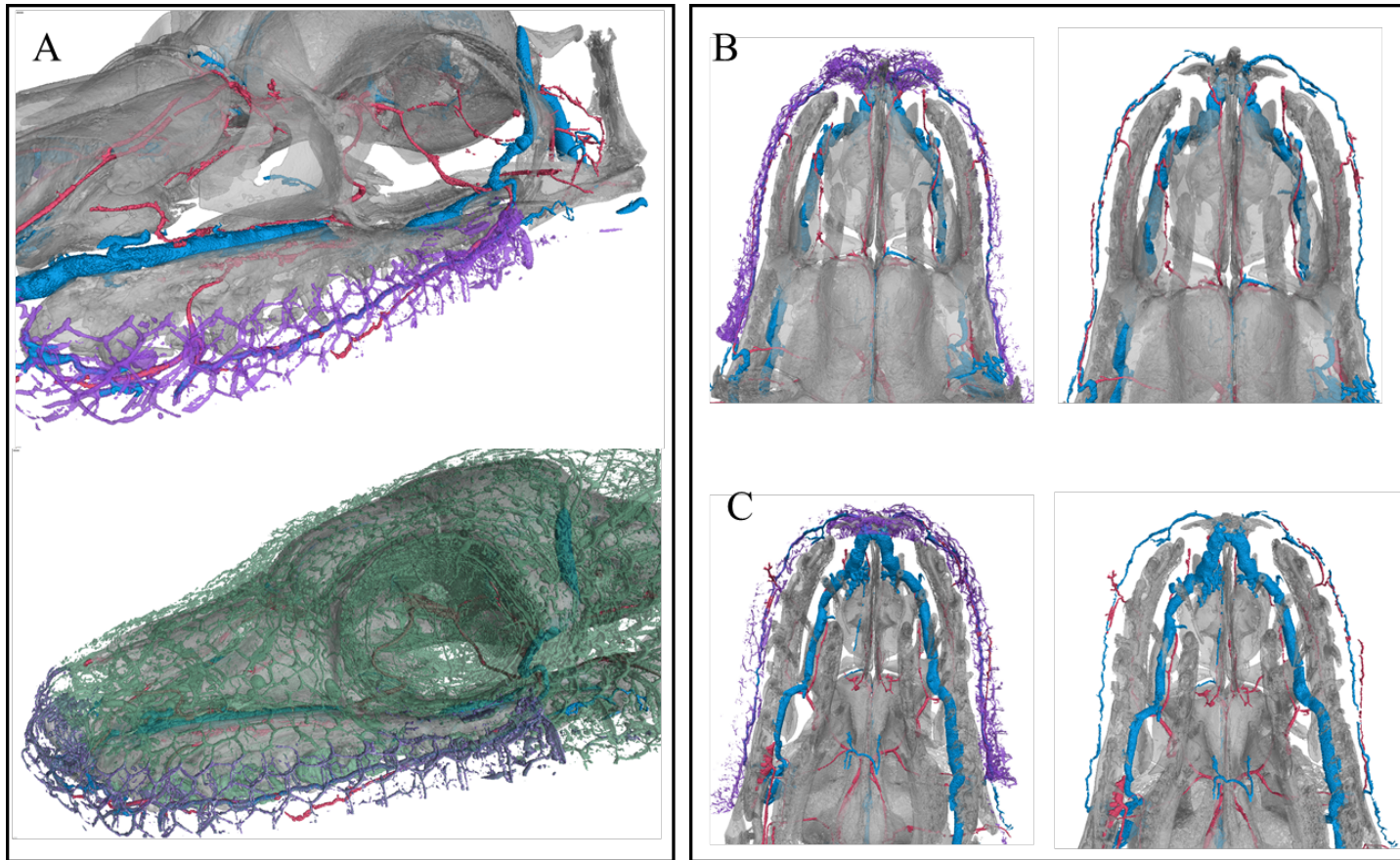
Fig. 4.9. Cephalic blood supply in the upper jaw of *Boa constrictor*. (A) Blood vessels of the upper jaw and braincase, showing the major vessels supplying and draining the supralabial scales (arteries in red, veins in blue). Vessels that form in the margins between scales are shown in purple for the supralabial scales and green for the other scales of the head. The arrangement of arteries and veins relative to the dense vascular network surrounding scales (purple) is shown in dorsal (B) and ventral (C) views of the upper region of the head
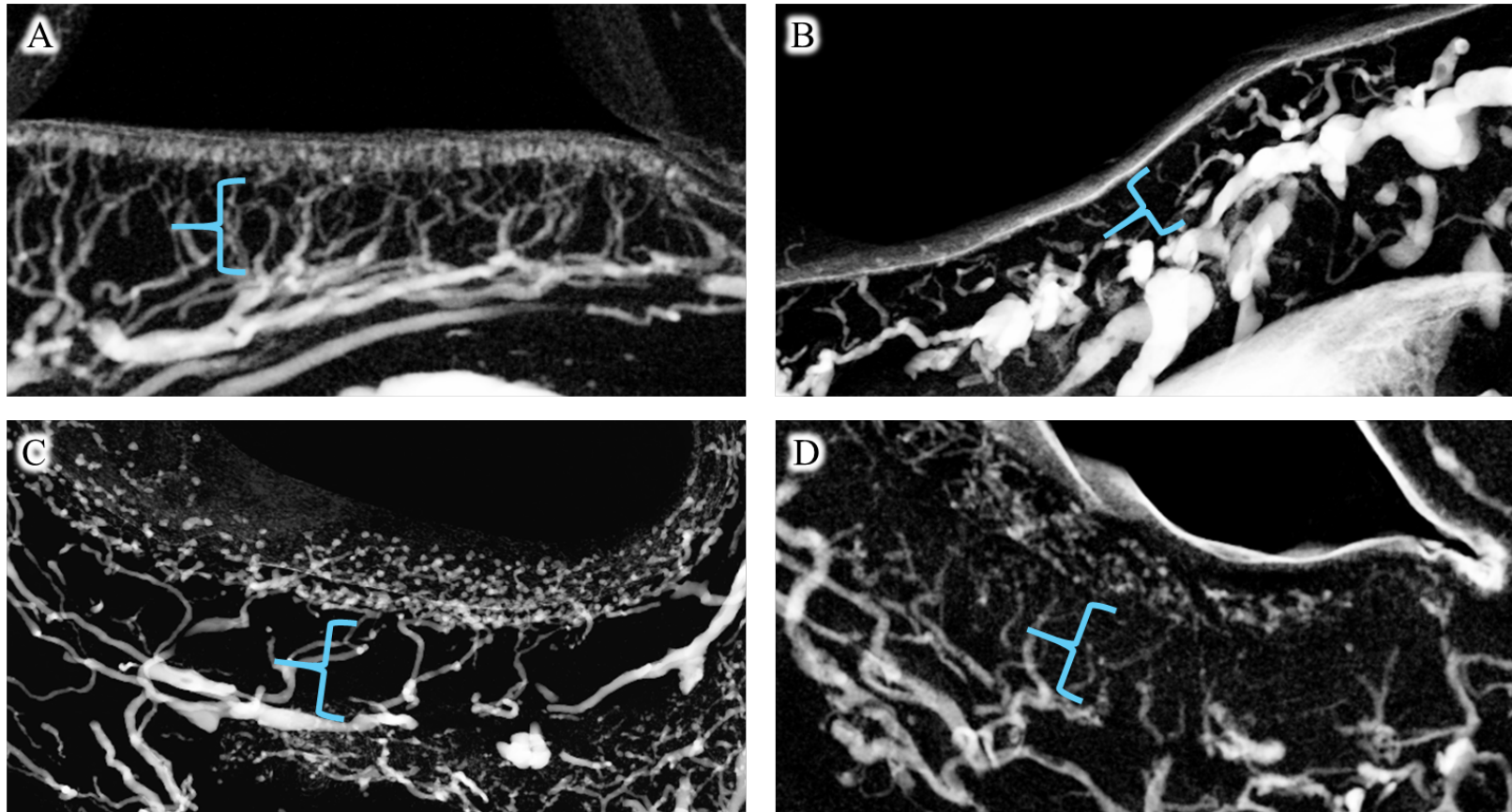
Fig. 4.10. Cross sections of the rostral pits of *P. regius* (A) and *M. spilota* (B), and one of the infralabial pits in *A. childreni* (C) and *C. hortulanus* (D). Blue brackets indicate the space between the layers of the major vessels and the capillary beds.
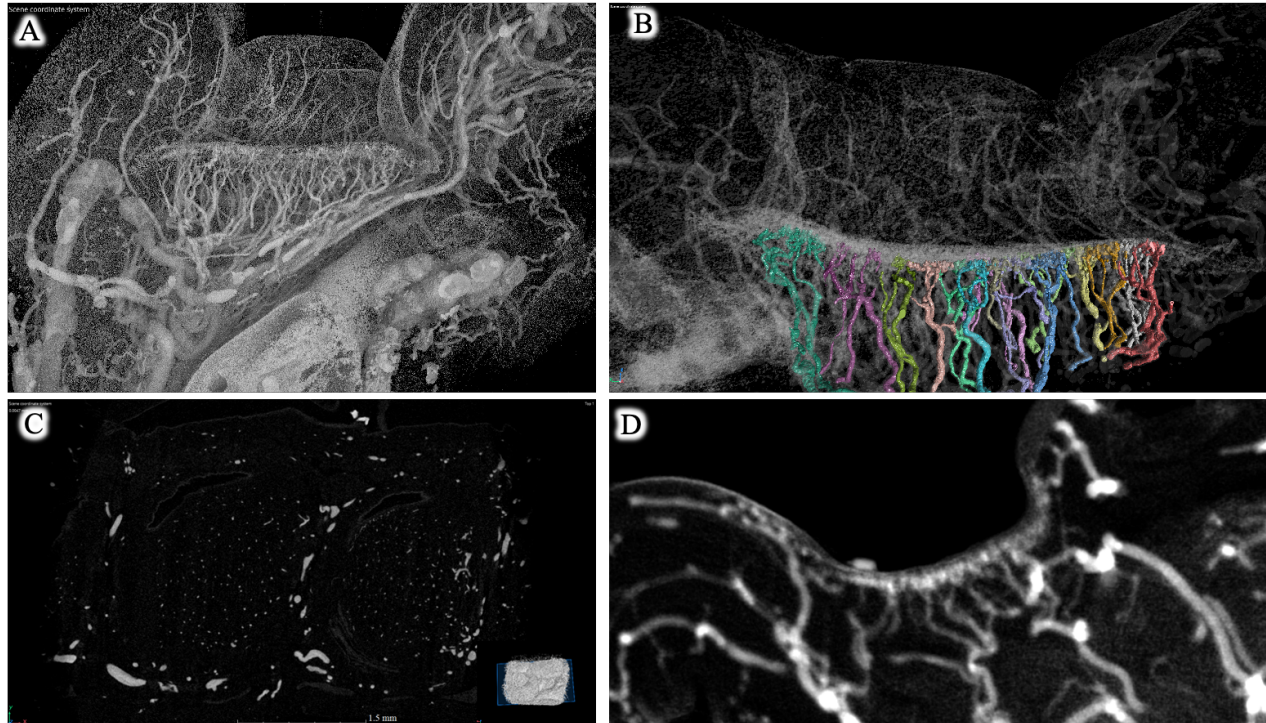
Fig. 4.11. The microvasculature of the pit organs in *Python regius* is arranged as a dense cluster of looping vessels that project perpendicularly to the pit fundus. (A) A cross-section taken from supralabial pit 1 showing the overall morphology of the vessels at the pit membrane, the arteries that supply it, the veins that drain it, and the relationship to the vessels of the scale within which it lies. (B) A single layer of individual capillary loops across the middle of the pit fundus, with each loop distinctively colored. (C) Slice taken from a microCT volume at the level of the pit fundus. White specks show the apices of individual capillary loops, and larger areas of white indicate the veins that drain the pit fundus. (D) The relatively sparse microvasculature of the infralabial pit array in *P. regius*.
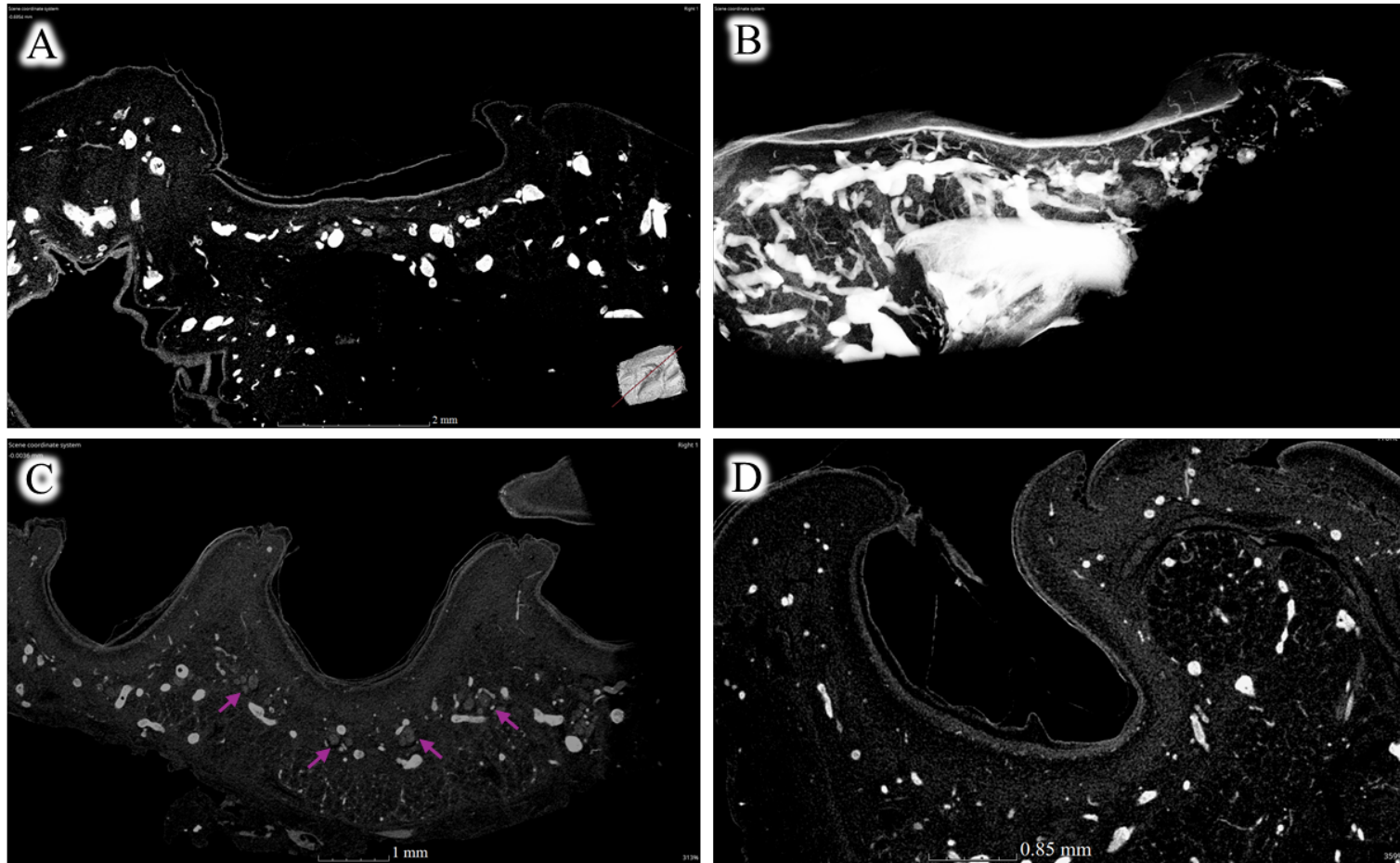
Fig 4.12. Some capillary loops appear to contact the pit membrane in both the supralabial (A, B) and infralabial (C, D) pit arrays of *Morelia spilota*. In the infralabial scale row, the arterioles terminating at these capillary beds travel alongside the sub-branches of V_3 (marked with arrows in C).
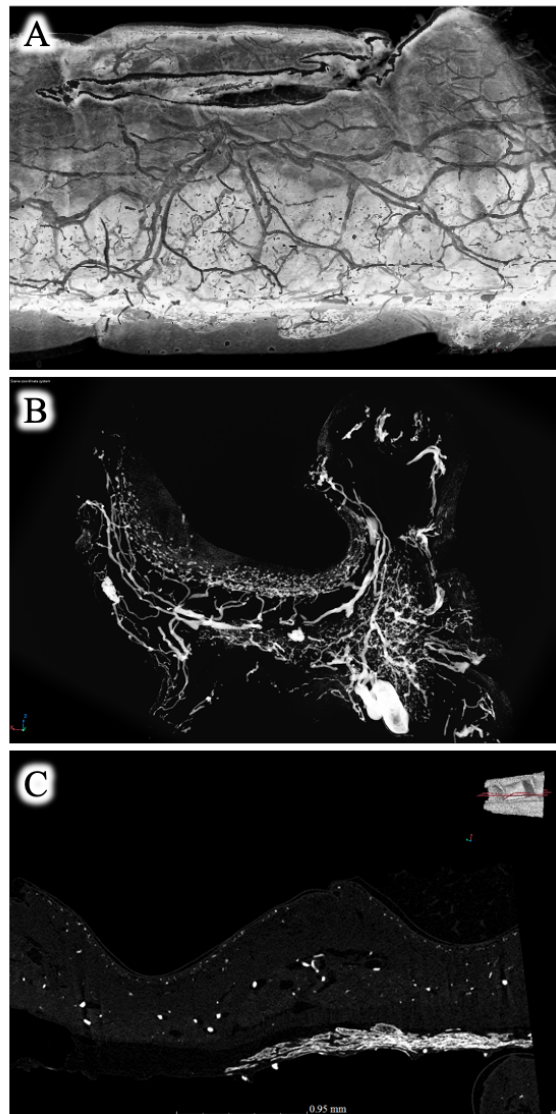
Fig. 4.13. Absence of supralabial pit organs in *Antaresia childreni* is reflected in a relatively less organized capillary network underlying the rostral and supralabial scales (A). The caudal infralabial pit arrays in this species are well developed and each consists of 3-5 pits. When segmented, a relatively flat layer of interconnected capillaries is seen to lie just below the fundus of each pit, apparently in contact with the pit membrane (B,C). The morphology of the capillary network differs from that of *P. regius* in that the loops do not project so strongly perpendicularly to the fundus, although a bulbous expansion at the apex of each loop is present (B)
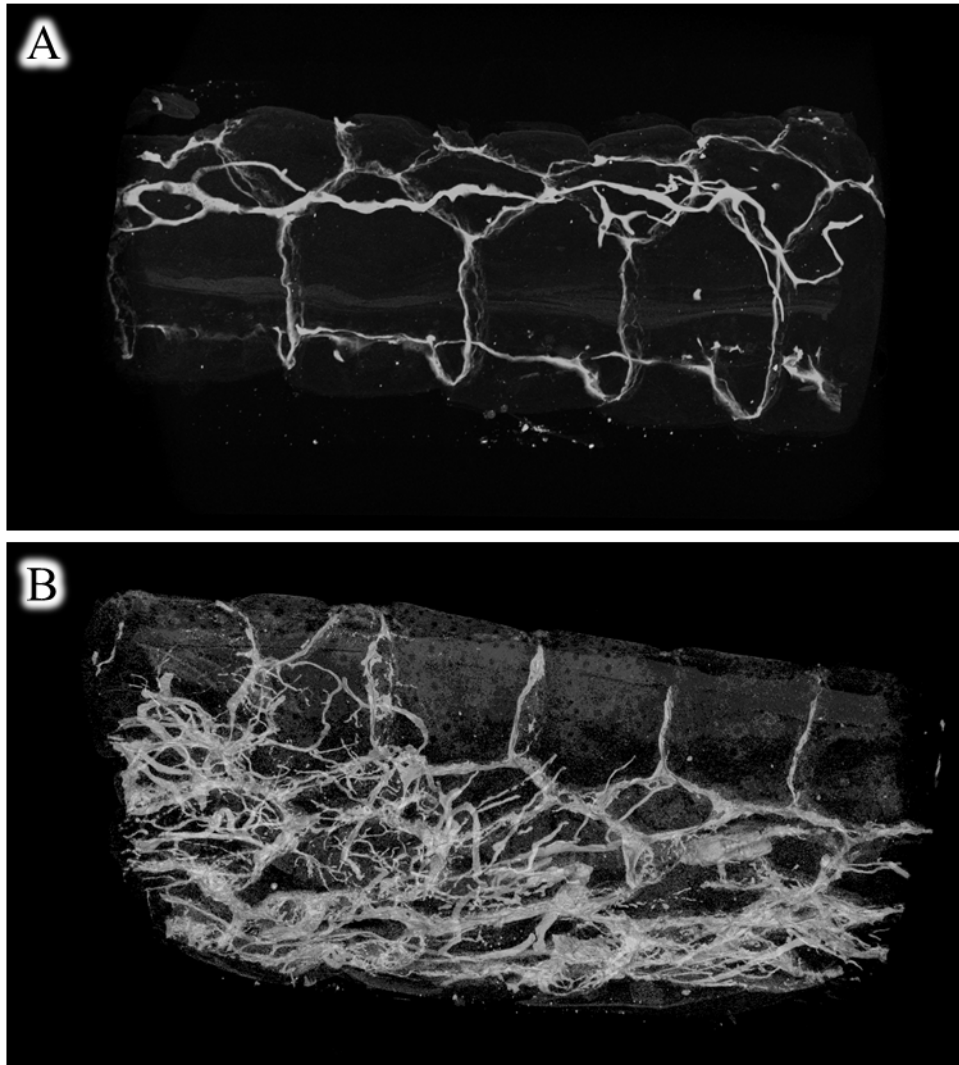
Fig. 4.14. The scales of the supralabial (A) and infralabial (B) scale rows of *Boa constrictor* are bracketed by small vessels, but no microvascular network underlying these scales was observed.
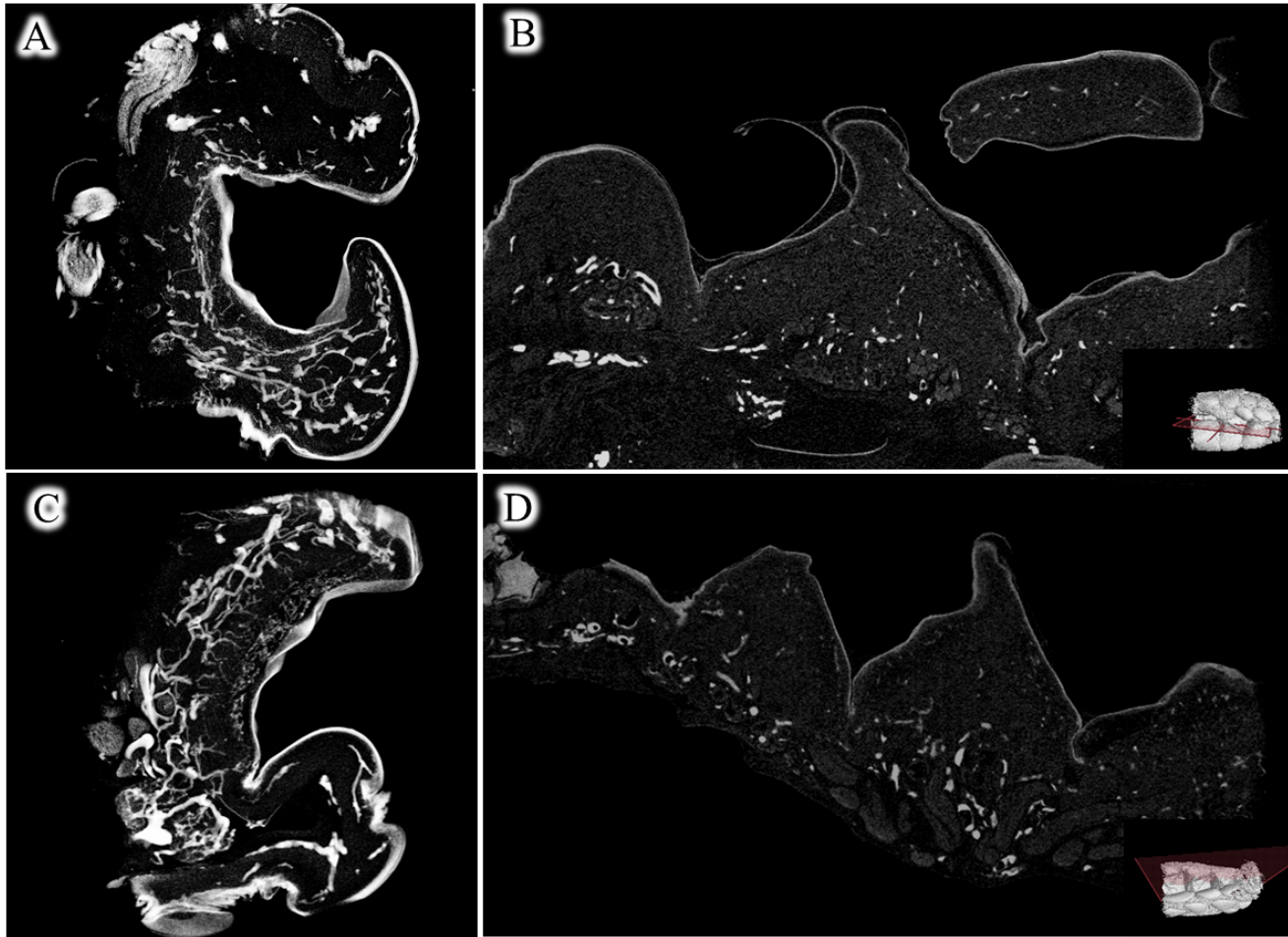
Fig. 4.15. The microvasculature of the pit organs of *Corallus hortulanus* is arranged in a dense cluster of looping vessels, which are associated with the regions of the scales comprising the supralabial (A, B) and infralabial (C, D) pit arrays where TNMs are reportedly present
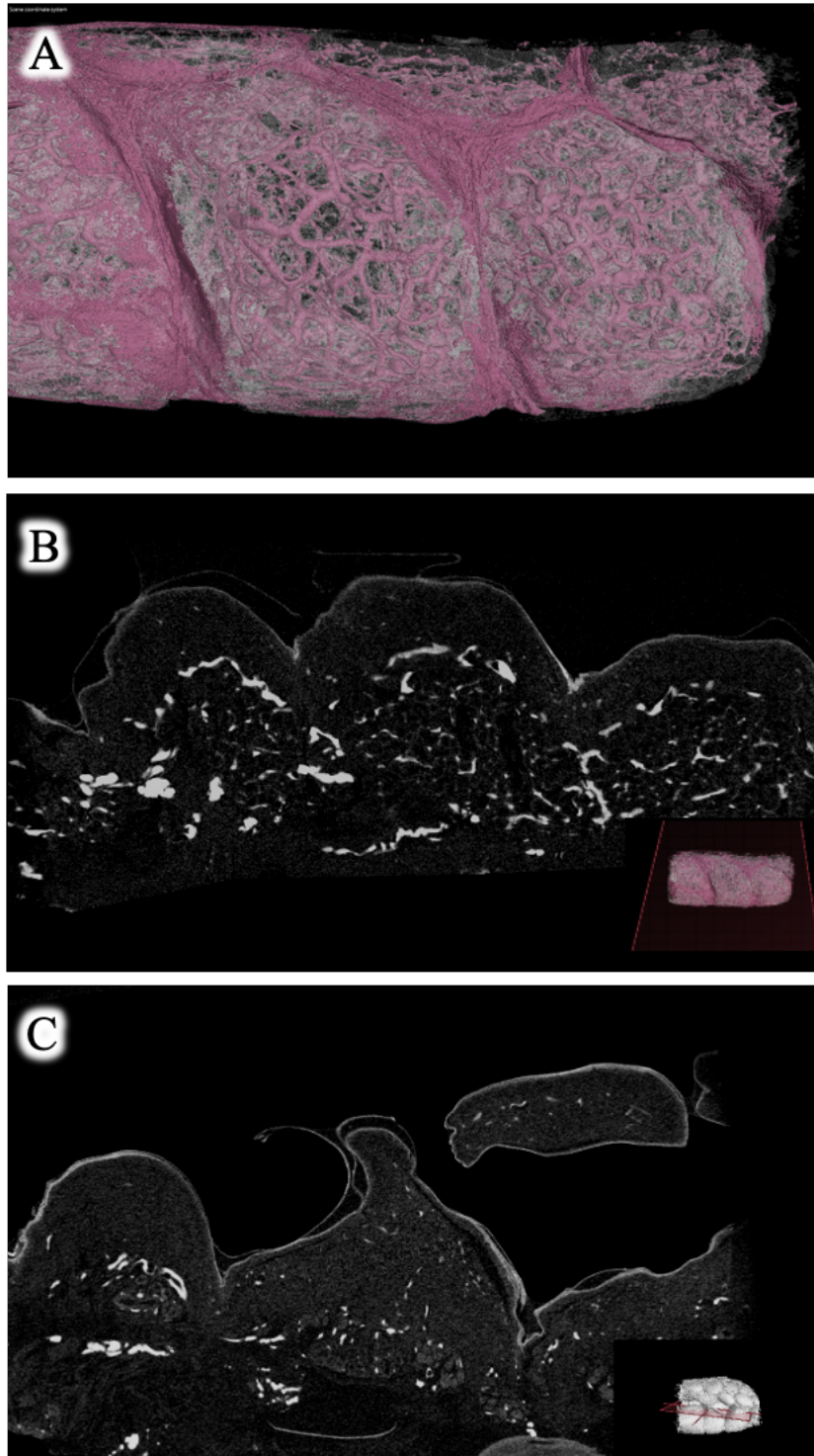
Fig. 4.16. Arrangement of vessels in the supralabial scales of *Corallus hortulanus* that lack pits (A, C) and those scales that are part of the supralabial pit array (B,D).
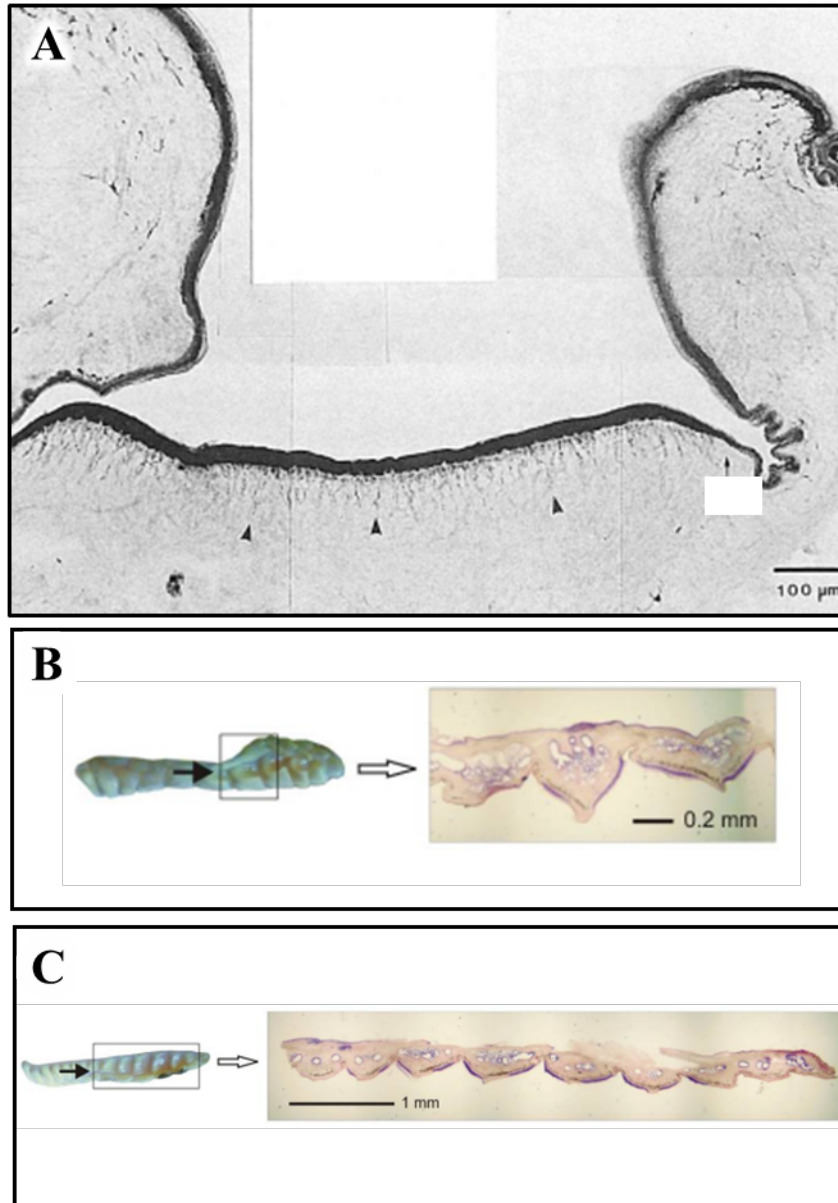
Fig. 4.17. Succinate dehydrogenase staining for mitochondria-rich TNMs shows the location of the TNMs in pits of *Python regius* (A) and *Corallus hortulanus* (B, C). (A) A cross section of a supralabial pit organ in *P. regius*, in which the dark staining of the pit fundus indicates presence of TNMs. Unmyelinated nerve fibers beneath the fundus are indicated by arrowheads [from Amemiya et al.(1996)]. Transverse sections of the supralabial (B) and infralabial (C) pit arrays in *C. hortulanus* show purple staining on the rostral and caudal margins of the scales, indicating regions where TNMs are located [from Ebert (2007)].

REFERENCES

Amemiya, F., R. C. Goris, Y. Atobe, N. Ishii, and T. Kusunoki. 1996. The ultrastructure of infrared receptors in a boid snake, Python regius: evidence for periodic regeneration of the terminals. Animal Eye Research (15): 13-25

Amemiya, F., M. Nakano, R.C. Goris,T. Kadota, Y. Atobe, K. Funakosh, and R. Kishida. 1999. Microvasculature of crotaline snake pit organs: possible function as a heat exchange mechanism. The Anatomical Record: An Official Publication of the American Association of Anatomists, 254: 107-115.

Bakken, G. S., and A. R. Krochmal. 2007. The imaging properties and sensitivity of the facial pits of pitvipers as determined by optical and heat-transfer analysis. Journal of Experimental Biology, 210(16): 2801-2810.

Bakken, G. S., S. E. Colayori, T. Duong. 2012. Analytical methods for the geometric optics of thermal vision illustrated with four species of pitvipers. Journal of Experimental Biology, 215(15): 2621-2629.

Bruner, H. L. (1907). On the cephalic veins and sinuses of reptiles: With description of a mechanism for raising the venous blood-pressure in the head. Amer. Jour. of Anatomy.

Bullock, T. H., and F. P. J. Diecke. 1956. Properties of an infra-red receptor. The Journal of Physiology, 134(1): 47-87.

Cadena, V., Andrade, D. V., Bovo, R. P., & Tattersall, G. J. (2013). Evaporative respiratory cooling augments pit organ thermal detection in rattlesnakes. Journal of Comparative Physiology A, 199, 1093-1104.

de Cock Buning, T. 1985. Qualitative and quantitative explanation of the forms of heat sensitive organs in snakes. In G.G. Zweers and P. Dullemeijer (Eds.), Architecture in Living Structure (pp. 87-99). Springer, Dordrecht.

de Cock Buning, T., Terashima, S. I., & Goris, R. C. (1981). Crotaline pit organs analyzed as warm receptors. Cellular and Molecular Neurobiology, 1, 69-85.

Ebert, J. (2007). Infrared sense in snakes–behavioural and anatomical examinations (Crotalus atrox, Python regius, Corallus hortulanus) (Doctoral dissertation, Ph. D. Thesis).

Ebert, J., S. Müller, and G. Westhoff. 2007. Behavioural examination of the infrared sensitivity of ball pythons. Journal of Zoology, 272(3): 340-347.

Enok, S., Leite, G. S., Leite, C. A., Gesser, H., Hedrick, M. S., & Wang, T. (2016). Improved cardiac filling facilitates the postprandial elevation of stroke volume in Python regius. Journal of Experimental Biology, 219(19), 3009-3018.

Goris, R. C., Y. Atobe, M. Nakano, T. Hisajima, K. Funakoshi, and T. Kadota. 2003. The microvasculature of python pit organs: morphology and blood flow microkinetics. Microvascular Research, 65(3): 179-185.

Goris, R. C., Y. Atobe, M. Nakano, K. Funakoshi, and K. Terada. 2007. Blood flow in snake infrared organs: response-induced changes in individual vessels. Microcirculation, 14(2): 99-110.

Hensel, H. (1975). Static and dynamic activity of warm receptors in Boa constrictor. Pflügers Archiv, 353(3), 191-199.

Kluge, A. G. (1993). Aspidites and the phylogeny of pythonine snakes. Records of the Australian Museum Supplement, 19, 1-77.

Molenaar, G. J. 1992. Anatomy and physiology of infrared sensitivity of snakes. In C. Gans and T.S. Parsons (Eds.), Biology of the Reptilia (Vol. 17, pp. 367-453). Academic Press, London and New York.

Nakano, M., Y. Atobe, R. C. Goris, F. Yazama, M. Ono, H. Sawada, and R. Kishida. 2000. Ultrastructure of the capillary pericytes and the expression of smooth muscle α-actin and desmin in the snake infrared sensory organs. The Anatomical Record: An Official Publication of the American Association of Anatomists, 260(3): 299-307.

Porter, W. R., and Witmer, L. M. (2015). Vascular patterns in iguanas and other squamates: blood vessels and sites of thermal exchange. PLoS One, 10(10), e0139215.

Terashima, S. I., Goris, R. C., & Katsuki, Y. (1970). Structure of warm fiber terminals in the pit membrane of vipers. Journal of Ultrastructure Research, 31(5-6), 494-506.

Von Bourgondien, T. M., and Bothner, R. C. (1969). A comparative study of the arterial systems of some New World Crotalinae (Reptilia: Ophidia). American Midland Naturalist, 107-147.

CHAPTER 5
CONCLUSIONS

The capacity for infrared-imaging evolved independently in three clades of snakes: boas, pythons, and pitvipers. Although the morphology of the crotaline IR-imaging system has received considerable attention, and to a lesser extent so has their development, few previous works have addressed the detailed morphology of this system in pythons or boas, and only one previous study has been done on the development of this system in pythons. The preceding three chapters collectively describe the morphology of elements critical to the function of the infrared-imaging systems of boas and pythons — specifically, the blood vessels that supply and drain the pit membranes and the nerves that innervate them — and the development of this sensory system in pythons.

The first research chapter of this dissertation provides a description of the embryonic development of the IR-imaging system in three species of pythons: *Antaresia childreni*, *Python molurus*, and *P.regius*. I combined observations of traditional histological material and microCT scans to assess interspecific variation in the developmental timing of structures associated with IR-imaging, including the pit organs, trigeminal nerve rami, and the optic tectum. *Python molurus* and *P. regius* both possess several large pit organs in their supralabial arrays and only a few shallow pits in their infralabial arrays. Conversely, *Antaresia childreni* lacks supralabial pits entirely, but possesses a well-defined series of infralabial pits. In *P. molurus* and *P. regius*, the invagination of the rostral and supralabial pits is evident as early as the day of oviposition (day 0 post-oviposition), well before these pits are contacted by sub-branches of the two trigeminal rami (V_1 or V_2) that ultimately innervate them. However, in all three taxa examined, V_3 reaches the peripheral tissues of the lower jaw prior to any evidence of pit formation. Although the pit organs of the upper jaw form individually in a rostral-to-caudal sequence, those in the lower jaw are first

evident as a longitudinal fold, from which the infralabial pits later differentiate. This suggests a decoupling of development between the pits in the supra- and infralabial arrays. Additionally, the post-ovipositional developmental periods of *P. molurus* and *P. regius* are substantially longer than that of *A. childreni*, and they spend more time in each stage of post-ovipositional embryonic development. Considering that the supralabial pits continue to develop through hatching, I hypothesize that their development may be related to the longer developmental periods in those taxa that possess them.

In my second research chapter, I used diffusible iodine contrast-enhanced microCT (diceCT) to compare patterns of innervation of the pits and labial scales in four pythons (*A. childreni, Morelia spilota, P. bivittatatus,* and *P. regius)* and two boas (*Corallus hortulanus* and *Boa constrictor*). I found substantial intra- and interfamilial variation in innervation of the pit organs, particularly that of the maxillary nerve, which exhibits extensive sub-branching, which has not been previously reported. Additionally, I found that some individual pit organs are simultaneously innervated by multiple sub-branches of a given trigeminal ramus, suggesting a more complex spatiotopic mapping of infrared information in the central processing centers of the brain than previously believed.

One unexpected and important finding reported in the second research chapter is the discovery of "pit organs" in *Boa constrictor*—a species that had previously been thought to lack pit organs entirely. MicroCT renderings of the heads of *B. constrictor* revealed shallow depressions on the caudal margins of some scales in both the supra- and infralabial scale rows — i.e., in regions where IR-sensitive tissues are reportedly present in this species. These depressions may have been overlooked in previous studies of IR-imaging in *B. constrictor*, as they are generally obscured by scale texture and pattern, neither of which are observed in microCT volume renderings. It is not clear whether the small labial depressions of *Boa constrictor* represent rudimentary or vestigial pit organs. *Boa constrictor* is the sister group to all of the New

World boas that possess pit organs (e.g., those in the genera *Corallus* and *Epicrates*). *Sanzinia madagascariensis*, the Malagasy tree boa, also possesses pit organs, though it lies outside of the New World clade along with all other boas (e.g., *Acrantophis*, *Eryx*, *Charina*, etc.) that lack pit organs. While taxon sampling has been far from complete, all boas examined in previous studies have demonstrated response to thermal stimulation of their labial scales, independent of whether they possess obvious pit organs. These reports coupled with the presence of rudimentary or vestigial pits in *Boa constrictor* may indicate repeated loss and re-evolution of pit organs within the boid lineage.

The third and final research chapter combined vascular casting with microCT to compare patterns of blood supply to the pit organs and labial scales in three pythons (*A. childreni, Morelia spilota,* and *P. regius)* and two boas (*C. hortulanus* and *B. constrictor*). Studies of the overall pattern of cephalic arterial supply and veinous drainage are limited, so I first described the major vessels in the heads of those taxa. Interfamilial differences in cephalic vascular patterns were observed, and intrafamilial differences in those patterns were associated with the presence or absence of pits in the supralabial array. However, the major vessels supplying and draining the pits are largely consistent between taxa.

The microvasculature underlying the pit organs is highly complex in *P. regius*, and the looping arrangement of capillaries observed in microCT scans of the rostral and supralabial pits is consistent with previous studies based on scanning electron microscopy of vascular corrosion casts. Similar (though substantially less dense) arrangements of vessels are present in the supra- and infralabial pits of *M. spilota* and *C. hortulanus* and in the infralabial pits of *A. childreni*. The occurrence of this microvascular pattern in the independently evolved pit organs of the Boidae and Pythonidae suggests that the developmental processes involved in pit organ formation are either conserved or there is a strong functional component to the microvascular pattern, that has evolved independently in both groups alongside the independent evolution of pit organs.

My research adds to our collective understanding of the IR-imaging system of boid and pythonid snakes, providing novel anatomical observations and development insights. The advent of X-ray microcomputed tomography as a tool for anatomical research allowed me to study this system *in situ* for the first time, a feat that has only recently become possible.

APPENDICES

Appendix A: Formula for 10% Phosphate Buffered Formalin

Materials

- 4 g Sodium dihydrogen phosphate, monohydrate ($NaH_2PO_4 \bullet H_2O$)

- 6.5 g Disodium hydrogen phosphate, anhydrous (Na_2HPO_4)

- 100mL 38% Formaldehyde stock solution

- 900 mL Deionized water (DI H2O)

Steps

1. Under a fumehood, combine 900 mL DI H2O and 100 mL of 38% formaldehyde in an Erlenmeyer flask.

2. Add a stir bar and place on a stir plate set to medium speed.

3. Measure 4 g of $NaH_2PO_4 \bullet H_2O$

4. Measure 6.5 g of Na_2HPO_4

5. Add both to the formaldehyde solution.

6. Allow salts to mix until combined.

Appendix B: Formula for 0.3% PTA in 70% EtOH (per Metscher, 2011)

Materials

- 0.5 g crystalline phosphotungstic acid (PTA)

- 50 mL Deionized water (DI H_2O)

- 35 mL absolute ethanol (100% EtOH)

Steps

1. Combine 0.5g of PTA with 50 mL DI H2O to generate a 1% (w/v) solution.

2. Agitate for 10-15 minutes at room temperature.

3. Add 15 mL of 1% PTA solution to 35 mL of absolute EtOH to generate 0.3% PTA in 70% EtOH.

Store at room temperature protected from light. Both 1% PTA and 0.3% PTA in 70% EtOH keep indefinitely at room temperature.

Appendix C: Formula for 1.25% Lugol's Solution (per Callahan et al., 2021)

Materials

- 12.5 g iodine

- 25 g potassium iodine

- 1 L Deionized water (DI H_2O)

Steps

1. Fill a container with 1.0 L of DI water.

2. Measure 12.5 g of iodine crystals.

3. Measure 25 g of potassium iodine crystals.

4. Mix the crystals into the DI H_2O.

5. Shake the container well.

6. Add a mixing tab into the container.

7. Place mixture filled container onto mixing platform - set to maximum.

8. Allow to mix for up to 48 h.

Mix and store in a dark location. Prepare as needed.

Helen Bond Plylar, Ph.D.
Curriculum Vitae

PROFESSIONAL PREPARATION

Utah State University, Logan, UT	Biology (Ecology)	Ph.D.	(2024)
Florida Institute of Technology	Biological Sciences	Ph.D.	(transferred to USU)
Southeastern Louisiana University	Biological Sciences	M.S.	(2015)
Southeastern Louisiana University	Biological Sciences	B.S.	(2013)

APPOINTMENTS
2025-2028: NSF Postdoctoral Fellow, UF, Gainesville, FL
2024: Postdoctoral Researcher, UNCG, Greensboro, NC
2022-2024: Lab Manager, MicroCT Facility, USU, Logan, UT
2022 (fall): Graduate Instructor, USU Logan, UT
2018–2022: Graduate Teaching Assistant, USU, Logan, UT
2017–2018: Graduate Teaching Assistant, FIT, Melbourne, FL
2016 (fall): Graduate Research Assistant, FIT, Melbourne, FL
2015–2018: Terrestrial Animal Lab Manager, FIT, Melbourne, FL
2014–2015: Graduate Teaching Fellow, SELU, Hammond, LA
2013–2014: Graduate Teaching Assistant, SELU, Hammond, LA
2011–2013: Anatomy and Physiology Assistant, SELU, Hammond, LA

PUBLICATIONS
Plylar, H.B., B.I. Crother. C.L. Fontenot. (2024). Ontogenetic Eye-body Allometry in Two Sympatric Natricine Snakes, *Nerodia cyclopion* and *N. fasciata. Ichthyology and Herpetology 112:*1, 1-9.

Kepas, M., S.B. Hudson, E.E. Virgin, **H.B. Plylar**, S.S. French, A.H. Savitzky. (2023). Stage-dependent corticosterone production and response to maternal toxin exposure in embryos of a viviparous and genetically toad toxin-resistant snake (*Thamnophis elegans*)*. Ichthyology and Herpetology 111:*4, 543-548.

Godwin, C.D., **H.B. Plylar** (2020). Geographic distribution*: Storeria maculata* (Red-bellied snake). *Herpetological Review*. 51(4): 784.

Godwin, C.D., **H.B. Plylar** (2020). Geographic distribution: *Chrysemys picta* (Painted turtle). *Herpetological Review*. 51(4): 771.

Plylar, H.B., Godwin, C.D. (2020) Geographic distribution: *Agkistrodon contortrix* (Southern Copperhead). *Herpetological Review*. 51(4): 780.

MANUSCRIPTS SUBMITTED OR IN PREPARATION
Kepas, M., **H.B. Plylar**, C.D. Godwin, E.E. Virgin, S.S. French, A.H. Savitzky. A Field Evaluation of Adrenal Sufficiency in a Toad-Eating Species (Heterodon Platirhinos) With Profound Adrenal Enlargement. [submitted to Herpetological Conservation and Biology, 2024]

Fukuda, M., J. Shi, **H.B. Plylar**, T. Inoue, Q. Chen, N. Mori, A.H. Savitzky, A. Mori. Comparison of feeding morphology in association with diet and toxin inAsian Natricine snakes (genus Rhabdophis) [in preparation, 2024]

CONFERENCE PRESENTATIONS

Plylar, H.B., A.H. Savitzky (2023, July). Trigeminal Innervation and Blood Supply to Boid and Pythonid Pit Organs. Oral presentation given at the Joint Meeting of Ichthyologists and Herpetologists in Norfolk, VA.

Savitzky, A.H., **H.B. Plylar**, Yamamoto, M. Toda (2023, July). Observations on the Soft Tissues and Vasculature of Sea Snakes (Hydrophiinae). Oral presentation given at the Joint Meeting of Ichthyologists and Herpetologists in Norfolk, VA.

Craige, L., A. H. Savitzky, **H.B Plylar** (2023, July) Hypothesized Morphological Correlates of Slug-eating in Contia, Compared with Related Dipsadine Snakes. Poster presentation given at the Joint Meeting of Ichthyologists and Herpetologists in Norfolk, VA.

Savitzy, A.H., **H.B. Plylar**, A. Mori, M. Toda (2022, November). Anatomical and Developmental Studies of Amphibians and Reptiles Facilitated by Contrast-enhanced Microcomputed Tomography. Oral presentation given at the annual meeting of the Herpetological Society of Japan in Okinawa, Japan.

Plylar, H.B., D. Hutchinson, A. Mori, A.H. Savitzky (2021, July). The Vascular Supply to the Parotoid Glands and of the Japanese Toad, Bufo Japonicus (Bufonidae). Poster presentation given at the Joint Meeting of Ichthyologists and Herpetologists in Phoenix, AZ.

Fontenot, C.L., S. Ferguson, **H.B. Plylar**, (2018, July). Comparison of the Role of Spectacle/Cornea Curvature in Vision Among Colubrid Snakes From Southeastern Louisiana. Oral presentation given at the Joint Meeting of Ichthyologists and Herpetologists in Rochester, NY.

Plylar, H.B., C.L. Fontenot (2016, July). Eye:Body Allometry and Scaling: Do Small Snakes Really Have Big Eyes? Oral presentation given at the Joint Meeting of Ichthyologists and Herpetologists in New Orleans, LA.

Plylar, H.B., C.L. Fontenot (2015, July). Shining a Light On Snake Eyes: A Photorefractive Study of Accommodation in Snakes. Oral presentation given at the Joint Meeting of Ichthyologists and Herpetologists in Reno, NV.

Plylar, H.B., C.L. Fontenot (2014, August). Refractive State and Visual Accommodation in Semiaquatic Colubrid Snakes. Poster presented at the Joint Meeting of Ichthyologists and Herpetologists in Chattanooga, TN.

GRANTS AND AWARDS

- NSF Postdoctoral Research Fellowship in Biology, recommended for funding
- 2024 Doctoral Research Student of the Year for the USU College of Science
- 2024 Doctoral Research Student of the Year for the USU Department of Biology
- USU Biology Department Matthew Del Grosso Endowed Scholarship (Awarded, 2023)
- University of the Ryukyus Tropical Biosphere Research Center Collaborative Opportunities Fellowship (Awarded, 2023)
- USU Graduate Research and Creative Opportunities Grant (Awarded, 2023)
- USU Biology Department Joseph E. Greaves Endowed Scholarship (Awarded, 2022)
- SSAR Roger Conant Grant in Herpetology (Awarded, 2021)
- Herpetologist's League E.E. Williams Research Award (Awarded, 2021)
- USU Ecology Center Graduate Student Research Award (Awarded 2020 & 2021)
- Smithsonian Institutional Fellowship Program (Honorable Mention, 2020)
- Society for Integrative and Comparative Biology Grants in Aid of Research (Awarded, 2015)

SYNERGISTIC ACTIVITIES

University, College, and Departmental Service

- USU Biology Department Diversity, Equity, and Inclusion Committee, Graduate Student Representative (2022-present)
- USU Student Association Graduate Director & Graduate Student Council President (2019-2020)
- College of Science Representative, USU Graduate Student Council (2019-2020)
- USU College of Science Graduate Student Council Chair (2020)
- USU College of Science Graduate Student Council Biology Representative (2019)
- USU Biology Graduate Student Association Vice President (2019)
- FIT Biology Graduate Student Association Co-Chair (2016-2017)
- SELU Biology Graduate Student Organization Secretary (2014-2015)

Professional Society Membership & Service

- American Society of Ichthyologists & Herpetologists (2014-present)
- Society for the Study of Amphibians and Reptiles (2014-present)
- Herpetologist's League (2014-present)
- ASIH Board of Governors (Governor, class of 2026)
- ASIH Executive Committee (Graduate Student Chair, 2022)
- ASIH Long Range Planning and Policy Committee (2022-2023)
- ASIH Committee on Student Participation Chair (2022)
- ASIH CoSP, Chair-elect (2020-2021)
- ASIH CoSP Secretary (2016, 2017, 2018)

- ASIH Book Raffle Committee (2019, 2023)
- ASIH Workshop Committee (2015, 2016, 2019)

Mentorship

- Gabriella Cale; USU URCO recipient, project investigating the blood supply to the adrenal glands of toad-eating Natricine snakes (*Thamnophis elegans* and *Rhabdophis tigrinus).*
- MicroCT scan segmentation and analysis (USU—undergraduate student: Emily Plant, 2021-2022; graduate student: Lauren Craige, 2022)
- Histological methods and image acquisition (USU—undergraduate students: Emily Plant, Gabriella Cale, from 2021-present)
-

PROFESSIONAL EXPERIENCE & SKILLS

Teaching Experience

- Ecology Lab (USU; GTA Fall 2021, Instructor Fall 2022)
- Herpetology (USU; Spring 2021, 2022)
- Evolution (USU; Fall 2020)
- Biology I Lab (USU; Fall 2019)
- Human Anatomy Lab (USU; Spring 2019 & 2020, Summer 2020, 2021, 2022, 2023, 2024)
- Animal Behavior Lab (USU; Fall 2018)
- Plant Physiology Lab (FIT; Spring 2018)
- Comparative Anatomy Lab (FIT; Fall 2017)
- Introductory Biology Lab (SELU; 2013-2015)

Field Work Experience

- Seasnake field collection (University of the Ryukus; Okinawa, Japan; September 2023)
- *Rhabdophid tigrinus* field collection (Kyoto University; Kyoto, Japan; April 2023)
- Phrynosoma field collection (Canyonlands Research Center, Monticello, UT, USA; Summer 2022)
- Hognose snake sampling (New York, USA; Spring 2021)
- Snake fungal disease sampling project, field technician (Middle Tennessee State University; Summer 2019)
- *Varanus giganteus* monitoring project, field technician (Northern Territory, Australia; December 2019-January 2020)
- Long-term monitoring of herpetofaunal road mortality
- Field collection of Natricine snakes for M.S. thesis research

Laboratory & Technical Skills

- Histology – traditional histology, immunohistochemistry
- Microscopy – SEM, TEM, fluorescence, confocal
- MicroCT volume analysis– 3D Slicer, Dragonfly ORS, VG Studio
- Statistics – R, RStudio, Systat, SPSS, Excel
- Programming – R
- Phylogenetics – PAUP, Mesquite, BEAST, etc.
- Equipment – Leica cryostat, Leica microscopes, Nikon XTH 225 2x microCT scanner, Bruker SkyScan microCT scanner, Keyence fluorescence microscope
- Other – ArcGIS

Workshops & Certifications

- Nikon X-Ray CT Training (USU; Summer 2022)
- NSF-sponsored Slicermorph Workshop (University of Washington, Friday Harbor Lab; August 2019)

SUPERVISION

Graduate Advisory Committees

Doctoral (USU)

- Major Advisor: Alan H. Savitzky
- Departmental Committee Members:
  - Susannah French
  - Sara Freeman
  - Molly Womack
- External Committee Member:
  - Kerry Jordan

Master's (SELU)

- Major Advisor: Clifford L. Fontenot, Jr.
- Co-advisor: Brian I. Crother
- Committee Member: David M. Sever